The University Of Sheffield.

Simulation and Optimisation of Compressed Air Energy Storage Systems for Performance Improvement

A thesis submitted in partial fulfilment of the requirements for the degree of Doctor of Philosophy

2023

Name: Yuxing Ding

Supervisor Name: Prof. Meihong Wang

Department of Chemical & Biological Engineering

Faculty of Engineering

The University of Sheffield

Acknowledgement

Completing a PhD is a journey that is full of challenges and obstacles. It is not possible to achieve this milestone alone, and the successful completion of this PhD would not have been possible without the support and assistance of numerous individuals and organizations. I would like to take this opportunity to express my gratitude to all those who have helped me along the way.

First and foremost, I am deeply grateful to my supervisor, Prof. Meihong Wang. His guidance, support, and encouragement have been invaluable to me throughout this PhD journey. I appreciate his patience, kindness, and dedication to my success. His feedback and insights have been instrumental in shaping my research, and I have learned so much from his expertise and experience. I am fortunate to have had him as my mentor and advisor.

I am also thankful to the research participants (Dr Olumide Olumayegun, Dr Yurong Liu, Dr Yue Chai, Mr Yide Han, Dr Olajide Otitoju and Dr Toluleke Akinola) who generously gave their time and shared their experiences with me. Without their participation, this research would not have been possible. I appreciate their willingness to share their stories and insights, which have enriched my understanding of the topic and informed my research findings.

I am also indebted to my family and friends for their unwavering support and encouragement throughout this journey. Their love, understanding, and patience have sustained me during the challenging times and made the joyous moments even more meaningful. I am fortunate to have them in my life.

Finally, I would like to express my deepest gratitude to my wife, Dr Yurong Liu, who has been my rock and my source of inspiration. Her unwavering support, understanding, and encouragement have been instrumental in helping me to overcome the challenges and obstacles that I encountered during this journey. I am fortunate to have her by my side.

In conclusion, I am deeply grateful to all those who have helped me in any way during this PhD journey. Their support, encouragement, and contributions have made this milestone possible. I will always remember their kindness and generosity with gratitude and appreciation.

Abstract

Compressed Air Energy Storage (CAES), a technology capable of large-scale energy storage (>100MW), has already been implemented commercially in industry. However, the round-trip efficiency (RTE) of existing commercial CAES plants leaves room for significant enhancement. CAES systems hold an important role in balancing electricity supply and demand, especially as they can be integrated with renewable energy sources to overcome their inherent intermittency. This thesis aims to explore strategies to enhance the RTE of CAES, and to examine its design, operation and cost reduction. This investigation was achieved through process simulation and optimisation.

Firstly, a newly combined cooling heating and power (CCHP) system that integrates a CAES system, organic Rankine cycle (ORC) and single-effect absorption refrigeration system (ARS) using LiBr/H_2O is proposed in this study. The ORC can operate during both charging and discharging process. The waste heat was recovered from recuperator in CAES, thereby improving its RTE. Steady-state process models of the CCHP system were developed in Aspen Plus® V12 and validated individually. Process analysis was undertaken using the validated models to assess the effect of six organic working fluids of the ORC and several key parameters (inlet mass flowrate of pump in ARS, inlet temperature of combustion chamber 1, different working fluids for ORC, ORC turbine inlet pressure, inter-cooler temperatures, and compressor's inlet temperatures) on system performance. Results show that the RTE of CCHP (using R290) and overall exergy efficiency of the CCHP system are 67.6% and 51.21%, respectively. Among the factors examined, the inlet temperature of the compressor and the inlet temperature of the combustion chamber are the most decisive parameters influencing the system's performance.

Additionally, a multi-objective optimisation was conducted to maximise the RTE and minimise the total investment cost per output power (ICPP) of the CCHP (including CAES, ORC and single-effect ARS using LiBr/H_2O). The findings reveal that the optimised CCHP system has advantages with a significantly enhanced efficiency reaching 68.38% RTE (increased by 0.78%) and a cost-efficiency improved to 0.20 $/kWh ICPP (decreased by 2.68%).

In another configuration of CCHP (including CAES, ORC and different types of ARS), the ORC was designed to operate exclusively during the charging process, while the ARS functioned solely during the discharging phase. Under these design conditions, the low-grade waste heat from the flue gas was completely supplied to ARS. The CCHP system integrated with different types of ARS (i.e. different effect and different working medium) was compared. The results indicate that the double-effect ARS performs better than the single-effect ARS with the same working medium. The lithium bromide/water ($LiBr/H_2O$) is more suitable than ammonia/water (NH_3/H_2O) as working medium. The double-effect ARS $LiBr/H_2O$ has the better performance, which can produce 206 MW of electrical energy, 7.26 MW of heating, and 27.28 MW cooling capacity (COP 1.36). The levelized cost of electricity (LCOE) of the CCHP-3 system is 31.01 $/MWh, and the payback period is 12.9 years.

Keywords: Compressed air energy storage (CAES), Organic Rankine cycle (ORC), Absorption refrigeration system (ARS), CCHP, Process simulation, Process Optimisation, Process integration, Economic evaluation.

Peer-reviewed Publications and Presentations

Part of this thesis has been published in the following peer-reviewed journals:

- **Ding, Y.,** Olumayegun, O., Chai, Y., Liu, Y. and Wang, M., (2022), Simulation, energy and exergy analysis of compressed air energy storage integrated with organic Rankine cycle and single-effect absorption refrigeration for trigeneration application. *Fuel*, 317, 123291.
- Liu, Y., **Ding, Y.,** Yang, M., Peng, B.Y. and Qian, F., (2022), A trigeneration application based on compressed air energy storage integrated with organic Rankine cycle and absorption refrigeration: Multi-objective optimisation and energy, exergy and economic analysis. *Journal of Energy Storage*, 55, 105803.
- Liu, Y., Yang, M., **Ding, Y.,** Wang, M., and Qian, F., (2022), Process modelling, optimisation and analysis of heat recovery energy system for petrochemical industry. *Journal of Cleaner Production*, 381, 135133.
- **Ding, Y.,** Liu, Y., Chai, Y., Han, Y., Olumayegun, O., Wang M. (2023), Energy analysis and economic evaluation of cogeneration system integrating compressed air energy storage system, organic Rankine cycle with different absorption refrigeration systems, *Journal of Energy Storage*. (Accept with minor modification)
- **Ding, Y.,** Liu, Y., Wang, M., Wenli Du., Qian F. (2023), Heat integration, simultaneous structure and parameter optimisation, and techno-economic evaluation of waste heat recovery systems for petrochemical industry, *Energy*. (Under Review)
- **Ding, Y.,** Liu, Y., Han, Y., Hui, Y., Wenli, Du., Feng, Qian., Wang M. (2023), A carbon neutral system based on liquid air energy storage, closed Brayton cycle and solar power: energy, exergy and economic (3E) analysis. Fuel, (Under review)

Conference Presentation:

Ding, Y., Chai Y., Wang, M. (2021). Thermodynamic analysis of compressed air energy storage system integrated with ORC and a single-effect LiBr/H_2O absorption system. The European Conference on Fuel and Energy Research and its Applications (1st FERIA), Nottingham, United Kingdom, 6-8 September 2021.

Ding, Y., Wang, M. (2023). A carbon neutral system based on liquid air energy storage, closed Brayton cycle and solar power: energy, exergy and economic (3E) analysis. The European Conference on Fuel and Energy Research and its Applications (2nd FERIA Conference), Sheffield, United Kingdom, 4-6 September 2023.

Table of Contents

List of Figures

List of Tables

Nomenclatures

C_{avg}	Average specific heat capacity of the substance (kJ/kg·K)
$\dot{C}_{total}$	Total cost rate ($/d)
$\dot{C}_{fuel}$	Fuel cost rate ($/d)
ex	Summation of the physical and chemical exergy (kW)
$\dot{E}_x^{D}$	Exergy destruction of the component (kW)
$\dot{E}_x^{Q}$	Exergy associated with heat (kW)
$\dot{E}_x^{W}$	Exergy associated with work (kW)
h_i	Enthalpy (kJ/kg)
h_0	Enthalpy at the reference state (kJ/kg)
i_r	Interest rate
LHV	Lower heating value of fuel (kJ/kg)
$\dot{m}$	Mass flowrate (kg/s)
N	System lifetime (year)
p_0	Ambient pressure (bar)
$\dot{Q}$	Heat flow (kW)
$Q_{cooling}$	Cooling capacity of ARS (kW)
$Q_{ARS,evap}$	Heat duty of evaporator in ARS (kW)
$Q_{ARS,desorber}$	Heat duty of desorber in ARS (kW)
s_i	Specific entropy
T_0	Ambient temperature (℃)
T_i	Temperature of the heat transfer (℃)

W_t	Output power of Turbine (kW)
W_{comp}	power consumption of compressors in charging process (kW)
W_{orc-c}	Output power of ORC in charging process (kW)
W_{orc-d}	Output power of ORC in discharging process (kW)
$W_{ORC,p-c}$	power consumption of ORC pump in charging process (kW)
$W_{ORC,p-d}$	power consumption of ORC pump in discharging process (kW)
$W_{LiBr,p}$	power consumption of pump in LiBr/H_2O absorption system (kW)
$W_{ARS,pump}$	power consumption of pump in ARS (kW)
$\dot{Z}_{total}$	Investment cost rate ($/d)
γ	Specific heat ratio of the air
γ_g	Specific heat ratio of the gas turbine

Greek Symbols

η	Efficiency
ρ	Density (kg/m^3)
γ	Maintenance factor

Abbreviations

A-CAES	Adiabatic compressed air energy storage
ACAPAX	Annualized capital expenditure
AA-CAES	Advanced adiabatic compressed air energy storage
APEA	Aspen Process Economic Analyzer®
ARS	Absorption refrigeration system
BES	Battery energy storage
CAES	Compressed air energy storage
CCHP	Combined cooling heating and power
CEPRI	China Electric Power Research Institute
CES	Cryogenic energy storage
COP	Coefficient of performance
CRF	Capital recovery factor
D-CAES	Diabatic compressed air energy storage
EES	Electrical energy storage
FES	Flywheel energy storage
FBES	Flow battery energy storage
FOPEX	Fixed operational expenditure
GSHP	Ground source heat pump
I-CAES	Isothermal compressed air energy storage
ICPP	Investment cost per output power
IEA	International Energy Agency

IET-CAS	Institute of Engineering Thermophysics, Chinese Academy of Sciences
IPC, CAS	Institute of Physics and Chemistry, Chinese Academy of Sciences
KCS	Kalina cycles
LAES	Liquid air energy storage
LCOE	Levelized Cost of Electricity
O&M	Operating and maintenance
ORC	Organic Rankine cycle
PCM	Phase change material
PH-CAES	Pumped Hydro-Compressed Air Energy Storage System
PGU	Power generation unit
PHES	Pumped hydroelectric energy storage
PV	Photovoltaic
RTE	Round-trip efficiency
SGCC	State Grid Corporation of China
SC-CAES	Supercritical compressed air energy storage
SOFC	Solid oxide fuel cell
TAC	Total annual cost
T-CAES	Trigenerative compressed air energy storage system
TES	Thermal energy storage
VOPEX	Variable operational expenditure
VRB	Vanadium redox

1. Introduction

1.1 Background

1.1.1 Rising electricity demand and renewable energy

The global electricity demand continues to surge, with the average global electricity consumption reaching 26,832 TWh in 2020, and the trend of increasing power consumption shows no sign of slowing down (IEA, 2022). Figure 1-1 depicts traditional power plants that rely on fossil fuels, such as coal, oil, and natural gas, still contribute significantly to the world's electrical energy production in 2020 (IEA, 2022). However, there has been a noticeable shift towards renewable energy sources such as hydro, solar, and wind in recent years, a positive trend towards sustainable and clean energy production.

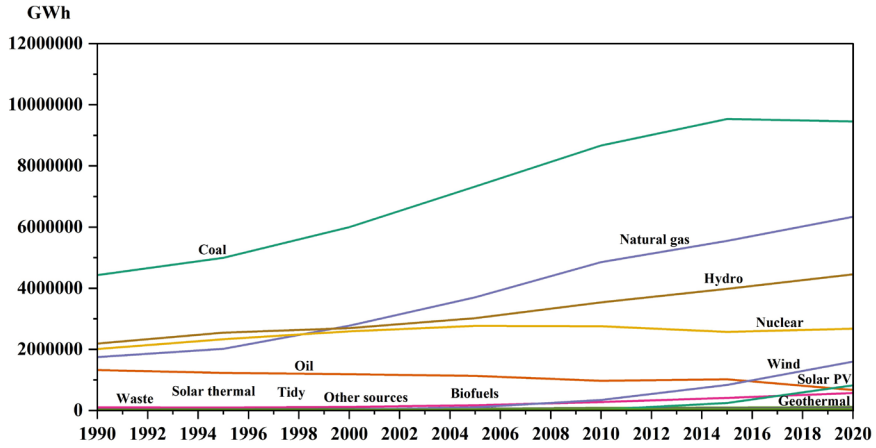

Figure 1-1 The sum of global electricity generated by various energy sources from 1990 to 2020 (IEA, 2022)

As traditional fossil fuel energy sources (including coal, oil and natural gas) release significant amounts of greenhouse gases during combustion, they contribute to the alarming issue of climate change and global warming. Furthermore, the extraction and utilization of finite fossil fuel resources not only adversely impact the environment but also have detrimental effects on human health (Meng et al., 2018). As a result, renewable energies (such as solar, wind and tide power) have been developed as alternative energy sources, which could reduce carbon footprint and advance environmental sustainability. The intermittency of renewable energy sources poses a significant challenge to the

availability and reliability of clean energy. To overcome this limitation, energy storage technologies have emerged as a critical solution for addressing the intermittency of renewable energy sources.

1.2 Brief introduction to energy storage technologies

1.2.1 Classification of energy storage technologies

Energy storage technology refers to the process of transforming electrical energy into various forms of potential energy (such as chemical, electromagnetic, thermal, or mechanical) for subsequent utilization. The existence of different forms of energy with varying energy levels and utilization requirements, has created many energy storage technologies. The technology was developed to accommodate these diverse needs. Many energy storage technologies are currently in use, each of which can be broadly classified according to the intended purpose of the stored energy. Figure 1-2 depicts the classification of diverse energy storage technologies. Two primary categories of energy storage technologies are electrical energy storage (EES) and thermal energy storage (TES).

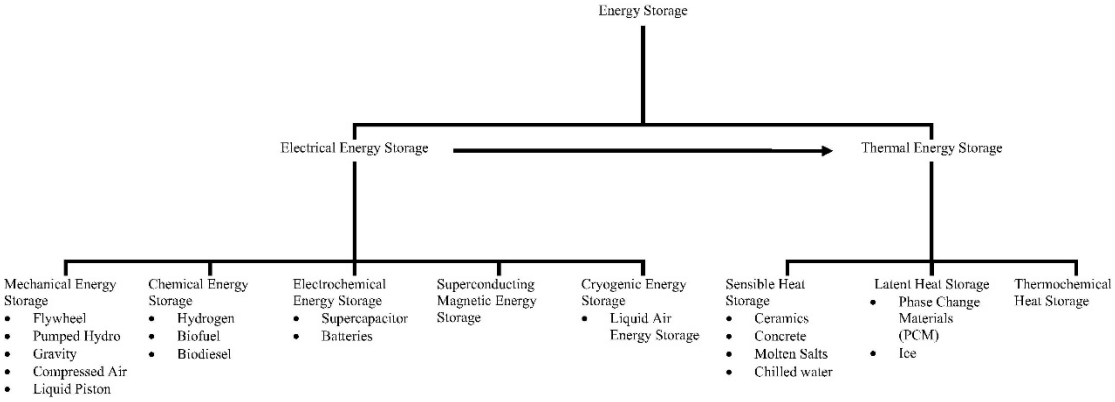

Figure 1-2 Classification of energy storage strategies (Aneke and Wang, 2016)

1.2.2 Pumped hydro electric energy storage (PHES)

Pumped hydro energy storage (PHES) is the most widely adopted technology for large-scale (>100 MW) commercial applications, and it has been extensively validated (Kaldellis, 2008; Deane et al., 2010). Figure 1-3 illustrates the schematic diagram of a pumped hydro storage plant. The PHES system embodies three principal elements: the reversible pump/turbine, the dedicated pumps, and the generators (Nikolaidis and Poullikkas, 2017). In the charging

phase, electrical energy harvested from an off-peak power source drives a pump to elevate water from a lower to an upper reservoir, effectively transferring electrical energy into potential energy brought by the heightened water mass. During the discharging phase, this reserved potential energy is used as the elevated water cascades down to stimulate the turbines, generating electricity. This interplay of potential and kinetic energy illustrates the energy transformation within the PHES system.

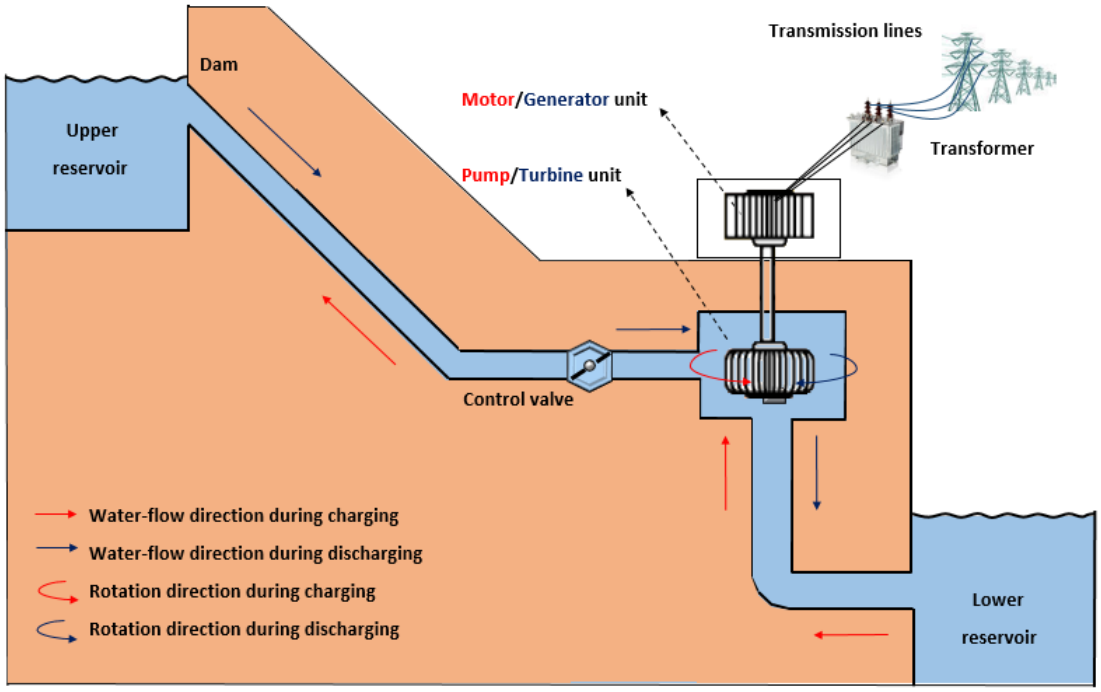

Figure 1-3 Schematic diagram of PHES plant (Nikolaidis and Poullikkas, 2017)

At the moment, there are more than 300 PHES facilities with a combined installed capacity of more than 120 GW. A significant percentage of the worldwide large-scale energy storage building (about 99%), is composed of PHES and another small part (Pittock, 2010; Luo et al., 2015; Aneke and Wang, 2016). However, the system has a high requirement on geographical conditions, requires more water supply, and has a long construction period, which has a great impact on the environment (Rogeau and Kariniotakis, 2017; Ferreira et al., 2013).

1.2.3 Compressed air energy storage (CAES)

The CAES system is a promising option for large-scale (>100 MW) energy storage applications comparable to PHES. Currently, only two commercial CAES facilities are in operation worldwide: the Huntorf CAES plant in Germany (since 1978) and the McIntosh CAES plant in the United States (since 1991) (Budt et al., 2016). Figure 1-4 illustrates the operational process of a CAES system, which utilizes gas turbine technology.

During the charging phase, surplus or low-cost energy is used to compress air and store it at high pressure in underground caverns, thereby converting electrical energy into potential energy (Meng et al., 2018).

In the discharging phase, high-pressure compressed air is released from the cavern, heated and expanded in a gas turbine to generate electricity during peak demand, converting the potential energy back into electricity.

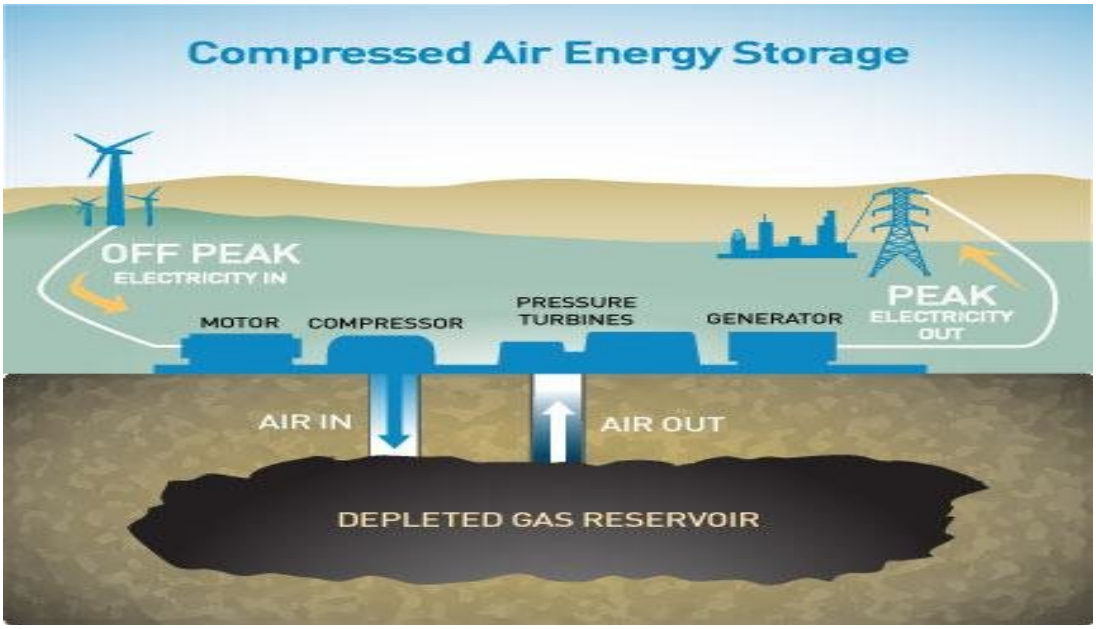

Figure 1-4 Schematic diagram of CAES plant (Meng et al., 2018)

The CAES system offers several advantages, including the potential for smaller unit sizes, the ability to integrate renewable energy sources to mitigate intermittency issues, and a long lifespan of approximately 50 years (Aneke and Wang, 2016). However, the technology has significant challenges, including high capital costs and geological constraints.

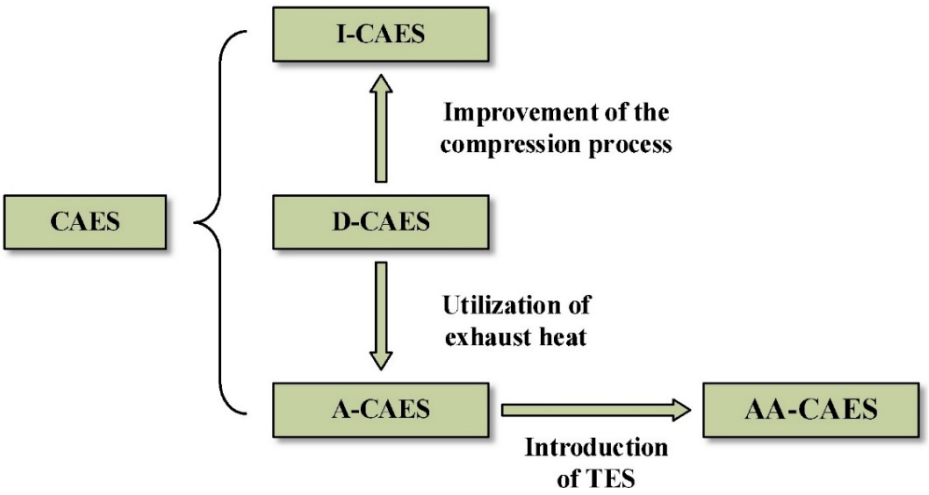

Figure 1-5 The classification of CAES (Zhou et al., 2019)

Figure 1-5 presents a specific classification of CAES systems based on their development process. CAES technology can be categorized into three types: Isothermal-CAES (I-CAES), Diabatic-CAES (D-CAES), and Adiabatic-CAES (A-CAES). The A-CAES can be subdivided into A-CAES without TES and A-CAES with TES. Currently, only D-CAES has been commercialized.

Table 1-1 The comparison of different CAES (Budt et al., 2016; Zhou et al., 2019)

	Diabatic		Adiabatic		Isothermal	
Round-trip efficiency	Today	Target	Today	Target	Today	Target
	54%	60%	-	70%	38%	80%
Energy density (kWh/m^3)	2-15		0.5-20		1-25	
Start-up time (min)	10-15		5-15		<1	
Power range	5 MW-1 GW		1 MW-1 GW		5 kW-1 GW	
Development Status	Application/ Demonstration		Research/ Demonstration		Research/ Demonstration	

The D-CAES systems require an external heat source, typically a combustor, for the discharge process. In contrast, A-CAES systems do not require an

external heat source due to the incorporation of additional TES devices that capture heat of compression. However, A-CAES systems without TES have been reported to have significant drawbacks, such as low round-trip efficiency (RTE), since the air is not cooled at each compression stage, limiting the ability to raise air pressures. Therefore, research efforts have focused on A-CAES with TES, which can be classified into high-, medium- and low-temperature storage systems. I-CAES systems aim to avoid temperature changes during charging and discharging but are limited to laboratory-scale investigation due to low energy density. Table 1-1 provides a comparative analysis of the technical requirements for the three CAES systems.

1.2.4 Liquid air energy storage (LAES)

In recent years, the energy storage industry has witnessed a growing interest in the novel technology known as LAES, which is also referred to as cryogenic energy storage (CES) or "cold thermal energy storage". As an emerging technology, LAES shares similarities with the compression stage of CAES in the early stages of the process. However, in the LAES system, the heat that would otherwise be lost is captured and contained in a phase change material (PCM) (Sciacovelli et al., 2017).

Figure 1-6 shows stand-alone LAES plant. At the start of the charging process, surplus or inexpensive energy is used to compress the air, and the compressed air is liquefied and held in a tank at a pressure equal to or just below the air pressure at sea level. During the discharging process, liquid air can be pumped (and hence used for auxiliary cooling purposes) while also being vaporised using waste heat and ultimately expanded for electricity generation (Aneke and Wang, 2016).

Higher energy densities, long storage time, and up to 80% RTE are advantages of LAES (Chen et al., 2009). In comparison to CAES systems, LAES systems are not hindered by geological conditions. With respect to the 1/700th ratio, the liquid air uses up the same volume of space as gaseous air, but the same amount of energy can be contained in smaller storage tank (Aneke and Wang, 2016).

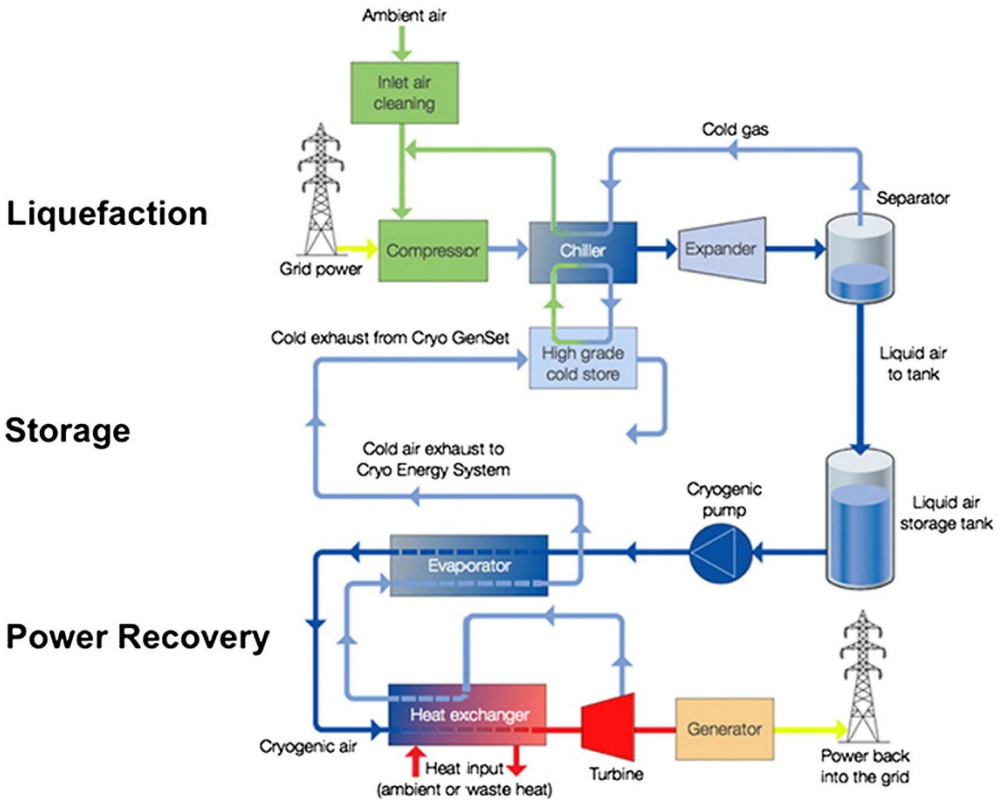

Figure 1-6 The schematic diagram of Highview LAES plant (Aneke and Wang, 2016)

1.2.5 Flywheel energy storage (FES)

A flywheel is a large rotating disc with a mass comparable to that of a washing machine, designed to store energy in the form of rotational kinetic energy, which can subsequently be converted into electrical energy (Tan et al., 2013). The flywheel energy storage system is composed of several key components, including a high-speed flywheel, a bearing system, a motor, a generator and a vacuum pump, as depicted in Figure 1-7.

The FES device uses extra power during the charging process to drive the flywheel at high speed and transforms the power into rotational kinetic energy to complete the energy storage process. During the discharging process, the high-speed rotating flywheel drives the electrochemical power generation, and the energy output is completed through the energy conversion device, realising the conversion of mechanical energy to electric energy.

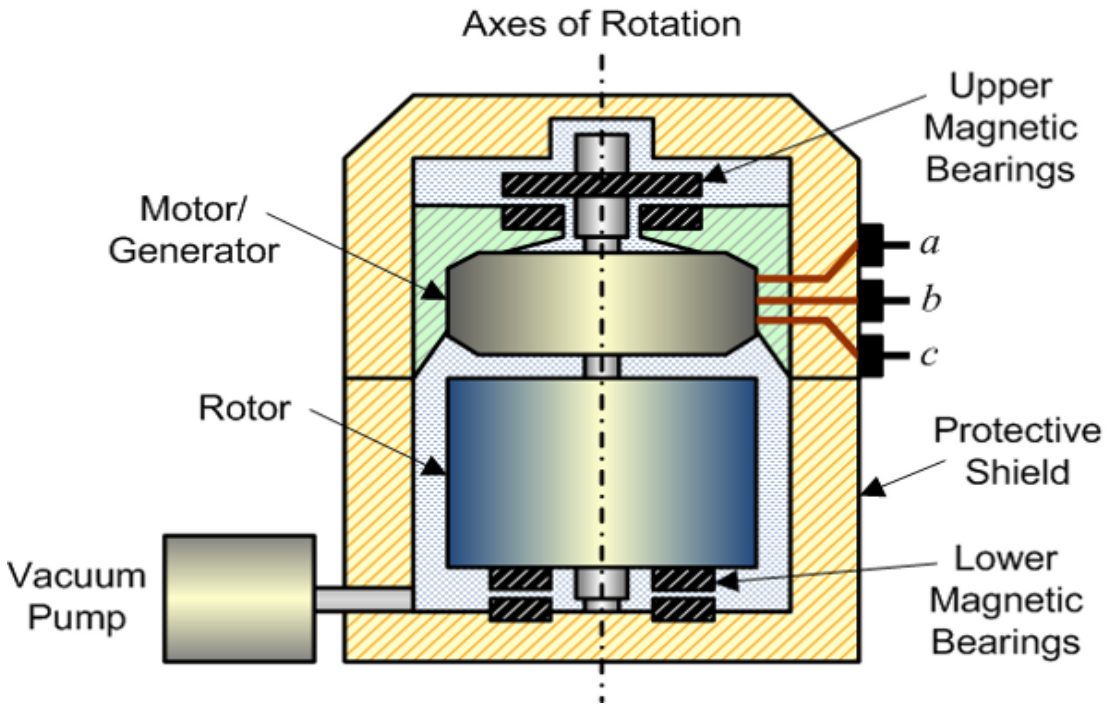

Figure 1-7 The schematic diagram of a conventional flywheel (Molina, 2010)

FES can be divided into two forms depending on the spinning speed: low-speed (typically less than 6,000 rpm) and high-speed (typically greater than 100,000 rpm). FES systems exhibit remarkable characteristics: high efficiency (80-90%), power density exceeding 5 kW/kg, energy density over 20 Wh/kg, low maintenance costs, absence of pollution and versatile applications including emergency power supply, power grid peak regulation and frequency control (Aneke and Wang, 2016). However, FES requires higher structure, materials and tightness of the device, and is restricted by its working principle. To put it another way, large-scale energy storage is virtually impossible to accomplish (Kousksou et al., 2014).

1.2.6 Battery energy storage (BES)

BES systems use the redox (reduction-oxidation) reactions between the positive and negative electrodes to facilitate the conversion of chemical energy into electrical energy and vice versa.

During the discharging phase, these chemical reactions occur at the respective electrodes while the current flows through the external circuit from the anode to the cathode. During the charging cycle, the battery can be recharged by

applying an external voltage across the electrodes, allowing the reactions to occur in the opposite direction (Ferreira et al., 2013).

Presently, various battery storage technologies find application in power systems, including lead-acid (PbO_2) batteries, nickel-cadmium (NiCd) batteries, lithium-ion (Li-ion) batteries, sodium nickel chloride ($NaNiCl_2$) batteries, sodium sulphur (NaS) batteries and liquid flow batteries. The following sections will introduce some typical battery types and their characteristics.

(1) PbO_2 battery

PbO_2 batteries, developed by French physicist Gaston Plante in 1859, represent the oldest rechargeable battery technology (Moubayed et al., 2008). These batteries comprise a negative electrode of lead sulphate, a positive electrode of lead acetate and an electrolyte solution of sulfuric acid and water. Figure 1-8 illustrates a PbO_2 battery.

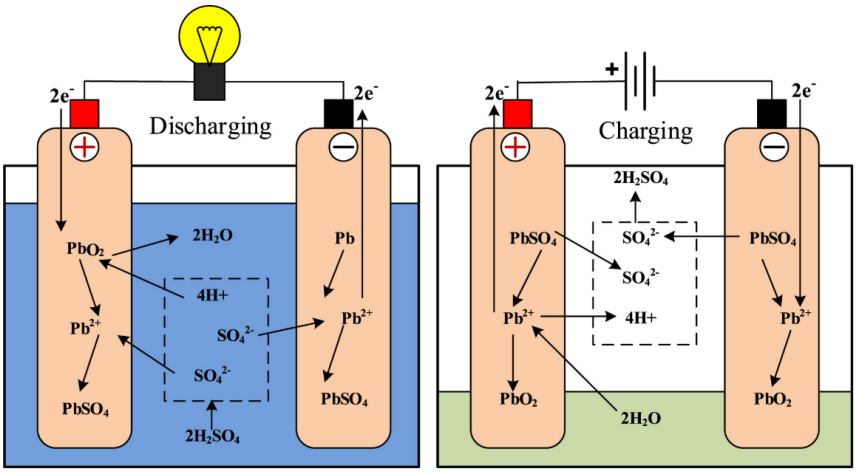

Figure 1-8 The schematic diagram of PbO_2 battery (Hannan et al., 2017)

Due to their affordability, well-established technology, and high reliability, PbO_2 batteries have been a popular choice in various applications. In the energy storage industry, they were among the earliest battery technologies utilized and extensively employed in power systems such as peak regulation, enhancing system stability and improving power supply quality. However, PbO_2 batteries do possess certain limitations. These include slow charging speed, relatively low energy density, limited cycle life and the potential for environmental pollution (Hannan et al., 2017).

(2) NiCd battery

NiCd batteries, known for their maturity in battery technology, utilize nickel hydroxide as the positive electrode and cadmium as the negative electrode. These batteries offer high energy density, excellent power output and long cycle life advantages, making them well-suited for electric vehicle applications. However, it should be noted that the capacity of NiCd batteries tends to decrease over repeated charging and discharging cycles, and there is a risk of heavy metal pollution associated with the cadmium content (Aneke and Wang, 2016; Ferreira et al., 2013; Gidwani et al., 2014).

(3) Li-ion battery

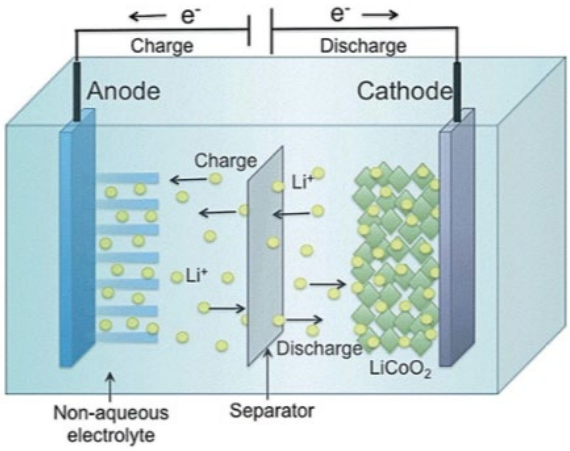

Figure 1-9 The schematic diagram of Li-ion battery (Roy and Srivastava, 2015)

Li-ion batteries, depicted in Figure 1-9, are operated by the movement of lithium ions between the two electrodes. As the electrochemical reaction proceeds, Li+ ions are gradually intercalated and deintercalated between the positive and negative electrodes. Li+ ions are deintercalated from the positive electrode and intercalated into the negative electrode through the electrolyte during the charging process. Li-ion batteries offer several advantages due to their higher voltage, facilitating the establishment of battery power supply networks. Additionally, the negative electrode remains in a lithium-rich state. Li-ion batteries exhibit a high energy density (90-190 Wh/kg), making them lighter than PbO_2 batteries (Aneke and Wang, 2016). These batteries have a relatively

long lifespan, high power tolerance, excellent adaptability to high and low temperatures and environmentally friendly characteristics (Li and Zhou, 2012). However, it is important to note that Li-ion batteries also have some disadvantages, including safety concerns, the risk of explosion and high costs associated with large-scale industrial applications (Aneke and Wang, 2016).

(4) NaS battery

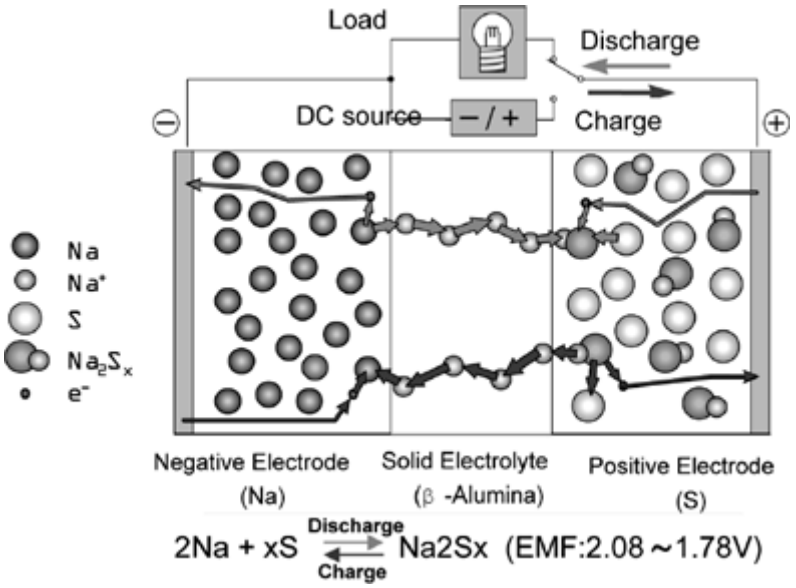

Figure 1-10 NaS battery (Oshima et al., 2004)

The utilization of NaS batteries (depicted in Figure 1-10) proves advantageous for large-scale energy storage systems, offering an energy storage capacity that is five times greater than PbO_2 batteries. During discharging, sodium (Na) donates an electron to the external circuit. As a result, Na ions migrate through the electrolyte towards the positive electrode, where they combine to form sodium polysulfide (Na_2Sx). Conversely, during the charging process, the reaction proceeds in the opposite direction (Oshima et al., 2004). The decomposition of Na_2Sx occurs during charging, and Na+ ions migrate back into the electrolyte. NaS batteries exhibit several noteworthy characteristics, including pollution-free operation, an exceptionally high energy density (760 Wh/kg), high energy efficiency (95% or higher) and long cycle life (2500 cycles or more). However, it is important to note that safety concerns arise when the battery temperature exceeds 300˚C (Aneke and Wang, 2016; Meng et al., 2019).

(5) $NaNiCl_2$ battery

$NaNiCl_2$ batteries represent a novel high energy thermal battery developed based on the NaS battery technology. Operating at temperatures ranging from 275 to 300˚C (Aneke and Wang, 2016), the $NaNiCl_2$ battery offers unique advantages in terms of its operational characteristics. During the charging process, the positive electrode of nickel releases electrons, forming Ni2+ ions. These ions then interact with chloride ions in the electrolyte to form $NiCl_2$. Conversely, Ni2+ ions at the positive electrode gain electrons during the discharging process and transform back into elemental nickel. Simultaneously, at the negative electrode, electrons are lost, leading to the production of Na ions. These Na ions pass through the ceramic isolation membrane and combine with chloride ions in the positive electrode-electrolyte interface to form sodium chloride. Despite its merits, the $NaNiCl_2$ battery exhibits a drawback in its relatively lower moderate energy density (Luo et al., 2015).

Table 1-2 Summarises of the technical characteristics of different BES (Aneke and Wang, 2016; Meng et al.,2018)

System	Energy density (Wh/kg)	Power density (W/kg)	Power rating (MW)	Discharging time	Suitable storage duration	Response time	Capital Cost ($/kWh)	Round-trip efficiency (%)
PbO_2	50-80	90-700	0-20	Seconds-hours	Minutes-days	< Second	63-90	300-600
NiCd	15-80	75-700	0-40	Seconds-hours	Minutes-days	< Second	60-80	500-1500
NaS	15-300	120-160	0.05-8	Seconds-hours	Seconds-hours	< Second	70-90	1000-3000
$NaNiCl_2$	150-180	220-300	0-0.3	Seconds-hours	Seconds-hours	< Second	85-90	150-300
Li-ion	200-400	1300-10000	1-0.1	Seconds-hours	Minutes-days	< Second	90-97	1200-4000
VRB	20-70	0.5-2	0.03-3	Seconds-10 hours	Hours-months	Seconds	65-85	600-1500

A comprehensive overview of the technical characteristics of various BES systems is provided in Table 1-2, displaying a summary of their respective attributes.

1.2.7 Flow battery energy storage (FBES)

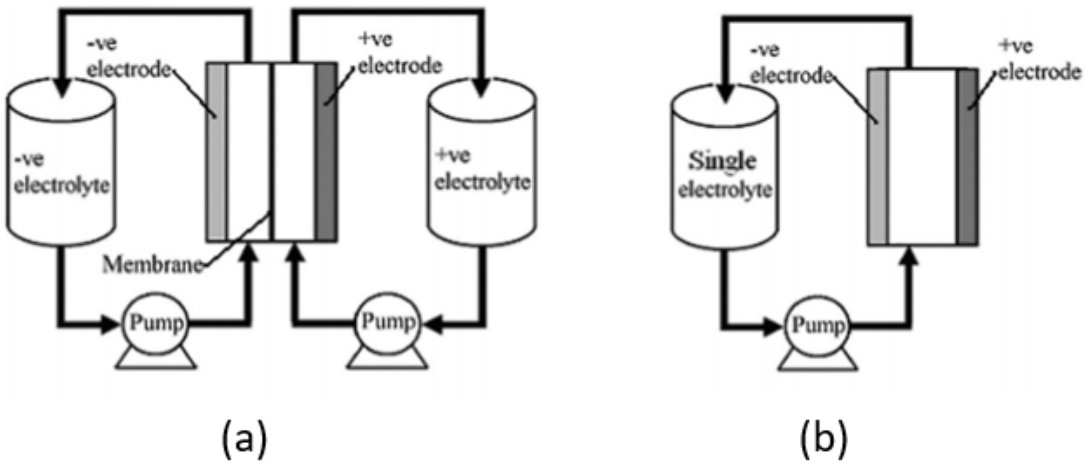

Figure 1-11 (a) Conventional redox flow battery (b) A soluble flow battery (Leung et al., 2012)

Flow batteries offer a promising solution for large-scale and efficient electrochemical energy storage, as they can convert and store various forms of energy into electrical and chemical energy. By circulating the electrolyte, the flow battery provides the necessary active substances for the electrochemical reactions, dissolving the previously stored active substances on solid electrodes (Aneke and Wang, 2016). Among the various types of flow batteries, the vanadium redox flow battery (VRB) stands out as the most representative dual-flow battery system. Depending on the configuration of solid electrodes, flow batteries can be categorized into conventional redox flow batteries (as depicted in Figure 1-11 a), soluble flow batteries (as illustrated in Figure 1-11 b) and metal & air flow batteries. The energy efficiency of flow batteries typically ranges from 75% to 85%, and they can withstand a significant number of charge and discharge cycles, reaching up to 13,000 cycles (Aneke and Wang, 2016). Nevertheless, the development of flow batteries is hindered by their low energy density and high cost, which remain key limiting factors (Luo et al., 2015).

1.2.8 Capacitor and supercapacitor energy storage

Supercapacitors have gained significant traction in backup power and renewable energy storage. The working principle of a supercapacitor is illustrated in Figure 1-12. Supercapacitors outperform secondary batteries in terms of power density, cycle life, adaptability (even at temperatures as low as -40°C), safety and reliability (Khaligh and Li, 2010). Supercapacitors employ

two primary storage mechanisms. Double-layer capacitors store energy through charge accumulation at the heterogeneous interface between the electrode and the electrolyte solution.

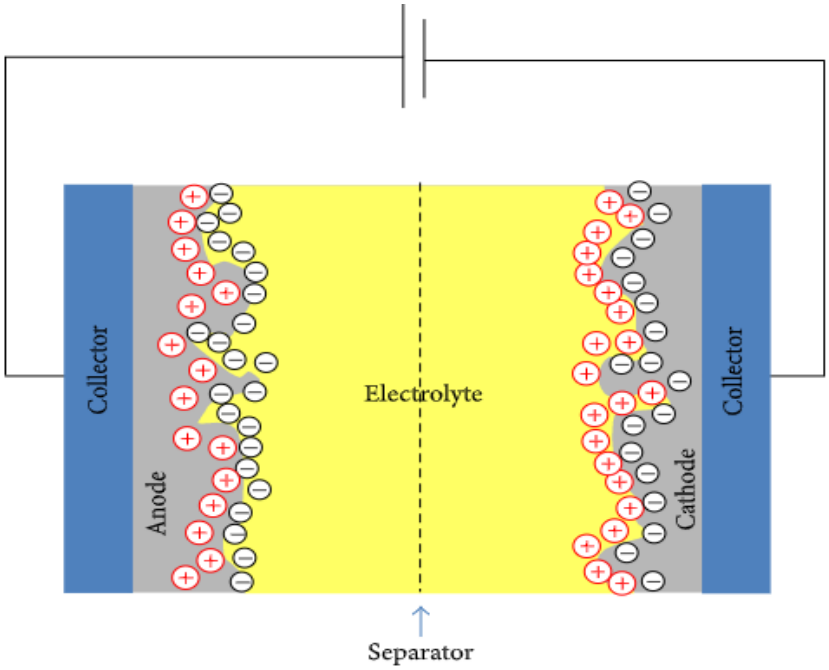

Figure 1-12 The schematic diagram of supercapacitor

On the other hand, Faraday pseudo capacitors rely on reversible redox reactions occurring between the electrode and the electrolyte in the electrode surface/quasi-two-dimensional space. However, one major drawback of supercapacitors is their high cost. Additionally, they are limited to direct current circuits and are susceptible to issues such as electrolyte leakage (Beaudin et al., 2014).

1.2.9 Thermal energy storage (TES)

TES has emerged as one of the most prominent methods for energy storage (Rismanchi et al., 2012). It addresses the temporal, spatial and operational disparities between the supply and demand of thermal energy in power plants and thermal consumers (Aneke and Wang, 2016; Zhou et al., 2019).

TES encompasses four major forms of heat storage based on the storage mode: cryogenic, sensible heat, latent heat and thermochemical (Aneke and Wang, 2016). Among these approaches, sensible heat storage has advanced theoretical and technological development. However, it suffers heat loss due to

its high freezing point (Aneke and Wang, 2016). Sensible heat storage includes packed bed and double-tank heat exchange fluid heat storage. Latent heat storage has garnered significant attention and is associated with the most comprehensive TES technologies due to its superior TES capacity and density (Zhou et al., 2019). Thermochemical heat storage is still in the early stages of research and development, with various materials under investigation.

The primary applications of heat storage technology include power plants, industrial waste heat recovery and spacecraft. However, heat storage equipment is currently in the experimental phase, and the RTE is approximately 30-55%. The development and application of thermal storage technology heavily rely on the selection and performance of thermal storage materials, which are key factors influencing their efficiency and feasibility.

1.2.10 Summary

Table 1-3 Comparison of different energy storage technologies (Meng et al., 2018; Aneke and Wang, 2016; Luo et al., 2015)

Technology	Energy density W/kg	Power density Wh/kg	Power Rating, MW	Discharging time	Suitable storage duration	Lifetime (years)	Round-trip efficiency (%)	Capital cost ($/kW)
PHES	0.5–1.5	0.1-0.2	100-5,000	1-24 hrs+	Hours-months	40-60	70-85	600-2,000
CAES	30–60	0.2-0.6	5-300	1-24 hrs+	Hours-months	20-60	40-75	400-800
LAES	97	-	0.35-5	1-24 hrs+	Hours-months	20-40	50-80	-
FES	20-80	40-2000	0-0.25	Up to 15mins	Seconds-minutes	20	85-95	250-350
PbO_2	50-80	90-700	0-20	Seconds-hours	Minutes-days	5-10	63-90	300-600
NiCd	15-80	75-700	0-40	Seconds-hours	Minutes-days	10-20	60-80	500-1,500
NaS	15-300	120-160	0.05-8	Seconds-hours	Seconds-hours	10-15	70-90	1,000-3,000
$NaNiCl_2$	150-180	220-300	0-0.3	Seconds-hours	Seconds-hours	10-14	85-90	150-300
Li-ion	200-400	1300-10000	0-0.1	Minutes-hours	Minutes-days	5-15	90-97	1,200-4,000
VRB	20-70	0.5-2	0.03-3	Seconds-10 hrs	Hours-months	5-15	65-85	600-1,500
ZnBr	30-60	1-25	0.05-2	Seconds-10 hrs	Hours-months	5-10	65-75	700-2,500
HES	500-3000	0.2-20	0-50	Seconds-24 hrs+	Hours-months	5-15	20-50	10,000
Capacitor	2-10	100,000	0-0.05	Up to 60 mins	Seconds-hours	5	60-70	200-400
Supercapacitor	10-20	40,000-120,000	0-0.3	Up to 60 mins	Seconds-hours	10-12	85-98	100-300
TES	80-500	-	0.1-300	1-24 hrs+	Minutes-months	10-20	30-60	100-400

Please refer to Table 1-3 for a comprehensive summary of the energy storage technologies discussed in this chapter. The table shows that CAES emerges as a promising long-term energy storage technology. However, it has its drawbacks. One of the primary limitations of CAES is its relatively low RTE, which necessitates the availability of suitable underground caverns for optimal operation. On the other hand, the diverse characteristics of alternative energy storage technologies provide the flexibility to choose the most appropriate solution based on specific requirements and conditions.

1.3 Brief introduction to air compressor and turbine in CAES

CAES is a technology that stores energy in the form of compressed air for later use. Figure 1-13 shows operational process of CAES system. The working principle of CAES involves two main stages: charging and discharging.

During the charging stage, excess electricity from the grid or renewable energy sources (such as wind or solar power) is used to run a compressor. The compressor takes in atmospheric air and compresses it to a higher pressure. The compressed air is then stored in an underground cavern or a specially designed above-ground storage vessel, where it can be held until needed.

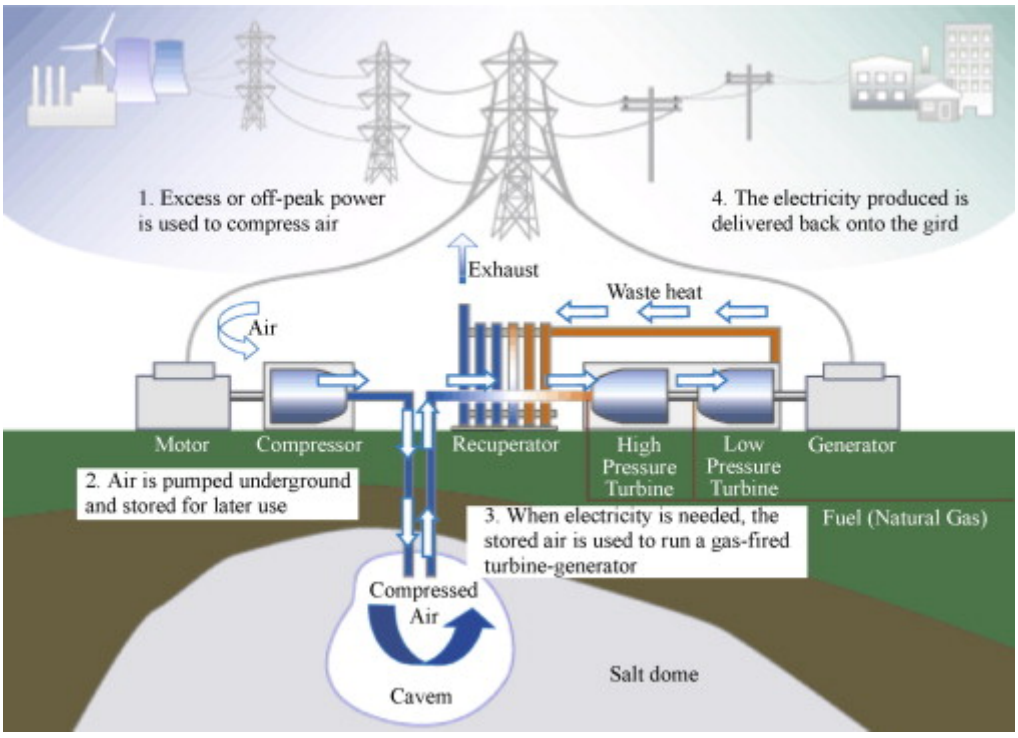

Figure 1-13 The schematic diagram of CAES plant (Chen et al., 2009)

The discharging stage begins when the energy demand on the grid increases or during periods when renewable energy sources are not generating enough power. To release the stored energy, the compressed air is released from the storage vessel and directed to a combustion chamber. In some CAES systems, natural gas or other fuels can be burned in combustion chamber to increase the energy output. After combustion, creating high temperature and high-pressure air that drives a turbine. The turbine is connected to a generator, which converts the mechanical energy into electrical energy. The generated electricity is then fed back into the grid to meet the increasing demand.

1.3.1 Axial Compressor

As illustrated in Figure 1-14, axial compressors are intricate machinery composed of multiple stages, each comprising a row of rotor blades followed by several stator blades. The functioning of axial compressors involves a sequential process where the air undergoes acceleration and deceleration. Initially, the rotor blades impart high-speed rotational motion to the air, resulting in its acceleration. Subsequently, as the air passes through the stator blade passages, it shows that during which its kinetic energy is efficiently converted into static pressure (Saravanamuttoo et al., 2001). The axial compressor possesses notable advantages, including accommodating higher flowrates and achieving superior pressure ratios compared to other compressor designs. These characteristics make axial compressors well-suited for various applications where efficient and substantial compression of air or gases is essential.

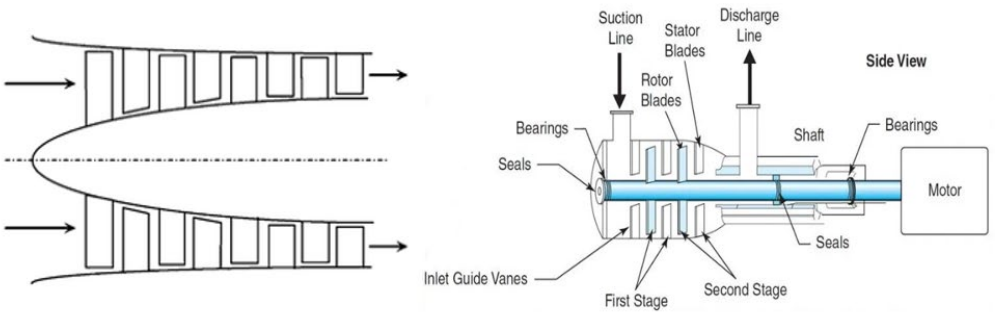

Figure 1-14 The schematic diagram of axial compressor (Saravanamuttoo et al., 2001)

1.3.2 Centrifugal compressor

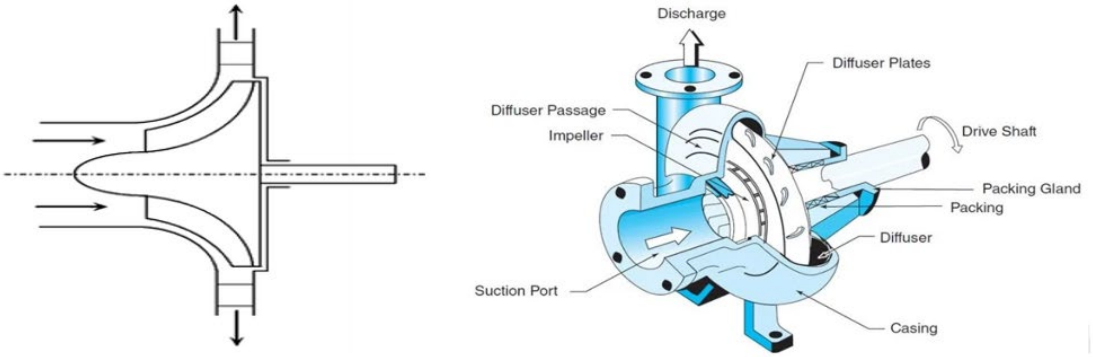

Figure 1-15 The schematic diagram of centrifugal compressor (Boyce, 2011)

As depicted in Figure 1-15, centrifugal compressors consist of a fixed casing housing a rotating impeller. The operational principle of this device involves the fluid entering the compressor through the inlet valve and then being redirected by 90 degrees to the radial direction, where it encounters the impeller. As the rotor or impeller imparts angular momentum to the fluid, its flow transitions into the axial direction, ultimately entering the volute (Lüdtke, 2004).

Table 1-4 Comparison of axial compressors and centrifugal compressors (Pelagotti et al., 2016)

Axial Compressor	**Centrifugal Compressor**
16-28 MW	16-44 MW
Up to 300,000 m^3/h inlet volume flow	Up to 500,000 m^3/h (double flow)
High efficiency 90%	Good efficiency 86%
Flexibility for operation and start up	High reliability
Fixed speed	Variable speed
pressure ratio per stage 1.15-1.35	pressure ratio per stage 7:1

Table 1-4 shows the comparison of axial compressors and centrifugal compressors. The centrifugal compressor offers several advantageous features, including remarkably low power consumption during start-up, the capability to achieve high-pressure ratios per stage, a wide range of rotational speeds and cost-effectiveness that makes it a competitive choice for various applications. These characteristics make centrifugal compressors well-suited for tasks requiring efficient compression of fluids, such as in industrial processes, refrigeration systems and gas turbines. Choosing the appropriate

compressor for specific design conditions is a critical aspect of engineering systems. Centrifugal compressors are often preferred for high flowrate and moderate pressure ratio applications. Axial compressors featuring two intermeshing rotors are well-suited for continuous duty and steady airflow applications, delivering reliable and consistent performance.

1.3.3 Axial turbine

Axial flow turbines, widely employed in large-scale commercial gas turbines, aircraft engines, power plants and other industrial applications, offer significant advantages in terms of efficiency and performance (Saravanamuttoo et al., 2001). Figure 1-16 shows the configuration of axial flow turbine. Their design enables a smooth and continuous flow of gases, allowing for higher power outputs and improved overall turbine performance. In contrast, radial inflow wheels are often preferred for smaller-scale micro-turbines due to their ability to tolerate running clearances and relatively minimal performance deficit compared to axial turbines. These radial inflow turbines provide reliable and efficient operation in compact configurations, making them suitable for various applications requiring compact power generation, such as distributed energy systems and small-scale industrial processes.

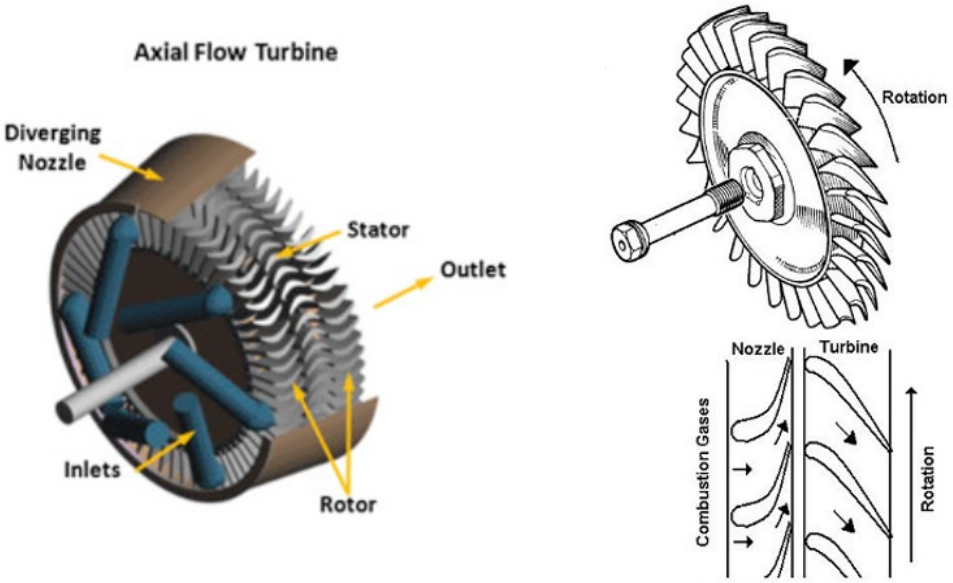

Figure 1-16 The configuration of axial flow turbine

1.3.4 Radial turbine

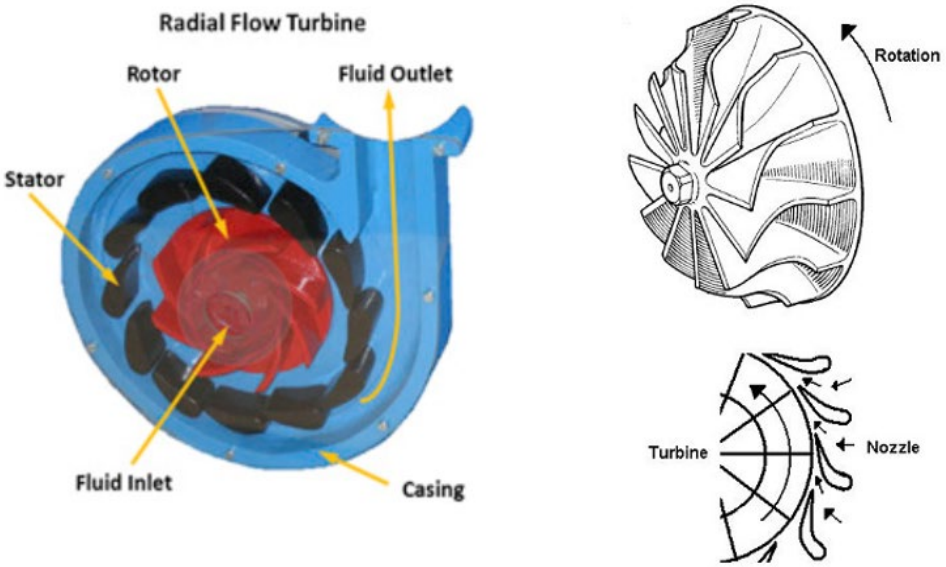

Figure 1-17 The configuration of radial flow turbine (Emrich, 2023)

The radial flow turbine shares similarities in design and construction with the centrifugal-flow compressor. It offers the advantage of ruggedness and simplicity, making it an attractive choice for certain applications. Figure 1-17 shows the configuration of radial flow turbine. Regarding manufacturing cost and ease, the radial inflow turbine proves to be relatively inexpensive and straightforward compared to its counterpart, the axial-flow turbine (Emrich, 2023). These factors contribute to its widespread utilization in various industries, where cost-effectiveness and manufacturing simplicity are crucial considerations (Boles and Cengel, 2014). The radial inflow turbine's robust design and straightforward construction make it a viable option for specific applications, offering an alternative solution to efficiently meet the desired operational requirements.

1.4 Brief introduction to organic Rankine cycle (ORC)

The RTE of CAES methods can be significantly reduced due to the unrecovered waste heat generated by the compressor. To address this issue, ORC has been introduced for large-scale waste heat recovery (Macchi and Astolfi, 2016). The working principle of the ORC process is depicted in Figure 1-18.

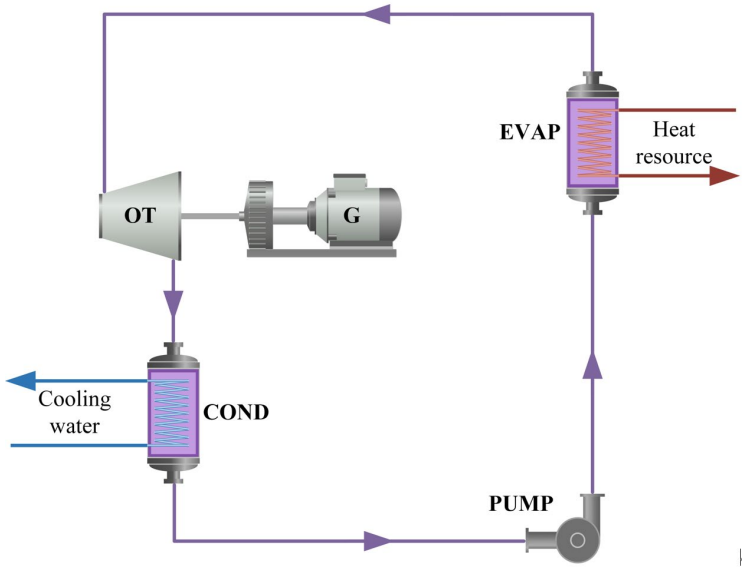

Figure 1-18 The diagram of ORC

This cycle consists of key components, including an evaporator, turbine, condenser and pump. The performance of the ORC is influenced by the choice of working fluid, as different types of fluids exhibit varying characteristics (Meng et al., 2018). In an integrated system combining CAES and ORC, the working fluid undergoes compression by a pump after exiting the condenser. Subsequently, the fluid is evaporated and passes through the turbine, ultimately reaching the condenser, where it undergoes re-condensation (Meng et al., 2018).

1.5 Brief introduction to combined cooling, heating and power (CCHP) system

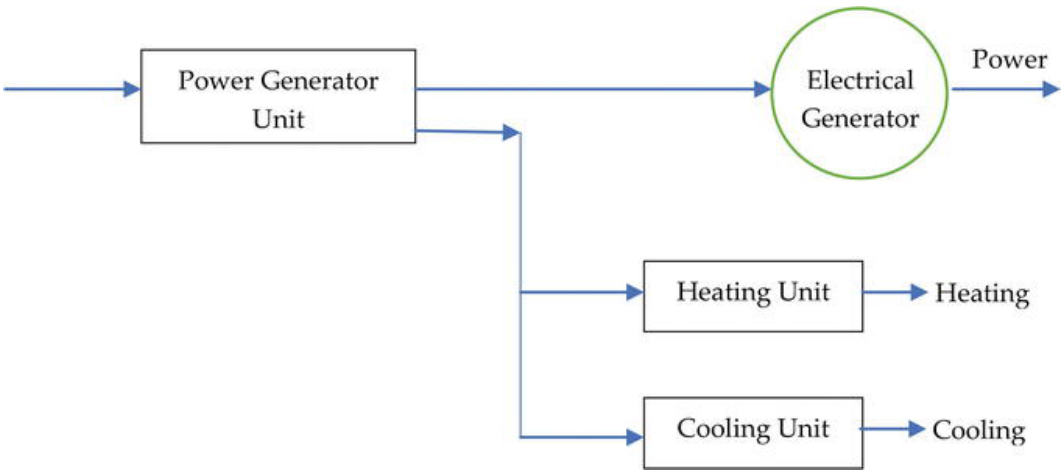

Figure 1-19 The diagram of CCHP system (Wu and Wang, 2006)

CCHP systems are designed to simultaneously generate electricity, heating and cooling, providing a comprehensive energy solution. A typical CCHP system comprises several key components, as Figure 1-19 illustrates, including a power generation unit (PGU), waste heat recovery system, gas boiler, absorption chiller and heat exchanger (Zhang et al., 2018). Implementing absorption chillers, which rely on mature technology, is prevalent in current CCHP systems (Wu and Wang, 2006). Among the numerous refrigerant and absorbent compounds available, the most commonly used working fluids for absorption chillers are lithium bromide/water ($LiBr/H_2O$) and ammonia/water (NH_3/H_2O) (Wu and Wang, 2006). The basic operation of a single-effect absorption refrigeration system (ARS) involves four main stages: absorber, desorber, condenser and evaporator. Initially, the concentrated solution refrigerant absorbs heat in the evaporator, causing evaporation and the formation of vapour, which is subsequently absorbed by the absorbent. The solvent absorbers are transferred from the solution to the desorber. As the refrigerant vapour becomes concentrated in the condenser, it is directed back to the evaporator after undergoing throttling (Wu and Wang, 2006).

1.6 Motivation

1.6.1 Large energy storage capacity

Among the various energy storage technologies, only PHES, CAES, and LAES have the capability for large-scale (>100MW) applications. PHES is the most mature technology, followed by CAES, which has reached commercialization but is still undergoing further development. However, PHES exhibits poor efficiency per unit mass and volume, necessitating massive storage tanks to achieve a certain power and energy capacity (Chen et al., 2009; Nikolaidis and Poullikkas, 2017). Geographical constraints and environmental concerns also limit the widespread commercial deployment of PHES. On the other hand, LAES systems have lower RTE (40% to 70%) and shorter storage durations than CAES, with associated concerns regarding leakages and safety precautions. Recognizing the importance of energy storage, the UK government has allocated £30 million for its development (UK government, 2017). Therefore, CAES technology holds significant potential for large-scale

applications and is poised for widespread adoption. In this study, the data from the real plant (>100 MW) is used to validate the CAES model.

1.6.2 RTE improvement

Efforts to increase RTE should encompass advancements in compressor design, waste heat recovery mechanisms and optimal system operation. Implementing these strategies will contribute to the overall enhancement of CAES system efficiency. Continued research and development in these areas will drive further improvements in the RTE of CAES systems.

Improving the efficiency of the compressor employed in the CAES system is crucial for enhancing RTE. Advancements in compressor design, including the utilization of more efficient compressor stages, optimisation of blade profiles, reduction of leakage losses and the application of advanced control algorithms, can optimize compressor operation and improve overall system efficiency. Efficient recovery and utilization of waste heat generated during the compression process can contribute to enhanced CAES system efficiency. Integration of heat exchangers and heat recovery systems enables the recovery and utilization of heat produced during compression. The recovered heat can be employed for purposes such as preheating the compressed air or providing additional thermal energy for power generation, thereby increasing overall efficiency. Operating the CAES system at optimal conditions plays a vital role in optimizing overall efficiency. Adjusting pressure ratios, temperature differentials and air mass flowrate in line with the specific requirements of the system can lead to improved performance. Employing advanced control strategies and real-time monitoring facilitates efficient system operation and enables dynamic adjustment of operating parameters to maximize efficiency.

1.6.3 Low-grade waste heat recovery and energy product diversity

The RTE of CAES can be further improved by integrated with ORC for the recovery of low-grade heat. During the discharging process, considerable amount of waste heat is present in the flue gas. This part of waste heat can be effectively utilized to drive an ARS, which enhances overall system efficiency and produce cooling capacity. CCHP systems offer several advantages that contribute to their widespread adoption and implementation. Firstly, these

systems enable simultaneous electricity, heating and cooling generation, presenting a holistic and integrated energy solution. By recovering and utilizing waste heat produced during electricity generation, CCHP systems minimize energy wastage and enhance overall system efficiency. Additionally, CCHP systems enhance the reliability and resilience of the energy supply. They can function autonomously, independent of the grid, providing backup power and thermal energy during grid outages, ensuring uninterrupted operation. Moreover, CCHP systems exhibit flexibility and scalability, allowing them to meet diverse energy demands. They can be customized to cater to specific requirements in various sectors, including residential, commercial and industrial applications. Overall, CCHP systems offer a comprehensive, efficient and adaptable approach to energy generation, providing multiple benefits for sustainable and reliable energy utilization.

1.7 Aim, objectives and novel contribution

The aim of this study is to improve the RTE as well as to gain understanding of the operational performance of CCHP through integrating CAES with ORC and ARS. This study will be achieved through steady-state simulation, model validation, exergy analysis, economic analysis and multi-objective optimisation. In order to achieve the aim, the objectives of the whole project will be split into three sections.

For the whole project:

- ✓ To carry out a comprehensive literature review on CAES (commercial applications, pilot plants and lab rigs), modelling, simulation and optimisation.

Stage one:

- ✓ To develop steady-state models of CAES, ORC and single-effect ARS in Aspen Plus®.
- ✓ Model validation of CAES, ORC and single-effect ARS.
- ✓ Energy and exergy performance evaluation of the CCHP system.
- ✓ Sensitivity analysis of system performance to study the effect of inlet mass flowrate of pump in ARS, inlet temperature of combustion chamber,

different working fluids for ORC, ORC turbine inlet pressure, inter-cooler temperatures and compressor inlet temperatures.

Stage two:

- ✓ Process simulation and multi-objective optimisation for the validated model.
- ✓ To compare different working fluids of ORC to evaluate the system performance.
- ✓ For the CCHP system, to performed energy, exergy and economic analysis.

Stage three:

- ✓ To compare different types of ARS (single-effect and double-effect) with different working media ($LiBr/H_2O$ and NH_3/H_2O) integrated with CAES and ORC in order to analyse the impact on the system performance.
- ✓ Parametric analysis of CCHP performance to study the effect of recuperator outlet temperature and ARS mass flowrate.
- ✓ Economic evaluation of the proposed D-CAES, ORC and different types of ARS.

For the stage one, the CCHP system was proposed and evaluated through simulation, parametric analysis and exergy analysis. For stage two, multi-objective optimisation and energy, exergy and economic analysis were performed to analyse the performance of CCHP system. For stage three, the performance of the CCHP system with different types of ARS is compared. The novel contributions of the PhD thesis include:

For stage one

- A new CCHP system composed of CAES, ORC and a single-effect ARS is proposed.

To achieve this target, simulation, energy and exergy analysis of CCHP system were carried out. The performance of CCHP system was evaluated. The main components and all model developed and validated. The detailed process description of the CCHP system is given. Several key parameters were chosen

to be analysed such as inlet mass flowrate of pump in ARS, inlet temperature of combustion chamber 1, different working fluids for ORC, ORC turbine inlet pressure and compressor inlet temperature.

For stage two

- A new process design was proposed for heat recovery in trigeneration system and simulation-based optimisation framework is developed to optimize the RTE and cost.

Further investigation (a multi-objective optimisation and synthetically considering energy, exergy and economy) is needed and performed. The performance analysis methodologies were carried out. The optimisation framework of CCHP was proposed. The multi-objective optimisation results and analyse the impact of different working fluids on the CCHP system were demonstrated by energy, exergy and economic analysis.

For stage three

- Different types of ARS (single-effect and double-effect) with different working media integrated with CAES and ORC are compared to analyse the impact on the system performance.

The ARS only operated during the discharging process. Under the design conditions, the waste low-grade heat from the flue gas was all used for supplying ARS. The performance of the CCHP system with different types of ARS is compared. The different cycles and different working media of ARS were compared to analyse the effects on the CCHP performance. The process analysis and energy and economic analysis were performed.

1.8 Scope of this study

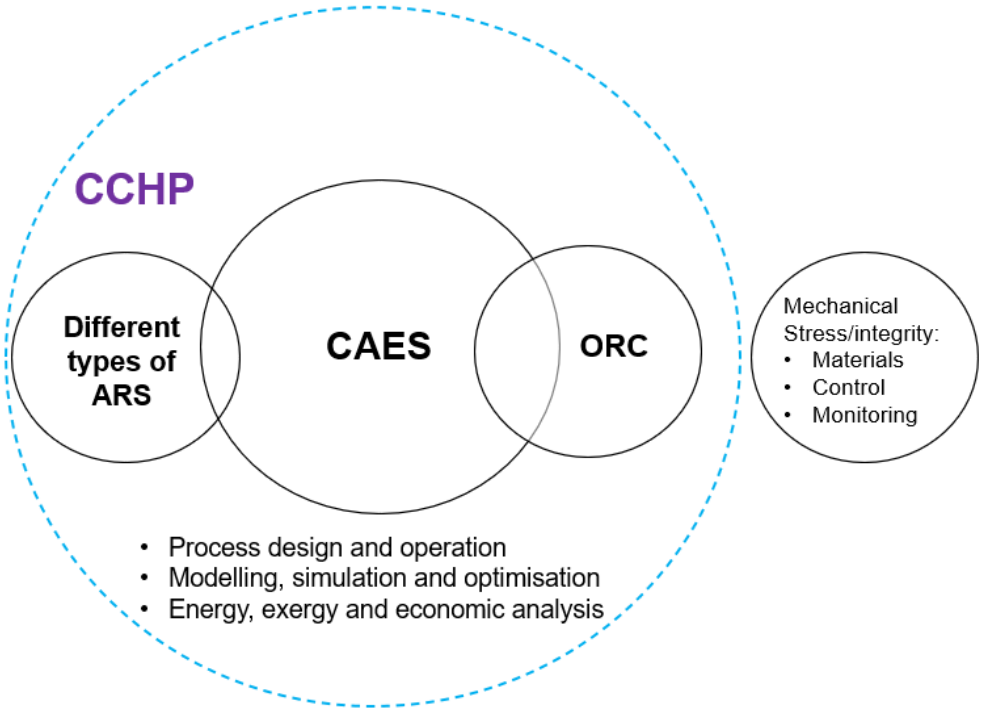

Figure 1-20 Overview of the scope of this thesis

The primary focus of this investigation pertains to the CAES system. The scope of this PhD study is presented in Figure 1-20, where the boundary is depicted by a blue dashed line. The interconnected systems are denoted by black circles, exemplifying the integration of various components such as the CCHP system, CAES, ORC, LiBr/H_2O ARS and different types of ARS. The research methodology encompasses simulation and optimisation techniques, involving energy, exergy and economic analyses to evaluate the performance of the CCHP system. It is important to note that this study does not entail experimental investigations and therefore does not address mechanical stress or system integrity concerns, such as materials, control and monitoring aspects.

1.9 Research methodology

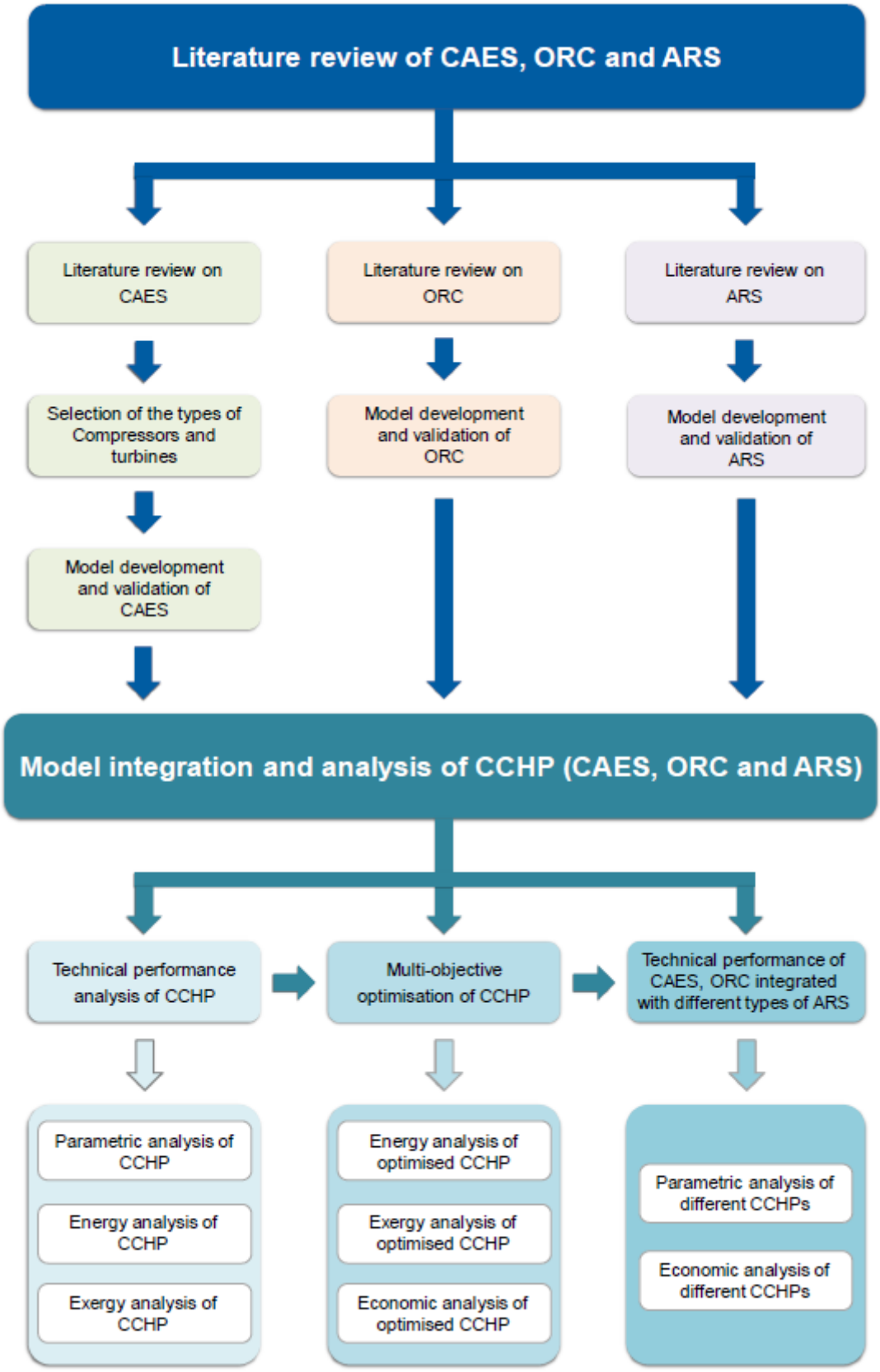

Figure 1-21 Overview of research methodology

Figure 1-21 shows the research methodology implemented in this thesis to achieve its aim and objectives.

1.10 Software tools used for this study

1.10.1 Aspen Plus®

Aspen Plus® is a highly sophisticated software tool designed for process modelling, simulation and optimisation in the fields of chemical engineering, petrochemical industries and power generation plants. It encompasses comprehensive model libraries that encompass a wide range of unit operations encountered in these industries. Additionally, the integration of Aspen Properties® software provides Aspen Plus® with an extensive physical property database, enabling accurate and reliable simulations (Dyment and Mantrala, 2015; Olumayegun, 2017). In this study, Aspen Plus® was employed for the simulation of the CAES, ORC and different types of ARS. The use of Aspen Plus® is specifically discussed in Chapter 3, where the development of steady-state simulation for the CCHP system is presented. Aspen Plus® was chosen due to its robust capabilities in simulating processes involving complex chemical reactions, as well as heat and mass transfer phenomena.

1.10.2 Aspen Process Economic Analyzer®

APEA is a software tool used for cost estimation to calculate both capital expenditures and operating expenses associated with a process system (AspenTech, 2018b). In the context of this study, APEA was employed to assess various costs, including capital costs, operating costs and the levelized cost of electricity (LCOE) for both the CAES system and the integrated system. APEA employs a bottom-up approach for cost evaluation, relying on historical data derived from real projects, apart from specialized equipment or units. APEA allows for the remapping and resizing of each equipment or unit within a system model created using Aspen Plus®. However, it should be noted that the model generated by Aspen Plus® cannot be directly used within APEA due to potential discrepancies with the design parameters of real plants (e.g. flowrate, area and volume). APEA has the capability to re-evaluate each equipment based on real data obtained from its extensive database (as discussed in Chapter 5 and Chapter 6).

1.10.3 MATLAB

MATLAB (matrix laboratory) is a high-level programming language and interactive environment for numerical computation and visualisation. MATLAB allows development of algorithms, creation of models and user interfaces, plotting of functions and data and interfacing with programs. It can be written in other languages (MathWorks, 2014). Simulink is an additional package that adds multi-domain simulation and model-based design. The non-dominated sorting genetic algorithm (NSGA-II) combining with Aspen Plus® and MATLAB capability is adopted to optimise CCHP in this study (discussed in Chapter 5).

1.11 Outline of this thesis

Chapter 2 provides a comprehensive review of the current state of research and development in CAES, ORC, ARS and CCHP technologies. It offers an up-to-date assessment of the ongoing research efforts and advancements in these fields. It also provides an overview of significant CAES programs, experimental/pilot plants and commercially operational facilities. Notably, the performance criteria that are crucial for evaluating the effectiveness and efficiency of these systems are highlighted, emphasizing key parameters and metrics.

Chapter 3 focuses on the development of steady-state models for CAES, ORC and ARS. The chapter begins by describing the process of model development, highlighting the key considerations and parameters involved. The developed models are then verified by comparing results with those obtained from existing models found in the literature.

Chapter 4 presents the steady-state thermodynamic performance analysis of CCHP. By employing exergy analysis, the chapter provides a comprehensive understanding of the thermodynamic efficiency and effectiveness of the system components. Technical performance analysis of the CAES system integrated with ORC is investigated with the discussion of the effects of different factors.

Chapter 5 presents multi-objective optimisation for the CCHP system. Different working fluids of ORC were compared to evaluate the performance of CCHP system. The CCHP system is subjected to detailed thermodynamic analysis, specifically energy and exergy analysis, to gain comprehensive insights into its

performance. Additionally, an economic analysis is conducted to assess the financial aspects of the system.

Chapter 6 proposes different types of ARS (single-effect and double-effect) using different working media integrated with CAES and ORC. Parametric analysis of CCHP performance was carried out to study the effect of recuperator outlet temperature and ARS mass flowrate. Economic evaluation of the proposed D-CAES, ORC and different types of ARS systems are performed.

Chapter 7 draws conclusions for the whole study and recommendation for future work.

2. Literature review

2.1 Overview

This chapter aims to provide a comprehensive overview of the state-of-the-art research activities related to CAES systems. Different aspects (including commercial plants, pilot plants, laboratory rigs and planned projects) will be thoroughly examined and presented. Furthermore, a comprehensive review of research methodologies employed in the analysis of CAES systems (such as modelling, simulation and optimisation techniques) will be conducted. Moreover, strategies for enhancing the overall performance of CAES systems will be introduced. Additionally, this chapter will encompass an in-depth review of the modelling, simulation and performance criteria of CCHP systems integrating CAES, ORC and ARS.

2.2 CAES commercial plants

2.2.1 Huntorf CAES plant

Two large-scale industrial CAES plants, operating under the D-CAES type, have been successfully deployed for commercial service. These plants, with a capacity exceeding 100 MW, have demonstrated consistent operational performance (Budt et al., 2016). The first commercial plant, known as the Huntorf CAES plant, was commissioned in 1978 in Germany (Chen et al., 2012; Meng et al., 2019). It has two caverns that comprise a total of 310,000 m^3. Figure 2-1 provides an illustration of the Huntorf CAES plant, which uses two separate turbo-compressor units and incorporates a pre-cooling process for the

incoming air within the cavern. In 2006, an expansion of the plant resulted in a reduction of the high-pressure turbine inlet temperature from 550°C to 490°C, while maintaining the inlet pressure. The output power increased from 290 MW to 321 MW and the discharging time increased from 2 hours to 3 hours.

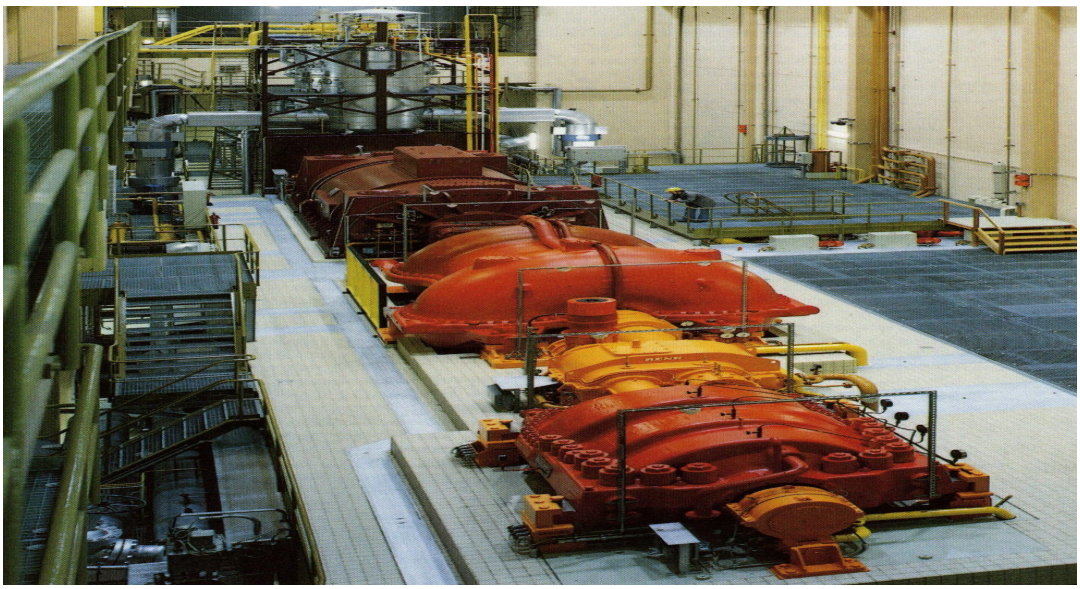

Figure 2-1 Huntorf CAES plant (Budt et al., 2016)

2.2.2 McIntosh CAES plant

Figure 2-2 McIntosh CAES plant (Venkataramani et al., 2016)

In 1991, the second D-CAES plant was established in McIntosh, Alabama, USA, with an output capacity of 110 MW (as shown in Figure 2-2). The McIntosh

CAES plant follows a similar construction arrangement as the Huntorf CAES plant, with the motor-generator positioned on a single shaft. The air compression unit uses a salt cavern with a storage capacity of 538,000 m^3 (Budt et al., 2016). It is important to note that all D-CAES systems are equipped with a combustor and require fuel for combustion, which can potentially give rise to environmental concerns. Despite this, no additional large-scale (>100 MW) commercial CAES plants have been constructed since the establishment of the McIntosh plant (Budt et al., 2016).

2.2.3 Comparison between Huntorf and McIntosh CAES plant

A comparative analysis of the design specifications is presented in Table 2-1. Notably, the McIntosh CAES plant has a higher RTE of 54% compared to Huntorf's RTE 42% (Budt et al., 2016; Meng et al., 2019). In terms of design considerations, the Huntorf CAES plant with shorter charging and discharging time aims to facilitate reserve power and black-start capability. As Huntorf CAES functions primarily as a reserve power source, minimizing energy consumption becomes more critical (Radgen, 2008; Budt et al., 2016). Conversely, the design of the McIntosh CAES plant emphasizes achieving high RTE and extending charging and discharging times.

Table 2-1 Comparison of Huntorf CAES plant and McIntosh CAES plant (Radgen, 2008; Kaiser, 2015; Budt et al., 2016)

Technical data	**Huntorf**	**McIntosh**
Operating company	E. ON Kraftwerke	PowerSouth
Operation year	1978	1991
Rated power output	290 MW	110 MW
Compressor manufacturer	Sulzer (today MAN Turbo)	Dresser-Rand
Compressor units	2	4
Compressor Type	LP Axial and HP Centrifugal	One LP Axial, two intermediate Centrifugal and one HP Centrifugal

Number of stages	20 and 6	15,8,8 and 6
Compressor max input power	60 MW	50 MW
Air mass flowrate in c harging proc ess	108 kg/s	90 kg/s
Charging time	8h	40 h
Disc harging time	2-3h	26h
Cavern pressure range	46-72 bar	46-75 bar
Caver Volume	310.000 m3	538,000 m?
Number of Cavem	2	1
RTE	42%	54%
Turbine manufacturer	BBC (today Alstom)	Dresser-Rand
Air mass flowrate in discharging process	417 kg/s	156 kg/s
Turbine start-up time	>9 min	14 min

Figure 2-3 provides an overview of the different components comprising the Huntorf and McIntosh CAES plants. The Huntorf CAES plant and the McIntosh CAES plant are characterized by the absence of waste heat recovery devices. In the McIntosh CAES plant, waste heat losses are minimized through the implementation of recuperator (see the red circle).

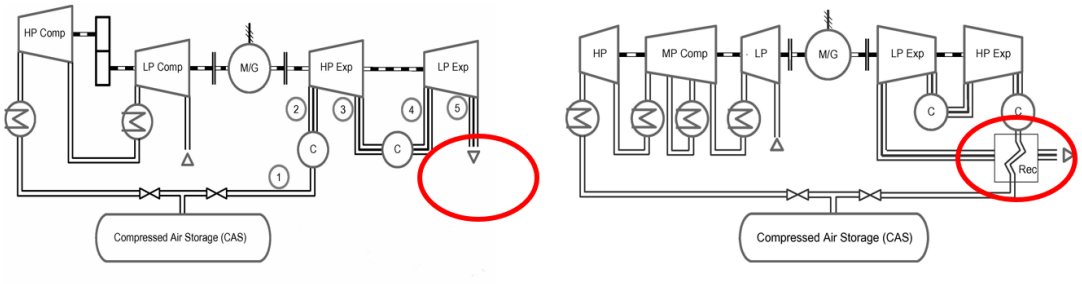

Figure 2-3 Block flow diagram of Huntorf CAES plant (left) and McIntosh CAES plant (right) (Budt et al., 2016)

2.3 CAES pilot plants

2.3.1 A-CAES pilot plants

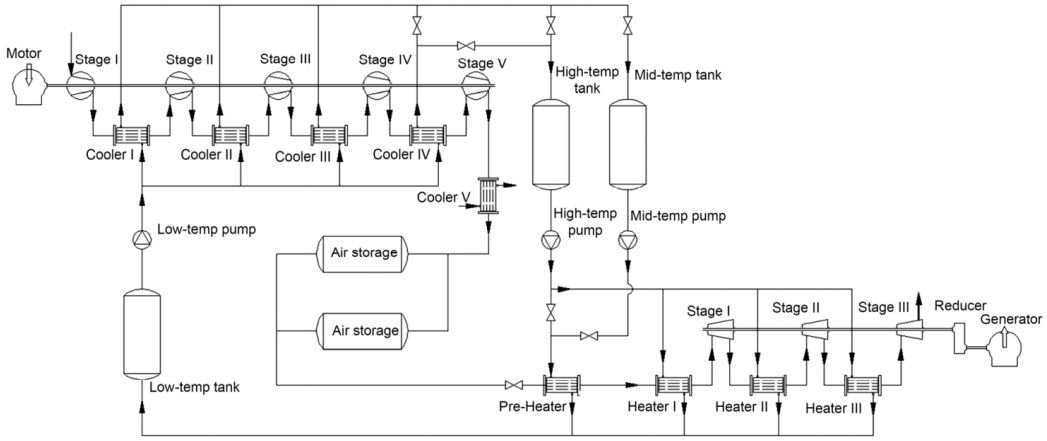

Figure 2-4 The schematic diagram of TICC-500 (Mei et al., 2015)

Over the past two decades, the implementation of CAES systems has grown faster all over the world. Consequently, several pilot plants have been designed with the aim of investigating RTE, conducting partial testing and demonstrating the feasibility of CAES technology. It is worth noting that the A-CAES system without TES has been identified as having significant drawbacks, as discussed in Chapter 1. To date, no pilot plant worldwide has been reported to operate specifically as an A-CAES system without TES. In this section, two pilot plants that incorporate the A-CAES system with TES will be reviewed.

In November 2014, the State Grid Corporation of China (SGCC) funded the construction of the world's first pilot plant for A-CAES with TES in Wuhu City, Anhui Province, China (Wang et al., 2016; Mei et al., 2015). This pioneering system (as shown in Figure 2-4), named TICC-500 (Tsinghua-IPCCAS-CEPRICAES), boasts a power rating of 500 kW. The storage unit comprises two steel pressure storage tanks, with each tank having a volume of 50 m^3 and operating pressure ranging from 2 MPa to 10 MPa (Mei et al., 2015). The TICC-500 project is led by Tsinghua University, in collaboration with the Institute of Physics and Chemistry, Chinese Academy of Sciences (IPC, CAS), and the China Electric Power Research Institute (CEPRI) (Wang 2017; Wang et al., 2016; Mei et al., 2015).

2.3.2 AA-CAES pilot plant

AA-CAES represents a high-temperature variant of the A-CAES process. During the charging phase, AA-CAES uses a TES working medium to capture and store the heat generated from compression (Budt et al., 2016; Zhou et al., 2019). The adiabatic nature of the process ensures that no net additional energy is consumed during the system's charge and discharge cycles. AA-CAES exhibits many advantages, including high energy storage density, exceptional energy storage efficiency, reliance solely on renewable energy sources, extended energy storage durations, environmental preservation through green technologies and considerable adaptability (Budt et al., 2016; Wang et al., 2017; Meng et al., 2019). By effectively recovering the heat generated during the air compression process, the RTE of the energy storage system can be significantly enhanced, theoretically reaching up to 70%.

In 2016, the ALA CAES group, in collaboration with the Swiss Federal Office, successfully constructed and tested the first pilot plant using AA-CAES technology (Figure 2-5). Situated in the Swiss Alps near the city of Biasca, this pilot plant was designed with a power rating of 1 MW and achieved an impressive RTE of 72%. To ensure proper pressure containment, the storage used a decommissioned transportation tunnel, which was sealed with two conical concrete plugs, each measuring 5 meters in thickness. Geissbühler et al. (2018) assessed the AA-CAES plant's RTE and reported values ranging from 63% to 74%. For now, many research efforts are focused on improving the performance of sensible TES systems. Becattini et al. (2018) demonstrated the potential of sensible/latent TES as an appealing option for large-scale high-temperature storage. Geissbühler et al. (2018) concluded that the TES system achieved energy efficiency between 77% and 91% and exergy efficiency between 72% and 89%. However, due to leakage issues primarily arising from the concrete plugs, the cavern had to be temporarily closed for repairs.

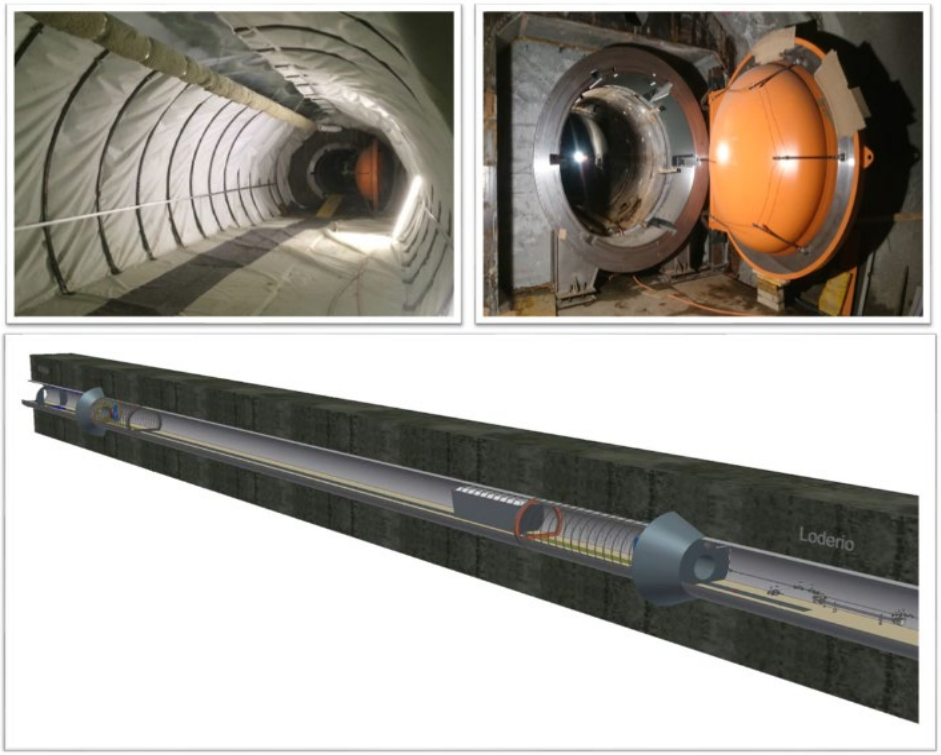

Figure 2-5 ALA CAES 1 MW AA-CAES pilot plant (Geissbühler et al., 2018)

Figure 2-6 Guizhou Bijie 10 MW AA-CAES pilot plant (Wang et al., 2017)

Additionally, a pilot plant for an AA-CAES system was designed in collaboration between the Energy Storage R&D Center and the Institute of Engineering Thermophysics, Chinese Academy of Sciences (IET, CAS), featuring a power output rating of 10 MW and a targeted RTE of 70%. This plant has been

operational and under testing since 2016 (Figure 2-6). Ongoing research endeavours are investigating the performance of the 10 MW AA-CAES pilot plant (He and Wang, 2018).

2.3.3 Supercritical CAES (SC-CAES) pilot plant

The supercritical compressed air energy storage (SC-CAES) system involves compressing air to the supercritical state and storing the heat generated during the charging phase (Letcher, 2020). The compression heat is subsequently stored in the cold heat exchanger, where it is utilized to liquefy the supercritical air and store it in a low-temperature storage tank. During the discharge process, a cryogenic pump compresses the liquid air back to a supercritical state, releasing the stored compression heat from the tanks (Wang et al., 2017).

Figure 2-7 Hebei Lang fang 1.5 MW SC-CAES pilot plant (Wang et al., 2017)

Figure 2-7 illustrates a 1.5 MW SC-CAES pilot plant designed by the IET, CAS in 2013. Located in Lang fang City, Hebei Province, the project received funding from Macao energy Industry Park Development Co. Ltd. The schematic diagram of the SC-CAES plant is depicted in Figure 2-8.

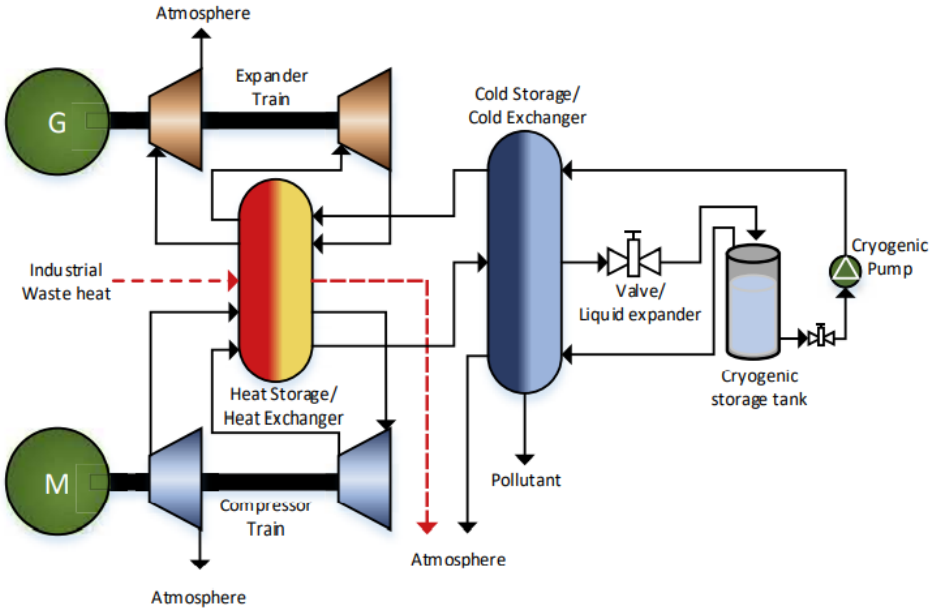

Figure 2-8 SC-CAES pilot plant (Guo et al., 2016)

The SC-CAES pilot plant has successfully operated for over 4000 hours (Wang et al., 2017; Meng et al., 2019). A study conducted by Guo et al. (2016) demonstrated that the SC-CAES system exhibits an energy density 18 times higher than that of the D-CAES system. Additionally, the compressor was identified as the component causing the most significant exergy destruction, followed by the expander. Guo et al. (2017) further investigated system optimisation and found that the RTE of the SC-CAES system can reach 55%.

2.3.4 I-CAES pilot plant

A pilot plant with a rated power of 1.5 MW (Figure 2-9) was designed by the Thayer School of Engineering at Dartmouth College in 2007. This project was executed by SustainX Inc. located in Seabrook, New Hampshire, USA. Piston machinery serves as the fundamental component for I-CAES systems and offers the best approximation for achieving high RTE performance (Budt et al., 2016). I-CAES aims to maintain a relatively constant temperature throughout the process. The I-CAES system used water as an ideal working medium due to its high heat capacity. The pilot plant consists of three low-pressure (0-12.4 bar) and three high-pressure (12.4-206.8 bar) compressor stages. One advantage of this system is its ability to reach full power in less than one minute. Although the RTE of the project was designed to be 90%, Bollinger (2015)

evaluated its performance and concluded that the RTE could achieve the target of 55%. The main reason is that dynamic performance characteristic of compressed air storage has effect on design capacity of first heat exchanger of expansion train.

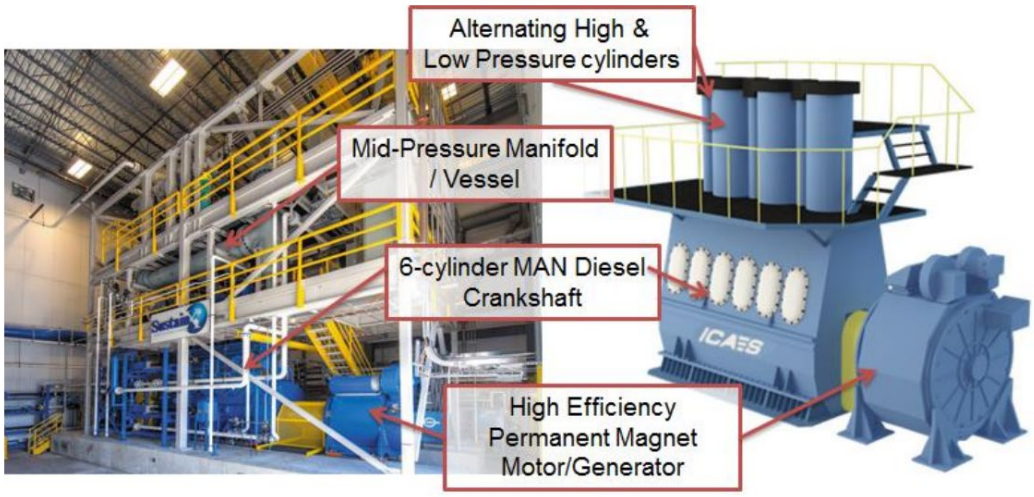

Figure 2-9 1.5 MW I-CAES pilot plant (Bollinger, 2015)

In 2013, General Compression Inc., a company founded by ConoCOPhillips, designed and built a 2 MW-rated power I-CAES pilot plant called General Compression Advanced Energy Storage (GCAES™). This pilot plant, integrated with a wind turbine, commenced operation in 2013 and is situated in Gaines, Texas, United States.

2.4 Lab rigs for CAES

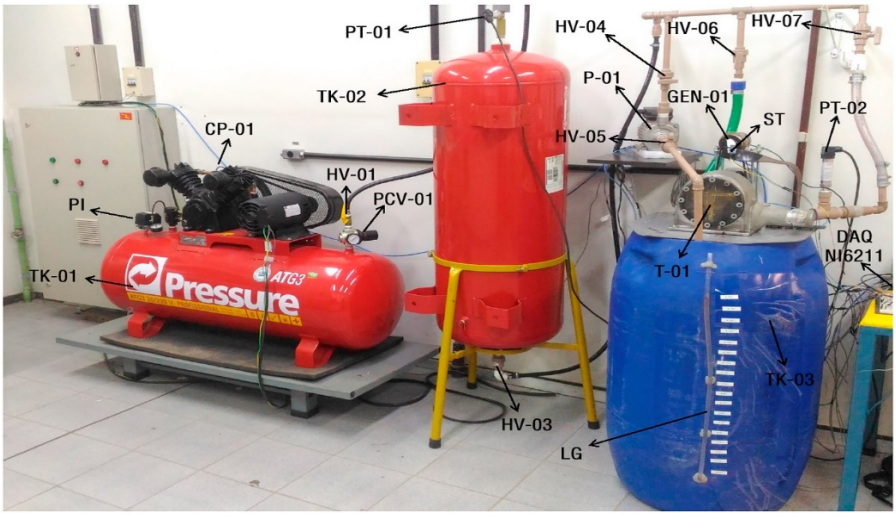

Figure 2-10 The experimental setup of PH-CAES system (Camargos et al., 2018)

Camargos et al. (2018) proposed a Pumped Hydro-Compressed Air Energy Storage System (PH-CAES) that incorporates hydraulic turbines and eliminates the need for an external heat source, thereby reducing fossil fuel combustion and heat losses. Figure 2-10 illustrates the experimental setup of the PH-CAES system.

The PH-CAES system's primary operational processes consist of water charging, air charging and power generation. It was concluded that the system's performance is influenced by turbine inlet pressure and the power conversion efficiency is predicted to reach 45%. Pottie et al. (2019) developed and tested a novel sequence of operation for the PH-CAES system. The results indicated that the RTE of the laboratory-scale PH-CAES simulation, with operational pressures ranging from 300 kPa to 800 kPa, reached 42%.

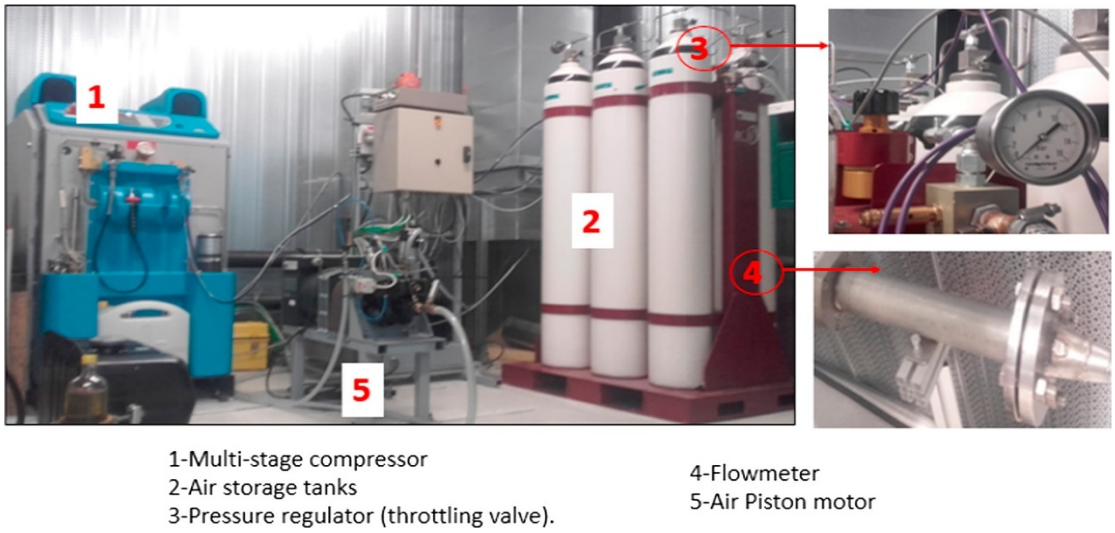

Figure 2-11 The lab photo of T-CAES (Cheayb et al., 2019)

Cheayb et al. (2019) developed a trigenerative compressed air energy storage system (T-CAES) that integrates compressors, heat exchangers, regulation valves, a storage tank, thermal energy storage and an expander. Figure 2-11 presents the experimental setup of the T-CAES system. The charging phase of the study was conducted at a room temperature of 22°C, with the input power increased up to a maximum of 3.6 kW.

During the discharging process, at a room temperature of 26.4°C, the pressure in the air storage unit decreased from 301 bar to 9 bar. The results of this study demonstrate the feasibility of the T-CAES system with an error margin of no

more than 13.2%. The reason is that the error during the charge phase. It should be noted that the T-CAES system is currently limited to small-scale applications.

Li et al. (2012) developed a novel micro-scale trigeneration system. The trigeneration system, as shown in Figure 2-12, offers excellent flexibility and a simple configuration. The experimental system is currently under construction, and for average detailed efficiencies of approximately 50% in winter and 35% in summer. The total efficacies were found to be 45% and 25%, respectively.

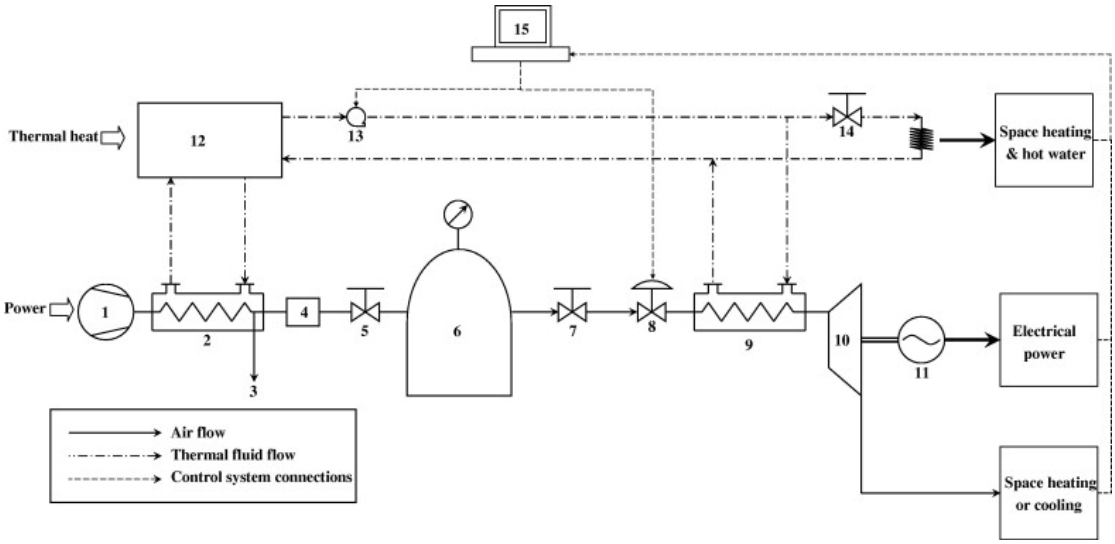

Figure 2-12 Micro-trigeneration system (Li et al., 2012)

2.5 Planned CAES projects

Being a well-established and large-scale energy storage technology, CAES has garnered sustained interest since its initial demonstration. This has resulted in the emergence of many significant CAES projects, both commercial and demonstrative, in recent years. A comprehensive overview of these projects can be found in Table 2-2. From the recent significant developments in CAES, it becomes apparent that there are notable hurdles in transitioning this technology into a viable commercial operation. Several meticulously planned and highly advanced projects, exemplified by ADELE and Norton initiatives, have encountered setbacks and ultimately failed, with economic factors primarily accounting for these shortcomings. The more promising AA-CAES technologies, anticipated to enter operational phases shortly, still need to catch up to the scalability of conventional gas-fired CAES facilities.

Table 2-2 Summary of planned projects (King et al., 2022; Ding et al., 2022; Budt et al., 2016)

CAES Project	CAES Technology	Location	Power output	Date	Current Status
Norton CAES plant	D-CAES	Norton, Ohio, USA	270 MW	2001-2003	Not realised
GAELECTRIC CAES plant	D-CAES	Islandmagee, Co Antrim, UK	200-330 MW	2008-2019	Not realised
Seneca CAES plant	D-CAES	Reading, New York, USA	130-210 MW	2010-2012	Not realised
ADELE CAES plant	AA-CAES	Staβfurt, Germany	200 MW	2010-2016	Discontinued
SustainX CAES plant	I-CAES	Seabrook, New Hampshire, USA	1.65-2.2 MW	2013-2015	Discontinued
Jintan CAES plant	AA-CAES	Jintan, Jiangsu, China	50-60 MW	2017-present	Commissioned
Texas CAES plant	D-CAES	Tennessee Colony, Texas, USA	324-487 MW	2019-present	Not realised
Feicheng CAES plant	AA-CAES	Feicheng, Shandong, China	300 MW	2019-present	Active
Zhangjiakou CAES plant	AA-CAES	Zhangjiakou, Hebei, China	100 MW	2020-present	Active
PG&E CAES plant	D-CAES	San Joaquin County, California, USA	300 MW	2020-present	Commissioned
Huaian CAES plant	AA-CAES	Huaian, Jiangsu, China	465 MW	2022-present	Commissioned
Angas CAES plant	AA-CAES	Strathalbyn, South Australia, Australia	5 MW	2022-present	Commissioned
Taian CAES plant	AA-CAES	Taian, Shandong, China	200 MW	2023-present	Commissioned

2.6 Modelling and simulation of CAES

Modelling and simulation of CAES systems encompass two key aspects: steady-state modelling and simulation, as well as dynamic modelling and simulation. Both steady-state and dynamic modelling and simulation play vital roles in advancing the understanding, optimisation and control of CAES systems. They serve as valuable tools for system design such as solid oxide fuel cell (SOFC), kalina cycles (KCS) and ground source heat pump (GSHP), performance evaluation and guiding the development of innovative strategies to enhance the efficiency, reliability and overall performance of CAES technologies.

Steady-state modelling and simulation involve the development of mathematical models that capture the thermodynamic processes and operational characteristics of CAES systems. Dynamic modelling and simulation, on the other hand, focus on capturing the transient behaviour and response of CAES systems. Table 2-3 shows the summary of CAES integrated with different systems reported. It is no surprise that most researchers have focused their studies on D-CAES. One reason for this preference is the availability of research data, with a significant portion currently accessible as D-CAES data. Another factor is the existing limitation in A-CAES due to the materials used for insulation, which still needs to be solved. Traditionally, the efficiency of conventional D-CAES systems is determined by the maximum operating temperature, relying on the Carnot efficiency principles applicable to heat engines. In contrast, the cycle efficiencies of storage systems with a single electrical input associated with A-CAES theoretically remain unaffected by the maximum operational temperature or storage temperature.

Table 2-3 Summary of CAES integrated with different systems reported

CAES Type	System Configuration	Research Methodology	Steady-State or Dynamic	Power Output	RTE	References
D-CAES	SOFC+CAES	Energy and Economic Analysis	Steady-State	200 MW	65.00%	Nease and Adams (2013)

D-CAES	CAES-CC	Energy, Exergy and Optimisation Analysis	Steady-State	349.1 MW	50.00%	Liu et al. (2014)
D-CAES	CAES+KCS	Energy and Exergy Analysis	Steady-State	290 MW	47.64%	Zhao et al. (2015)
D-CAES	CAES+ORC	Energy and Economic Analysis	Steady-State	205.8 MW	63.24%	Meng et al. (2018)
D-CAES	Wind+CAES+ ORC	Energy and Economic Analysis	Pseudo-dynamic	75.5 MW	54.34%	Meng et al. (2019)
D-CAES	CAES+GSHP	Energy and Economic Analysis	Steady-State	1.1 MW	90.06%	Zhang et al. (2019)
D-CAES	CAES+ORC+ SOFC	Energy and Exergy Analysis	Steady-State	250.93 kW	76.07%	Zhang et al. (2021)
D-CAES	CAES+ORC+ ARS	Energy and Exergy Analysis	Steady-State	234.2 MW	66.35%	Ding et al. (2022)
D-CAES	CAES+ORC+ ARS	Energy, Exergy, Economic and Optimisation Analysis	Steady-State	234.2 MW	68.38%	Liu et al. (2022)
A-CAES	A-CAES+ARS	Energy and Exergy Analysis	Steady-State	1000 kW	66.98%	Liu and Wang, (2016)
A-CAES	A-CAES-TES	Energy Analysis	Steady-State	100 MW	77.00%	Tola et al. (2017)
A-CAES	A-CAES-TES	Energy Analysis	Steady-State	1000 kW	56.20%	Guo et al. (2017)
A-CAES	A-CAES	Energy and Exergy Analysis	Steady-State	1000 kW	72.34%	Chen et al. (2018)
A-CAES	A-CAES-TES+ARS	Energy, Exergy, Economic and Optimisation Analysis	Steady-State	100 MW	91.00%	Han et al. (2020)
D-CAES	CAES	Energy and Economic Analysis	Dynamic	290 MW	42.00%	Raju and Khaitan (2012)
D-CAES	Wind+CAES	Energy and Economic Analysis	Pseudo-dynamic	290 MW	42.00%	Maton, et al. (2013)
D-CAES	D-CAES	Energy and Exergy Analysis	Pseudo-dynamic	290 MW	42.00%	Zhang et al. (2019)
A-CAES	A-CAES-TES	Energy Analysis	Dynamic	40MW	69.00%	Wolf, (2011)
A-CAES	A-CAES-TES	Energy Analysis	Dynamic	290 MW	56.50%	He et al. (2017)

A-CAES	A-CAES-TES	Energy Analysis	Dynamic	220 MW	74.00%	Sciacovelli et al. (2017)
A-CAES	A-CAES-TES	Energy Analysis	Dynamic	2 MW	58.99%	Luo et al. (2018)
A-CAES	A-CAES+ARS	Energy and Economic Analysis	Pseudo-dynamic	1.5 MW	68.00%	Li et al. (2022)

2.7 Ways to improve RTE of CCHP

2.7.1 CAES integrated with ORC or Kalina cycle or ARS

The use of the ORC holds significant potential in enhancing energy efficiency through the effective utilization of waste heat, primarily due to the implementation of organic fluid as the working medium, as highlighted in Liu et al. (2004). The salient virtue of such an integrated system is the conversion of waste heat into electrical energy, a process that underscores the potent recyclability inherent to this approach (Quoilin et al., 2013). A ground-breaking ORC was proposed by Mohammadi et al. (2017), integrating ORC and ARS (using toluene as the organic working fluid). Evaluations revealed a remarkable elevation of RTE, reaching a ceiling of 53.94%. Sadreddini et al. (2018) later innovated on this basis, implementing a CAES system that also used toluene as the working fluid in the ORC, thereby escalating the RTE to an impressive 71.87%. It should be noted that while the working fluid remained consistent across these two studies, the selection of varying working fluids can also exert substantial influence on the performance of the integrated system. Multiple scholarly investigations have highlighted the importance of selecting working fluids in the ORC that are both economically viable and possess lower toxicity profiles (Desai and Bandyopadhyay, 2016; Meng et al., 2018; Soltani et al., 2020). For instance, Desai and Bandyopadhyay (2016) scrutinized several organic working fluids in the context of an ORC integrated with solar energy, with their findings suggesting R113 as a cost-effective choice. Meng et al. (2018) took this a step further, designing an ORC equipped with a recuperator to reclaim waste heat, using a palette of five distinct working fluids. Their results indicated that the use of R123 could boost the RTE of the integrated system by a substantial 6.7%.

Introduced in 1980 by the Russian scientist Alexander Kalina, the Kalina cycle, with its pioneering utilization of an NH_3/H_2O working fluid, brought a new perspective to the exploitation of waste heat from gas turbine exhausts (Kalina, 1982). This approach proved beneficial in enhancing the performance of integrated systems, as demonstrated by Mokarram and Mosaffa (2018). This concept was further substantiated by Zhao et al. (2015), who developed a robust, steady-state mathematical model of an integrated energy system amalgamating CAES and the Kalina cycle. Their findings suggested that the integrated system's exergy efficiency could be improved by approximately 4% compared to a standard D-CAES system. Comparative analyses conducted by Soltani et al. (2020) using the ORC and the Kalina cycle, combined with a CAES system, indicated the interplay of the first and second laws of thermodynamics. The ORCs, using different working fluids (R717, R1270, R290 and R1234yf), were compared with Kalina cycles (KCS11 and KCS34). R290 emerged as the superior working fluid, achieving the maximum waste heat recovery.

2.7.2 A-CAES system or I-CAES system

Relevant research in CAES systems has provided critical insights into large-scale energy storage technologies. Notably, the RTE of A-CAES and I-CAES systems has been reported to surpass 75% in several studies, underscoring their potential for energy conservation (Meng et al., 2019; Zhou et al., 2019).

The A-CAES system offers the distinct advantage of eliminating the need for fuel combustion. The thermal energy generated during the expansion process can be harnessed and stored for subsequent air preheating. This underlines the necessity for more focused research on TES systems to optimize the performance of the A-CAES system (Zhang et al., 2013; Zhou et al., 2019).

The I-CAES system introduces a paradigm shift, distinguished by its remarkable RTE, spanning between 70-80%. The core innovation underpinning I-CAES stems from the deployment of piston machinery, which facilitates the attainment of desired isothermal compression and expansion. Currently, a growing contingent of scholars is turning their attention towards compressors and turbines/expanders to advance research in the area of near-isothermal compression/expansion (Letcher, 2020).

2.7.3 Integration with renewables and other energy storage technologies

With the rising adoption of renewable energy, the intermittent nature of wind and solar energy has surfaced as a challenge urgently requiring resolution. Coupling these renewable energy sources with CAES system presents an opportunity to enhance operational flexibility and ensure more consistent power production.

Mason et al. (2008) led the way with an integrated system combining photovoltaic (PV) electricity with a CAES system. Their results revealed that such an integration effectively mitigates the issue of intermittency while simultaneously driving down the cost of power generation. Subsequent research has concentrated significantly on wind power, yielding innovative solutions like wind-diesel-CAES hybrid and CAES-Wind systems (Meng et al., 2018; Sedighnejad, 2011). Pioneering work by Chen et al. (2017) introduced a CAES system coupled with wind and solar energy, with their technical feasibility analysis showing that such an integrated system offers practical solutions for the large-scale, continuous use of renewable energy.

The incorporation of CAES with other energy storage technologies holds the potential to amplify the efficiency of the resultant system. Such integration allows for the retention of a significantly larger volume of energy over extended durations. Additional benefits include faster reaction time and heightened energy densities (Letcher, 2020; Wang et al., 2017; Venkataramani et al., 2016).

Camargos et al. (2018) developed a novel PH-CAES system with hydraulic turbines. This design obviates the need for an external heat source, reducing fossil fuel combustion and heat loss. Their results indicated that the performance of the PH-CAES system was influenced by turbine inlet pressure, with power conversion efficiency projected to reach up to 45%. Meanwhile, Zhao et al. (2014) proposed a wind-hybrid energy storage system comprising an A-CAES and a flywheel energy storage system (FESS). This integrated system displayed superior performance in smoothing out wind power fluctuations, though their study did not include a comprehensive calculation of RTE.

2.8 Modelling/Simulation of CCHP

CCHP is often referred to as trigeneration. A CCHP system is a method of energy conservation that captures waste heat from power generation and uses it for heating and cooling purposes. A noteworthy contribution was made by Wang and Oliveira. (2006), which introduced a CAES-based vapour compression refrigeration system. A comprehensive energy and economic analysis indicated the structural is simple, the system excels in efficiency while maintaining low operational costs. Diving further into this field, Kim and Favrat (2010) conducted a rigorous examination of a small-scale trigeneration CAES system. This innovative system harnessed the heat generated from turbine exhaust and compression for heating and refrigeration applications. Mohammadi et al. (2017) extended the discourse by conducting an exergy analysis on a CCHP system integrated with a wind turbine and CAES system. Their study achieved a RTE of 53.94%. It indicated the highest exergy destruction to be generated in the wind turbine, followed by the combustion chamber and the CAES.

In a multi-objective optimisation study, Yao et al. (2017) performed an exergoeconomic investigation of a CCHP system. This system incorporated an NH_3/H_2O ARS, a gas engine and heat exchangers, all based on CAES. Wang et al. (2018) advanced this line of research by proposing a multi-objective optimisation of a gas turbine based CCHP system synergistically coupled with CAES and solar systems. Their findings showcased that the exergy efficiencies in optimal and maximum are 53.10% and 45.36%, respectively. Similarly, Razmi et al. (2019) presented a CCHP system based on wind turbines, CAES and ARS. Their system achieved an RTE of 56.71%. Ding et al. (2022) further broadened the horizon by proposing a CCHP system that incorporated CAES, an ORC and a single-effect $LiBr/H_2O$ absorption system. Under designated conditions, their system achieved an RTE of 66.35% and overall exergy efficiency of 51.21%.

2.9 Performance criteria of CCHP

2.9.1 RTE

The performance criteria of D-CAES systems are different from those of conventional power plants due to the charging process and the discharging

process at different time. Another reason is that the first law efficiency cannot be described for the CAES system. During the charging process, only the electrical energy is used for compressors work. The natural gas that combusts to heat compressed air is used to drive the gas turbine during the discharging process. Some waste heat in the gas turbine is recovered by the ORC and single-effect LiBr/H_2O absorption system. RTE is defined as the ratio of total energy output, comprising generated electricity of gas turbine and cooling energy, to the total energy input the general RTE of the CAES system (Budt et al., 2016; Meng et al., 2018; Ding et al., 2022):

$$\mathrm{RTE}_{CAES} = \frac{W_t}{E_{fuel} + W_{comp}} \qquad (2-1)$$

Where W_t is the output power of Turbine (kWh); W_{comp} is the electrical energy taken from grid for driving the compressors (kWh); E_{fuel} is the thermal energy of fuel consumed (kWh); Based on Eq. (2-1), the RTE of the CCHP system could be described as:

$$\mathrm{RTE}_{\mathrm{CCHP}} = \frac{W_t + W_{orc-c} + W_{orc-d} + Q_{cooling}}{E_{fuel} + W_{comp} + W_{ORC,p-c} + W_{ORC,p-d} + W_{LiBr,p}} \qquad (2-2)$$

Where W_{orc-c} is the output power of ORC in charging process (kWh); W_{orc-d} is the output power of ORC in discharging process (kWh); $Q_{cooling}$ is the output power of single-effect LiBr/H_2O absorption system. $W_{ORC,p-c}$ is the power consumption of ORC pump in charging process; $W_{ORC,p-d}$ is the power consumption of ORC pump in discharging process; $W_{LiBr,p}$ is the power consumption of pump in single-effect LiBr/H_2O absorption system.

2.9.2 Coefficient of performance (COP)

Furthermore, COP is defined as a ratio of useful cooling provided to work (energy) required that used for the different types of ARS, which can be defined as (Herold et al.,2016; Ding et al., 2022; Liu et al., 2022):

$$\mathrm{COP} = \frac{Q_{ARS,evap}}{Q_{ARS,desorber} + W_{ARS,pump}} \qquad (2-3)$$

2.9.3 Exergy efficiency

Exergy is defined as the maximum shaft work that a system can perform in a specified reference environment. Exergy analysis is a thermodynamic analysis technique that have resulted from the second law of thermodynamic, which indicates exergy destruction (Sadreddini et al., 2018; Ding et al., 2022; Liu et al., 2022).

The general exergy balance equation can be expressed as:

$$Exergy\ Input + Exergy\ Generation - Exergy\ Outpt - Exergy\ Consuption = Exergy\ Accumulation \quad (2-4)$$

The exergy of work and heat can be expressed as:

$$\dot{E}_x{}^{Q} = \left(1 - \frac{T_0}{T_i}\right)\dot{Q}_i \quad (2-5)$$

$$\dot{E}_x{}^{W} = \dot{W} \quad (2-6)$$

Where $\dot{E}_x{}^{Q}$ and $\dot{E}_x{}^{W}$ are exergy associated with heat and work; T_0 is the ambient temperature and T_i is the temperature of the heat transfer. The exergy of the stream can be divided into two parts, namely physical and chemical. The physical exergy is defined as:

$$\mathrm{e}x_{ph} = (h_i - h_0) - T_0(s_i - s_0) \quad (2-7)$$

Where h_i is enthalpy; h_0 is enthalpy at the reference state; s_i and s_0 are specific entropy, which related to different streams. The entropy term $(s_i - s_0)$ is defined as:

$$s_i - s_0 = C_{avg} ln \frac{T_i}{T_0} \quad (2-8)$$

Where C_{avg} is the average specific heat capacity of the substance.

The chemical exergy is defined as:

$$ex_{ch} = \sum_{i=1}^{N} y_i ex_i^{ch} + RT_0 \left(\sum_{i=1}^{N} y_i In(y_i)\right) \quad (2-9)$$

The ex is the sum of physical and chemical exergy which can be calculated by the following equation:

$$ex = ex_{ph} + ex_{ch} \quad (2-10)$$

Based on the above equations, exergy balance could be expressed as:

$$\dot{E}_x{}^{Q} + \sum \dot{E}x_{in} = \sum \dot{E}x_{out} + \dot{E}_x{}^{w} + \dot{E}_x{}^{D} \quad (2-11)$$

Where the $\dot{E}_x{}^{D}$ is exergy destruction of the component. Total exergy destruction can be defined as:

$$\dot{E}x_{total}^{D} = \sum \dot{E}_x{}^{D} \quad (2-12)$$

2.10 Summary

This chapter provides a critical review of various research domains within the sphere of CAES systems. It explores the commercial and pilot plants, lab-based experimental setups and planned CAES projects. It also explores the modelling and simulation of CCHP. It further delves into the improvement of integrated system performance, utilizing tools such as modelling and simulation. This analysis includes systems integrated with ORC, renewable energy sources and other subsystems.

Approaches to enhance the RTE of integrated systems are also examined, encompassing integration of CAES with ORC and a single-effect ARS, alongside A-CAES or I-CAES systems. Integration with renewable energy sources or other energy storage technologies is also discussed, illuminating the potential of these integrations to facilitate smoother operation of large-scale grids and tackle the issue of renewable energy intermittency. The following research knowledge gap has been identified:

- The RTE of CAES is still needed to be improved.
- The CAES could integrated with ORC and single-effect LiBr/H_2O ARS to recover the low-grade waste heat.
- A newly proposed CCHP system (CAES, ORC and single-effect LiBr/H_2O ARS) is analysed and simulation-based optimisation framework to optimize the RTE and cost.

- Different types of ARS (single-effect and double-effect) with different working media (LiBr/H_2O and NH_3/H_2O) integrated with CAES and ORC are compared to analyse the impact on the system performance.

This PhD thesis aims to address the gaps as summarised above through a comprehensive analysis the CAES, ORC and ARS.

3. Simulation and Model Validation

3.1 Overview

In this chapter, the development of the steady-state models to be employed for the thermodynamic performance analysis of CCHP system is presented. The CCHP system is comprised of CAES, ORC and ARS. Process simulation of each subsystem (e.g. CAES, ORC and different types of ARS) will be presented in Sections 3.2, 3.3, 3.4 and 3.5 respectively. Each subsystem has been validated separately because the proposed system is yet to be built. The conclusion of this chapter is given in Section 3.6.

3.2 Simulation and model validation of CAES system

Adopted from the selected D-CAES system is shown in Figure 3-1. One reason for choose D-CAES preference is the availability of research data, with a significant portion currently accessible as D-CAES data. Another factor is the existing limitation in A-CAES due to the materials used for insulation, which still needs to be solved. The key components of the D-CAES system include multi-stage centrifugal compressors (i.e. six HPCs and one LPC), cavern (CAVERN), recuperator (REC), combustors (COM1 and COM2) and turbines (HPT and LPT). The process of D-CAES is divided into the charging process and discharging process.

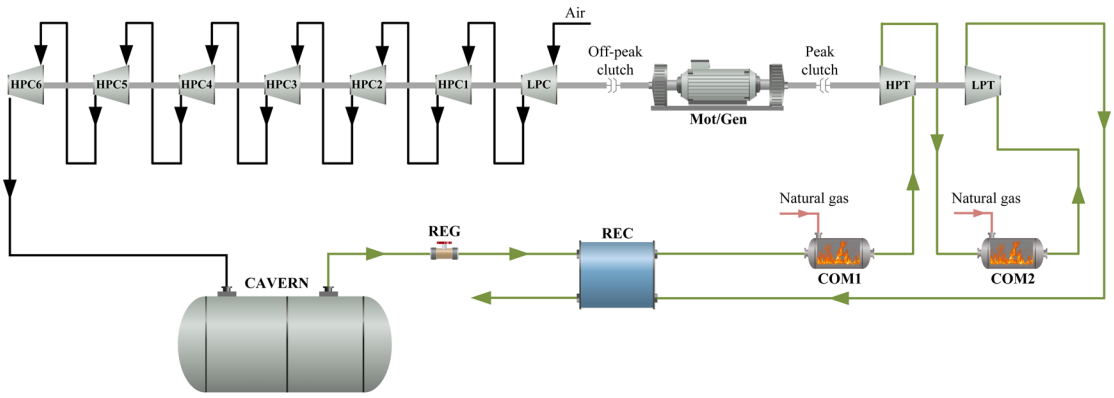

Figure 3-1 A simulation flowsheet of D-CAES

In the proposed D-CAES system, the use of a multi-stage centrifugal compression stage (6 intercooled stages) improves the efficiency due to the reduction of the gross energy demand of the machine (Meng et al., 2018; McGrail et al., 2013). The data is collected from the Columbia Hills CAES

project from McGrail et al. (2013). A further benefit is that the waste heat generated by the multi-stage compressors can be better recovered in the ORC. The multi-stage centrifugal compressors and turbines were simulated with *Compr* blocks based on isentropic efficiency. *Heater* blocks were used to simulate the intercoolers and aftercoolers, which were chosen based on the heat transfer between the process stream and the cooling utility. Excess air was introduced into the combustors to ensure complete combustion. The combustors were simulated using the *RGibbs* block, with natural gas as the fuel of choice. The recuperator was simulated with a *HeatX* block. A pressure regulating valve was simulated with *Valve* block. The cavern was simulated with *Tank* block and the required input was outlet pressure. The different critical components of the CAES system were simulated with different blocks in Aspen Plus® has been summarised in Table 3-1.

Table 3-1 The different CAES components were simulated in Aspen Plus®

Components	**Blocks**
Compressors/Turbines	*Compr*
Intercoolers/Aftercooler	*Heater*
Pressure regulating valve	*Value*
Recuperator	*HeatX*
Cavern	*Tank*
Combustors	*RGibbs*
Water pump	*Pump*

To simplify the D-CAES model simulation, the assumptions are listed as follows:

(1) The process is simulated under steady-state condition.
(2) The default air content is 78 vol% nitrogen, 21vol% oxygen, and 1vol% Ar.
(3) The isentropic efficiency of the multi-stage compressors is 75% (Ding et al., 2022).
(4) The pressure drops of all components are neglected.
(5) The isentropic efficiency of the turbines is 93% (Ding et al., 2022).
(6) The temperature of the fuel is 32 °C (Ding et al., 2022).
(7) The pressure into the combustion chamber is by default the same as the cavern outlet pressure (4.6 MPa).

(8) Pump mechanical efficiency of 80% and drive efficiency 97%.

The model physical property method was calculated using PENG-ROB (Standard Peng-Robinson cubic equation of state) method. PENG-ROB equation was developed by Peng and Robinson on 1976 (Meng et al., 2018; Liu et al., 2014) and it is implemented for the property calculation for the CAES model.

In this study, the ambient condition can be assumed as the 1.013 bar of pressure. The Huntorf CAES plant data was collected from Meng et al. (2019), Budt et al. (2016) to validate the models. Table 3-2 shows the operational parameters that were used in the CAES model as inputs. Table 3-3 shows the results of steady-state simulation against the Huntorf CAES plant. The results show that the amount of the relative error associated are 0.18% and 0.38%.

Table 3-2 The critical operational parameters of Huntorf plant

Process	**Parameters**	**Value**
Charging	Rated air mass flowrate	108 kg/s
Charging	Rated power of compressor (HPCs and LPC)	60 MW
Charging	Compressor stage	2
Charging	High pressure ratio	8
Charging	Low pressure ratio	6
Discharging	Rated power of turbine (HPT and LPT)	290 MW
Discharging	Rated air mass flowrate	417 kg/s
Discharging	Inlet pressure of HPT	4.2 MPa
Discharging	Inlet temperature of HPT	550°C
Discharging	Inlet pressure of LPT	1.13 MPa
Discharging	Inlet temperature of LPT	825°C

As the data from the Huntorf CAES plant is not sufficiently detailed, an additional model comparison with McGrail et al. (2013) was carried out. Based on the above assumptions, the simulation results were compared with the Columbia Hills CAES project from McGrail et al. (2013) to verify the model accuracy. Columbia Hills CAES plant is a planned project (but not commercially

deployed) and belongs to the D-CAES type. As shown in Table 3-4, all the relative errors are less than 1%.

Table 3-3 Model validation results comparison with Huntorf CAES plant

Quantity	Huntorf data	Simulation results	Relative errors (%)
Compressors consumption (MW)	60.00	60.11	0.18
Rated power of turbine (MW)	290.00	291.11	0.38

Table 3-4 Comparison between simulation results and data in Columbia Hills CAES plant (McGrail et al., 2013)

Parameters	Present work	Reference	Relative errors (%)
Inlet temperature of cavern (°C)	40.55	40.56	0.02
Inlet pressure of cavern (bar)	115.60	115.62	0.01
Outlet temperature of COM1 (°C)	676.02	676.67	0.09
Outlet pressure of COM1 (bar)	34.37	34.40	0.08
Outlet temperature of HPT (°C)	544.02	546.11	0.38
Outlet pressure of HPT (bar)	18.22	18.27	0.27
Outlet temperature of LPT (°C)	1330.65	1331.67	0.08
Outlet pressure of COM2 (bar)	17.90	17.93	0.17
Outlet temperature of LPT (°C)	604.55	601.72	0.47
Outlet temperature of REC (°C)	115.11	115.56	0.39
Outlet pressure of REC (bar)	1.03	1.03	0
Consumption power of LPC+(HPC1-HPC6) (kW)	229,160	228,670	0.21
Output power of HPT+LPT (kW)	205,789	205,392	0.19

3.3 Simulation and model validation of ORC

As shown in Figure 1-18, ORC consists of the turbine, condenser, pump and evaporator. The organic working fluid is R600a (Iso-Butane), which is a widely

used refrigerant. The *HeatX* block was used to simulate the evaporator and condenser. The *Compr* block was used to model the turbine, while the *Pump* block was used to simulate the fluid pump. The different critical components of the ORC were simulated with different blocks in Aspen Plus® has been summarised in Table 3-5.

Table 3-5 The different ORC components were simulated in Aspen Plus®

Components	Blocks
Evaporator	*HeatX*
Condenser	*HeatX*
Pump	*Pump*
Turbine	*Compr*

The following assumptions were made for the simulation:

(1) The ORC operates at steady-state condition.
(2) The pressure drops of all the components are neglected.
(3) The outlet stream of condenser is assumed to be saturated liquid condition (Meng et al., 2018).
(4) The isentropic efficiencies of the ORC turbine and pump are all assumed to be 85% and 92.5% (Ding et al., 2022).

The experimental data for ORC model validation was chosen from Kanoglu and Bolatturk (2008). Table 3-6 shows the input process conditions of ORC.

Table 3-6 Input process conditions and parameters of ORC (Kanoglu and Bolatturk, 2008)

Parameters	Value
Hot stream inlet flowrate (kg/s)	555.9
Hot stream inlet temperature (°C)	158
R600A flowrate (kg/s)	305.6
Cooling water inlet temperature (°C)	3
Cooling water inlet mass flowrate (kg/s)	1695.6
Turbine inlet/outlet pressure (bar)	32.5/4.1
Turbine isentropic efficiency	85%
Pump efficiency	92.5%

As shown in Table 3-7, the simulation results were compared with plant data to check the accuracy of the model in Aspen Plus® V12. All relative errors were less than 3% and the results of the simulation matched the commercial plant data.

Table 3-7 Simulation results compared with the plant data for geothermal power plant in Reno (Kanoglu and Bolatturk 2008)

Parameters	Reference plant data	Present work	Relative errors (%)
Heat resource of EVAP outlet temperature (°C)	128.00	128.70	0.54
Output power of OT (MW)	16.40	16.00	2.43
Cooling water outlet temperature (°C)	11.70	11.40	2.56
EVAP heat transfer rate (MW)	160.93	156.75	2.60
OT heat transfer rate (MW)	21.74	21.37	1.70
COND heat transfer rate (MW)	141.27	137.48	2.68

3.4 Simulation and model validation of single-effect ARS using $LiBr/H_2O$ and NH_3/H_2O

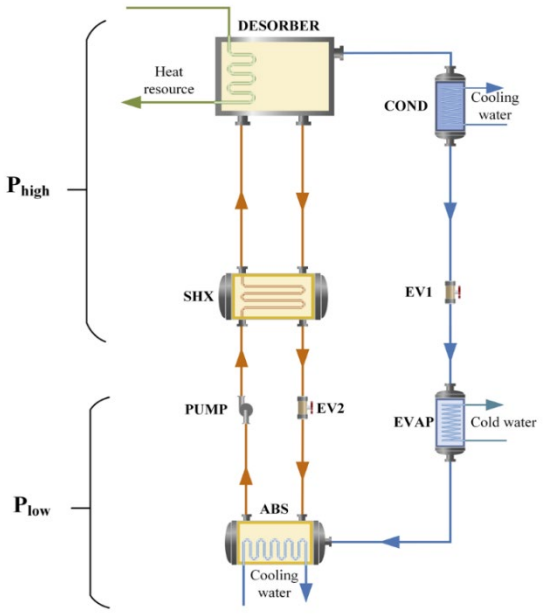

Figure 3-2 A simulation flowsheet of the single-effect ARS using $LiBr/H_2O$ and NH_3/H_2O

The simulation flowsheet of the single-effect ARS using LiBr/H_2O and NH_3/H_2O is shown in Figure 3-2. This section focuses on simulating single-effect ARS, then using LiBr/H_2O and NH_3/H_2O as working media. Considering the operating conditions and working fluids, the physical properties were computed using the ElecNRTL method. This is due to that the operating conditions and fluids being simulated with this method are designed for electrolytes (Somers et al., 2011).

The components of a single-effect LiBr/H_2O absorption system are simulated with different blocks in Aspen Plus®, as summarised in Table 3-8.

Table 3-8 Different components in ARS simulated in Aspen Plus®

Components	**Blocks**
Desorber	*Flash2, HeatX*
Solution heat exchanger (SHX)	*HeatX*
Condenser (COND)	*HeatX*
Evaporator (EVAP)	*HeatX*
Absorber (ABS)	*HeatX*
Pump	*Pump*
Throttling valve (EV)	*Value2*

The steady-state simulation assumptions for the single-effect LiBr/H_2O absorption system are given below:

(1) The desorber pressure is the same as the condenser, and the pressure of the absorber is the same as the evaporator.
(2) The thick solution of LiBr at the outlet of the desorber and the diluted solution of LiBr at the outlet of the absorber are both saturated solutions.
(3) The pressure drops and heating loss of the piping and components are not considered.
(4) The amount of heat diffusion in the flow direction is ignored.

In Table 3-9, a comprehensive comparison is provided between the simulation results of the single-effect LiBr/H_2O ARS system presented in this study and the simulation results reported by Somers et al. (2011). The relative errors were calculated. It can be observed that all of them were less than 1%, indicating that the simulation results obtained in this study were highly accurate and reliable.

Table 3-9 Simulation results of single-effect ARS using LiBr/H_2O compared with literature data from Somers et al. (2011)

Parameters	Reference plant data	Present work	Relative errors (%)
P low (kPa)	0.672	0.671	0.15
P high (kPa)	7.461	7.462	0.01
DESORBER heat transfer rate (kW)	14.592	14.586	0.04
ABS heat transfer rate (kW)	13.923	13.919	0.11
COND heat transfer rate (kW)	11.432	11.401	0.27
EVAP heat transfer rate (kW)	10.772	10.741	0.29
Concentration of dilute solution (%)	57.400	57.100	0.53
Concentration of thick solution (%)	62.570	62.480	0.14
COP	0.738	0.734	0.55

In Table 3-10, a comprehensive comparison is provided between the simulation results of the single-effect NH_3/H_2O ARS system presented in this study and the simulation results reported by Herold et al. (2016). All the relative errors were less than 1%.

Table 3-10 Simulation results of single-effect ARS using NH_3/H_2O compared with literature data from Herold et al. (2016)

Parameters	Reference plant data	Present work	Relative errors (%)
P low (kPa)	286.40	286.00	0.14
P high (kPa)	1556.00	1557.10	0.07
DESORBER heat transfer rate (kW)	327.50	326.80	0.21
ABS heat transfer rate (kW)	273.90	274.60	0.26
COND heat transfer rate (kW)	159.20	160.50	0.81
EVAP heat transfer rate (kW)	146.90	146.50	0.27
Concentration of dilute solution (%)	29.62	29.57	0.17
Concentration of thick solution (%)	39.62	39.55	0.18
COP	0.447	0.445	0.45

3.5 Simulation and model validation of double effect ARS using LiBr/H_2O and NH_3/H_2O

The selected double-effect ARS is shown in Figure 3-3. This section focuses on simulating double-effect ARS, then using LiBr/H_2O and NH_3/H_2O as working media. Unit operations that do not have exact modelling block in Aspen Plus require multiple blocks to model, as discussed in section 3.4.

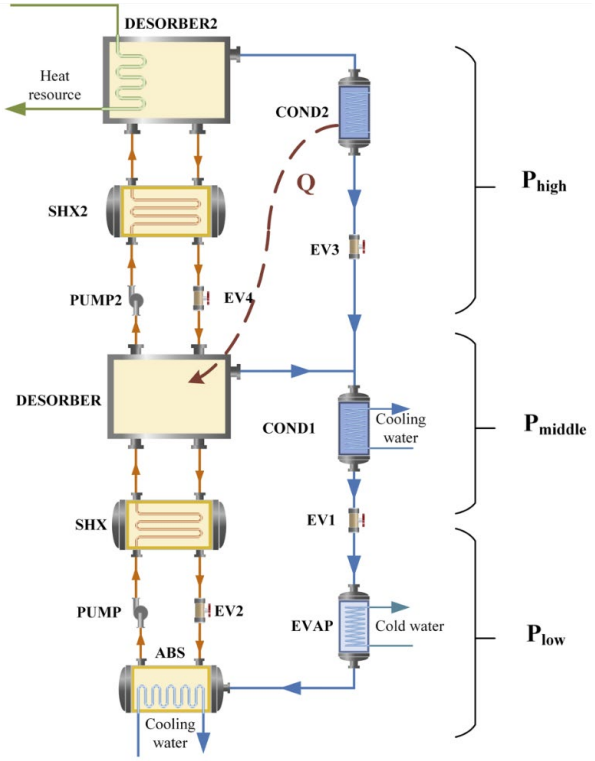

Figure 3-3 A simulation flowsheet of the double effect ARS using LiBr/H_2O and NH_3/H_2O

Table 3-11 shows the simulation results of double-effect LiBr/H_2O ARS compared with Somers et al. (2011). The results show that relative errors all below 1%.

Table 3-12 presents the simulation results of the double-effect NH_3/H_2O ARS model and compares them with the findings from Herold et al. (2016). Although slightly higher differences were observed in the double-effect ARS model compared to the single-effect ARS model, all relative errors remained below 1%, indicating that the simulation results were consistent with the reference plant data.

Table 3-11 Simulation results of double-effect ARS using $LiBr/H_2O$ compared with literature data from Somers et al. (2011)

Parameters	Reference plant data	Present work	Relative errors (%)
P low (kPa)	0.881	0.879	0.23
P middle (kPa)	4.178	4.172	0.14
P high (kPa)	64.370	64.310	0.09
DESORBER2 heat transfer rate (kW)	255.430	254.385	0.41
ABS heat transfer rate (kW)	421.250	420.186	0.25
COND2 and DESORBER heat transfer rate (kW)	189.860	188.784	0.57
COND1 heat transfer rate (kW)	188.580	189.212	0.33
EVAP heat transfer rate (kW)	354.370	352.112	0.64
COP	1.387	1.410	0.57

Table 3-12 Simulation results of double-effect ARS using NH_3/H_2O compared with literature data from Herold et al. (2016)

Parameters	Reference plant data	Present work	Relative errors (%)
P low (kPa)	494.80	494.30	0.10
P middle (kPa)	1344.10	1345.00	0.07
P high (kPa)	3365.40	3366.10	0.02
DESORBER2 heat transfer rate (kW)	206.00	205.80	0.09
ABS heat transfer rate (kW)	347.70	346.60	0.32
COND2 and DESORBER heat transfer rate (kW)	148.90	147.90	0.68
COND1 heat transfer rate (kW)	156.70	155.90	0.51
EVAP heat transfer rate (kW)	182.60	181.90	0.39
COP	1.165	1.171	0.51

3.6 Conclusion

This chapter presents the methodology for the development of the steady-state models and model validations carried out. The CCHP includes three parts, CAES, ORC and different types of ARS.

(1) The CAES model was developed in Aspen Plus® V12, then using Huntorf CAES plant data to perform model validation. As the data from the Huntorf CAES plant is not sufficiently detailed, an additional model comparison with Columbia Hills CAES project was also carried out.
(2) The ORC model was developed in Aspen Plus® V12, then compared with the geothermal power plant in Reno data.
(3) Models for different types of ARS were also developed in Aspen Plus® V12. The simulation results of single-effect ARS using $LiBr/H_2O$ and double-effect ARS with $LiBr/H_2O$ were all compared with Somers et al. (2011). The single-effect ARS using NH_3/H_2O and double-effect ARS using NH_3/H_2O were all compared with Herold et al. (2016).

All the relative errors were less than 5% and the simulation results matched the ARS commercial plant data. It should be mentioned that the cavern model wasn't developed because the steady-state model can't describe the behaviour of cavern.

4. Thermodynamic analysis of CCHP

4.1 Overview

In this chapter, simulation, energy and exergy analysis of CCHP system including CAES, ORC and single-effect ARS using LiBr/H_2O were carried out [1]. The ORC operates during both charging and discharging processes. In this study, the ARS is designed only operated during the discharging process. The performance of CCHP system was evaluated. In section 4.2, the detailed process description of the CCHP system is given. In section 4.3, the exergy analysis was carried out. In section 4.4, process analysis of CCHP system's performance was evaluated. Several key parameters were chosen to be analysed such as inlet mass flowrate of pump in ARS, inlet temperature of combustion chamber 1, different working fluids for ORC, ORC turbine inlet pressure, inter-cooler temperatures and compressor inlet temperature. Conclusion of this chapter is drawn in Section 4.5.

4.2 Brief description of CCHP

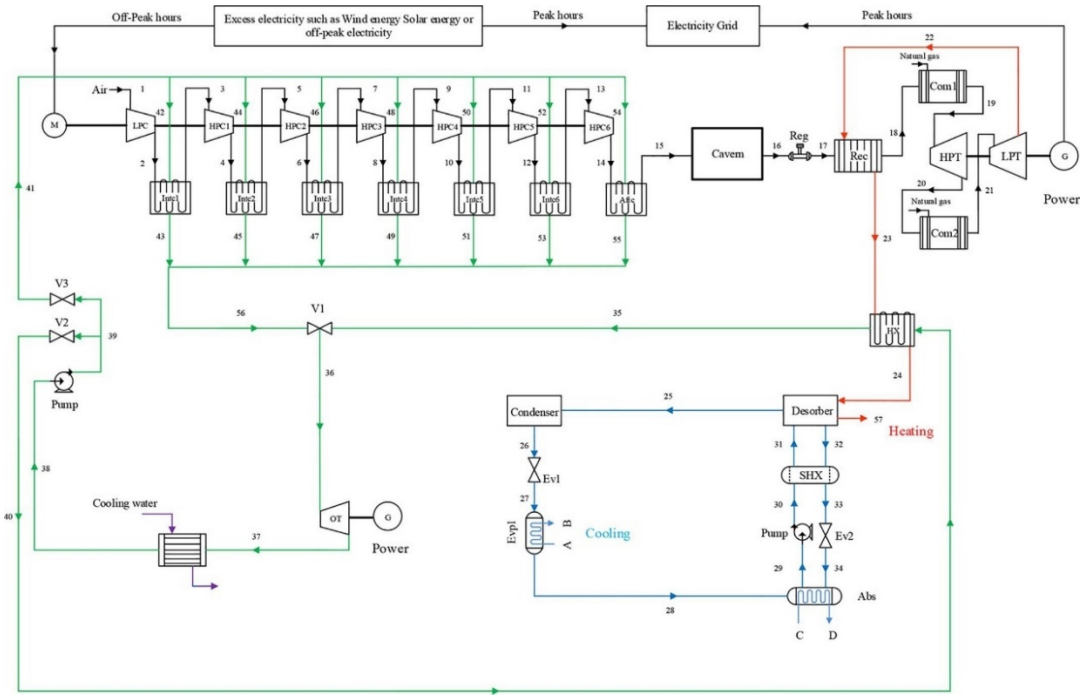

Figure 4-1 Schematic diagram of CCHP system

[1] Most of contents in Chapter 4 was published in Ding et al. (2022), Simulation, energy and exergy analysis of compressed air energy storage integrated with organic Rankine cycle and single-effect absorption refrigeration for trigeneration application. *Fuel*, *317*, 123291.

Figure 4-1 shows the proposed CCHP system, which comprises a CAES system, an ORC and a single-effect ARS using LiBr/H_2O. The CCHP system is further divided into two subsections (i.e. the charging and discharging processes).

During the charging process, the multi-stage compressors compress air to high pressure and store it in the cavern, converting electrical energy into the internal energy of the air for storage during periods of low power demand. Multi-stage compressors offer greater efficiency, less moisture accumulation and a smaller footprint (Meng et al., 2018; McNevin and Harrison, 2017). However, multi-stage compressors introduce much low-grade waste heat during operation. Using inter-coolers and after-cooler, an ORC recovers low-grade waste heat from multi-stage compressors to increase RTE (Meng et al., 2018; Quoilin et al., 2013).

During the discharging process, the high-pressure air is released from the cavern and heated up in the recuperator by recovering the waste heat from the exhaust of the low-pressure turbine. The fuel (natural gas) is then burnt in the combustion chamber by mixing with the preheated air. The high-temperature and high-pressure gas enters the turbine where it is expanded to generate electricity during peak electricity consumption (Budt et al., 2016; Zhou et al., 2019). But the stream leaving the low-pressure turbine still has some waste heat, one part is used to drive the ORC turbine and other is used to drive the ARS. The recovered waste heat can further improve RTE of CCHP system and generate cooling capacity.

The single-effect ARS can be driven by low-grade waste heat from low-pressure turbine. The advantages of using a single-effect ARS integrated with ORC include high economic efficiency and environmentally friendly (Misra et al., 2003; Gomri, 2009). The single-effect ARS consists of the desorber, condenser, evaporator, absorber, and solution heat exchanger. In this study, LiBr/H_2O is used as working medium of ARS. This is due to the refrigeration system's high economic efficiency, safety reliability, non-toxicity and odour lessness of LiBr solution (Chen et al., 2017; Misra et al., 2003). The operational mechanism of a single-effect ARS can be divided into two key processes. Firstly,

a portion of the solution is segregated as water vapour, which serves as the refrigerant, whereas the remaining portion is transformed into a concentrated LiBr solution. The separated water vapour is condensed into water by a condenser and then evaporated to absorb heat and produce cooling before entering the absorber and mixing with the concentrated LiBr solution to form a dilute LiBr solution. In contrast, the concentrated LiBr solution within the desorber undergoes heat exchange with the dilute LiBr solution before being fed into the absorber via a throttle valve. Subsequently, the concentrated solution mixes with the refrigerant vapour, leading to its dilution into a dilute solution within the absorber. The solution passes through the solution pump and the solution heat exchanger before entering the generator. A cooling capacity is generated through the working procedure.

The proposed CCHP system is comprised of three parts, namely CAES, ORC and single-effect ARS using Libr/H_2O. To study the process analysis of CCHP system, all models have been developed and integrated successfully within a single flowsheet in Aspen Plus® V12. The assumed input parameters design condition of CCHP system (as shown in Table 4-1).

Table 4-1 Design conditions of CCHP system (charging and discharging process)

Charging Process		
Parameter	Value	Unit
Ambient temperature	25	°C
Ambient pressure	1.013	bar
Pressure ratio of compressor	1.96177	-
Mass flowrate of compressor	353	kg/s
Compressor isentropic efficiency	75	%
Charging time	3	hour

Aftercooler exit/Cavern inlet pressure	115.65	bar
Throttle outlet/Cavern outlet pressure	35.78	bar
Throttle outlet	40.56	°C
ORC turbine inlet pressure	4	bar
ORC condenser pressure	4	bar
ORC turbine isentropic efficiency	85	%
ORC pump isentropic efficiency	92.5	%
Discharging Process		
Discharging time	6	hour
Inlet pressure of high-pressure turbine	34.40	bar
CAES Turbine isentropic efficiency	93	%
Inlet pressure of low-pressure turbine	17.93	bar
Fuel inlet pressure of combustor 1	44.82	bar
Fuel inlet pressure of combustor 2	24.13	bar
Fuel inlet temperature of combustor 1	32.22	°C
Fuel inlet temperature of combustor 2	32.22	°C
Heat duty of recuperator	105.51	kW
ORC turbine inlet pressure	19.85	bar
ORC condenser pressure	4	bar
ORC turbine isentropic efficiency	80	%

ORC pump isentropic efficiency	80	%
Outlet temperature of desorber	40.2	°C
ARS pump isentropic efficiency	85	%
Outlet temperature of SHX	53.5	°C
Outlet pressure of SHX	0.07461	bar

4.3 Exergy analysis

Exergy analysis is a thermodynamic analysis technique that have resulted from the second law of thermodynamic (Mohammadi et al., 2017; Sadreddini et al., 2018). The equations used to calculate the exergy destruction and exergy efficiency of each component are derived from Eqs. (2-4) - (2-12). According to the exergy analysis of the proposed CCHP system under design conditions, Figure 4-2 presents the results of the exergy destruction. The different colours mean different components. The highest exergy destruction (160,635 kW) was observed in the combustion chamber, which is attributed to the irreversibility of the combustion process leading to the highest level of exergy destruction in the CAES plant. The sum of Com1 and Com2 exergy destruction account for 33.64%. This is because the combustion process occurs in the combustor, and the combustor's irreversibility results. Furthermore, to reduce exergy destruction, the use of fuels (such as natural gas) with a simple molecular structure containing oxygen molecules is recommended (Sadreddini et al., 2018).

In addition, the incorporation of a recuperator for preheating the air and fuel before their introduction into the combustion chamber is an effective way to prevent combustion chamber destruction. The cavern component exhibited the second-highest exergy destruction at 83,716 kW, followed by the value and recuperator at third and fourth positions, respectively, due to the substantial temperature difference between the hot and cold streams entering these components.

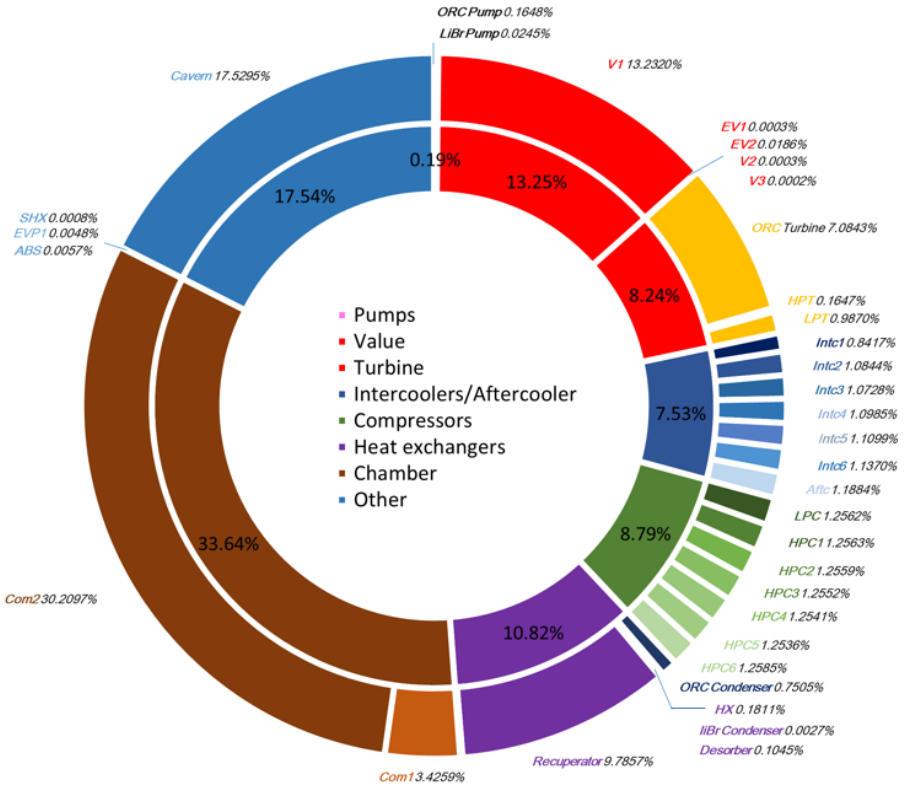

Figure 4-2 Exergy destruction of different components of the CCHP system

4.4 Process analysis

4.4.1 Effect of inlet temperature of compressor on CCHP performance

Figure 4-3 shows how the performance of the CCHP system is affected when the compressor inlet temperature changes. When it comes to multi-stage compressors, a higher inlet temperature of the compressor correlates to a higher exergy destruction. Because the compressor requires less power input to function properly when the air temperature entering the compressor is higher, the total compressor output will decrease when this occurs. This will result in an increase in the RTE of the CCHP system. The results show that the higher the inlet temperature of the compressor, the greater the amount of exergy that is lost.

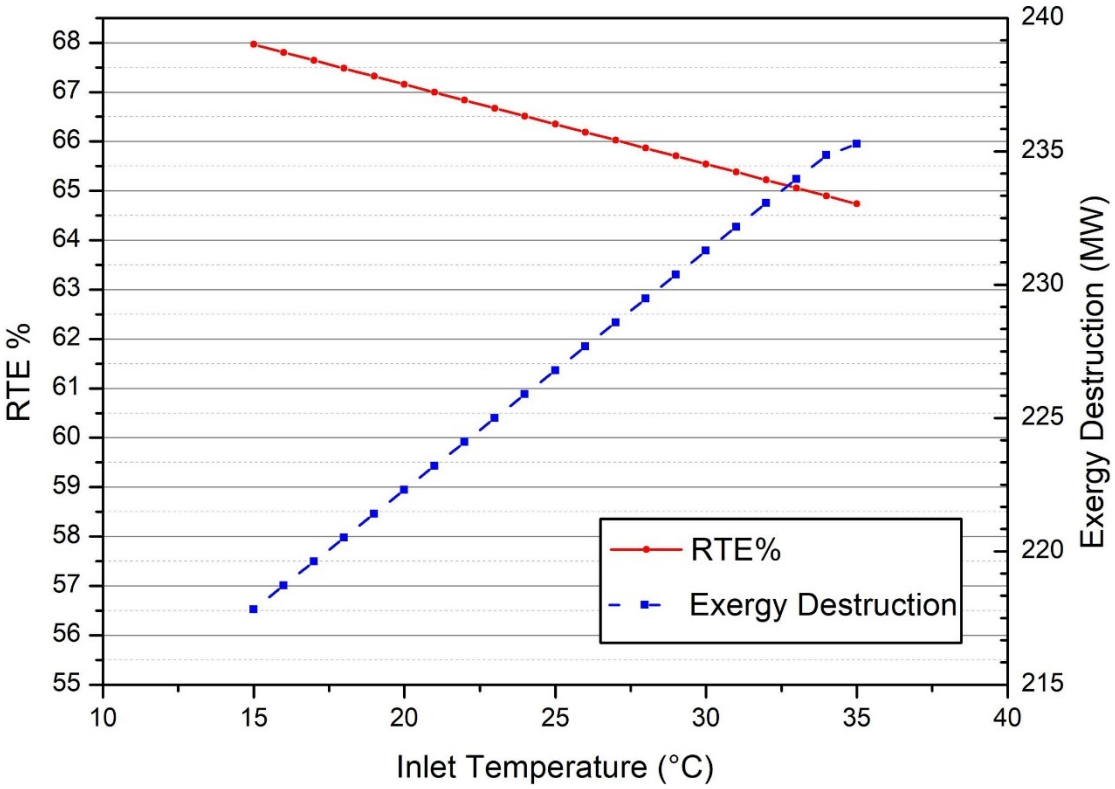

Figure 4-3 The impact of different compressor inlet temperatures on the performance of the proposed CCHP system

4.4.2 Effect of inlet pressure of ORC turbine on CCHP performance

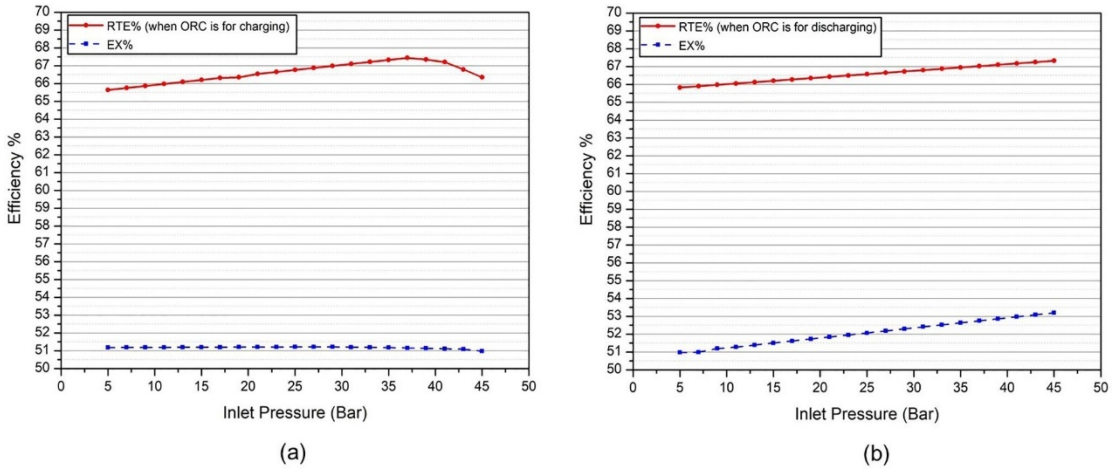

Figure 4-4 The impact of different inlet pressure of the ORC turbines on the performance of the proposed CCHP system (a) for charging process and (b) discharging process

Figure 4-4 presents the impact of the ORC turbine inlet pressure on total exergy destruction and the RTE during the whole process. The ORC power output increases as the inlet pressure increases. The findings indicate that there is an

optimal inlet pressure for the ORC turbine, which maximises the power generation, cooling and heating capacity. The results demonstrate that the optimal operating point of the inlet pressure during the charging process is approximately 35 bar. During the discharging process (as shown in Figure 4-4 (b)), the RTE and exergy efficiency of the system continue to increase with the increase in inlet pressure. The proposed CCHP system could achieve the highest RTE (66.35%) when the inlet pressure of the ORC turbine is at 35 bar.

4.4.3 Effect of different working fluids for ORC on CCHP performance

The selection of organic working fluids for the ORC to achieve the maximum utilisation of waste heat is important. Therefore, the performance of different working fluids operating is analysed. Figure 4-5 shows impact of different working fluids of the ORC on the performance of the proposed CCHP system. Under design condition, the charging time is 3 hours and discharging time is 6 hours.

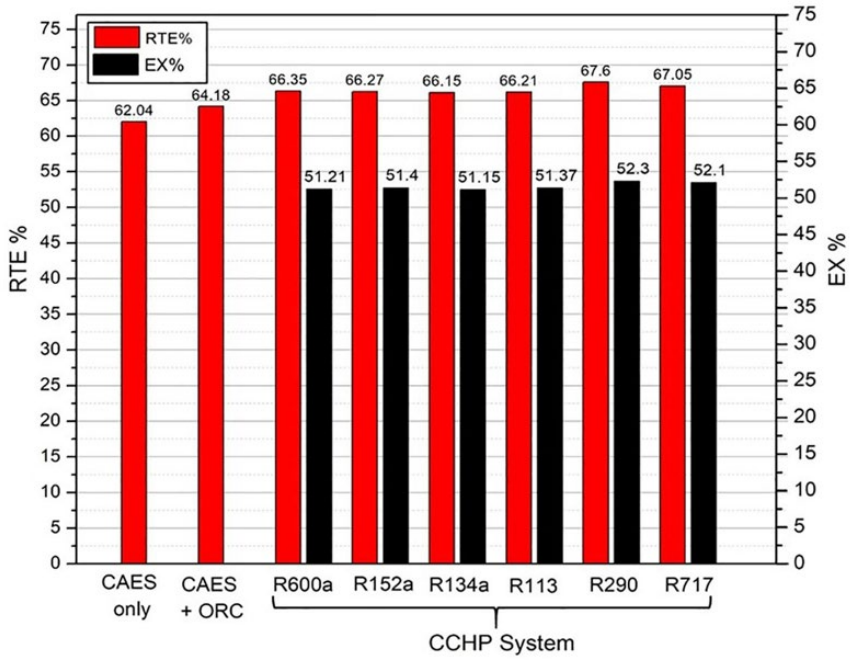

Figure 4-5 The impact of different working fluids of the ORC on the performance of the CCHP system

The study revealed that the RTE of the CAES system alone is 62.04%, whereas the RTE of the combined CAES system and ORC is 64.18%. To explain this, the inlet temperature of compressors and the combustion efficiency are different in two studies. The RTE of the CCHP system can achieve 66.35%.

The results show that the RTE of the CCHP system with R290 can reach up to 67.6%, an increase of 5.56% compared with CAES-only.

4.4.4 Effect of combustion chamber 1 inlet temperature on CCHP performance

Figure 4-6 illustrates the impact of the inlet temperature of the combustion chamber 1 on the overall performance of the proposed CCHP system. The inlet temperature of the combustion chamber is studied in the range from 490°C to 640°C.

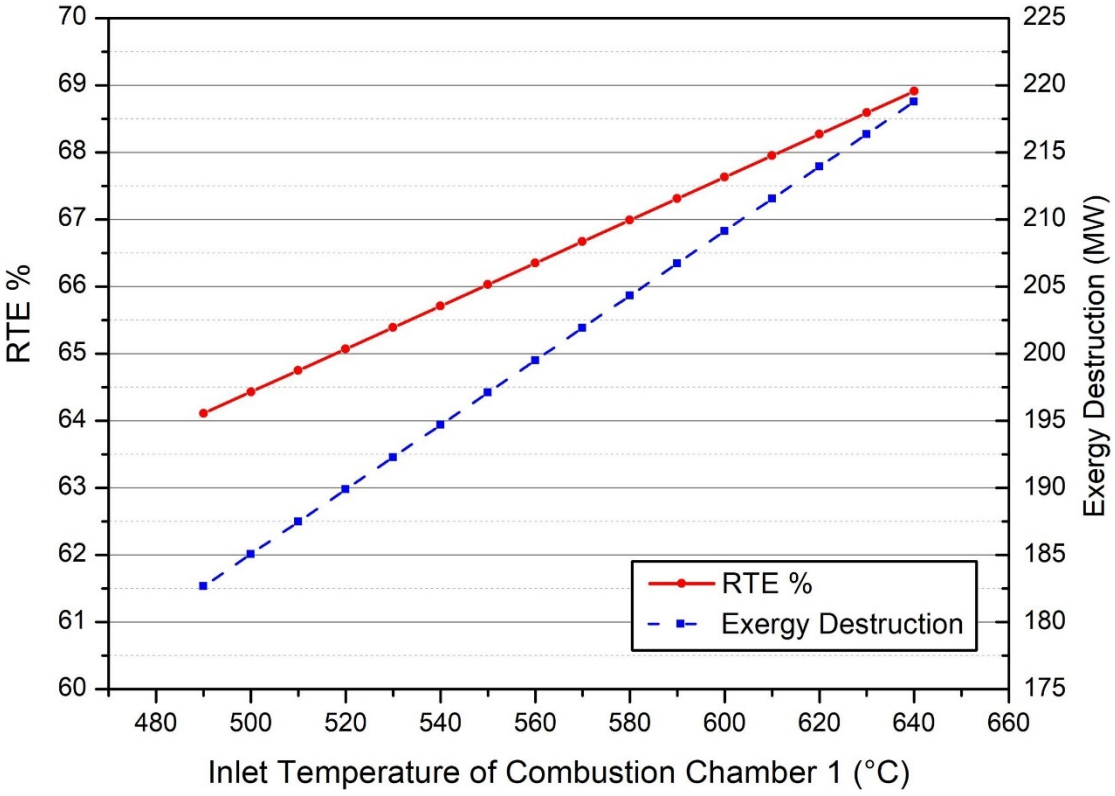

Figure 4-6 The impact of different inlet temperatures of combustion chamber 1 on the performance of the proposed CCHP system

As evidenced by the results, there was an increase in exergy destruction corresponding to the rising inlet temperature of the combustion chamber 1. The findings demonstrate that a rise in the inlet temperature translates into a higher output of the turbine. When the inlet temperature of the combustion chamber reaches 640°C, the RTE can achieve 69%. Moreover, this results in an increase in the outlet temperature of the turbine, leading to a higher power output generated by the ORC turbine. Additionally, due to the low-grade waste heat

produced from the flue gas, the cooling capacity generated by the single-effect ARS also increases.

4.4.5 Effect of inlet mass flowrate of pump in ARS on CCHP performance

Figure 4-7 shows the effect of the inlet mass flowrate of pump in ARS on the performance of the proposed CCHP system. The inlet mass flowrate of pump in ARS is studied in the range from 0.4 kg/s to 2.4 kg/s. The downstream placement of the single-effect ARS ensures that alterations in its parameters do not impact the ORC. Owing to the use of flue gas as the heating source, the cooling capacity of the single-effect ARS is limited to 245.45 kW. The results indicate that the COP efficiency attains its maximum value of 74% when the mass flowrate of the pump is 1 kg/s.

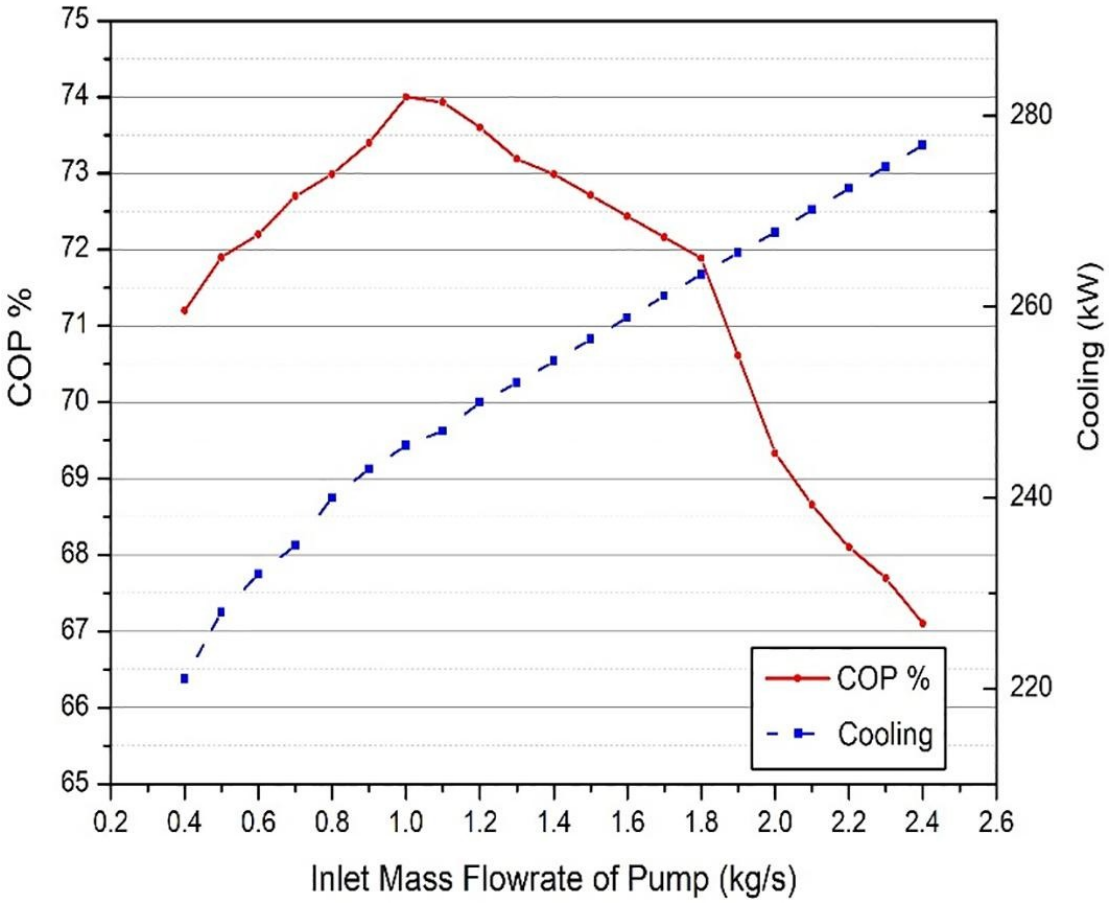

Figure 4-7 The impact of varying inlet mass flowrate of pump in ARS on the performance of the proposed CCHP system

4.5 Conclusion

In this chapter, a newly proposed CCHP system including CAES, ORC and single-effect ARS using LiBr/H_2O was proposed. The aim of research in this chapter is to improve the RTE of CCHP system. The energy and exergy analysis of a CCHP system was carried out. The key findings can be summarised as follows:

(1) The proposed CCHP system exhibits a remarkable improvement in its RTE when compared to the CAES only. The RTE of the CCHP system with R290 can reach up to 67.6%, an increase of 5.56% compared with CAES-only. The results indicated that the RTE and exergy efficiency achieve impressive values of 67.6% and 51.21%, respectively, under design conditions.

(2) The CCHP system experiences a total exergy destruction of 478 MW, in which the combustion chamber is responsible for more than half of it.

(3) R290 (Propane) as the ORC working fluid is the most suitable working fluid with the best performance.

(4) Of all the parameters considered, the inlet temperature of the compressor, the inlet temperature of the combustion chamber 1 and the inlet pressure of the ORC turbine are the most critical parameters.

5. Multi-objective optimisation and analysis of CCHP

5.1 Overview

The proposed CCHP system has not yet been commercially deployed. As such, an economic evaluation and multi-objective optimisation to identify the optimal operating conditions that maximize RTE and reduce the cost will be conducted in Chapter 5 [2]. These analyses are critical in determining the feasibility and potential of the CCHP system (includes CAES, ORC and single-effect ARS using $LiBr/H_2O$) for real-world applications and will help inform future development and implementation efforts.

Note, the ORC is designed to operate during both charging and discharging processes. The ARS only operates during the discharging process. Section 5.2 gives the performance analysis methodologies. In section 5.3, optimisation formulation of CCHP is proposed. Section 5.4 demonstrates the multi-objective optimisation results and analyse the impact of different working fluids on the CCHP system, as well as the results of energy, exergy, and economic analysis. Finally, the conclusions are presented in Section 5.5.

5.2 Performance analysis methodologies

The performance of the proposed system is analysed in three ways: 1) energy analysis, 2) exergy analysis, 3) economic analysis. For the energy analysis, the energy efficiency, COP and RTE are analysed by calculating the heat flow and work to evaluate each distinct subsystem and the suggested system performance. Exergy analysis is performed by calculating the exergy destruction of each component, subsystem and the suggested system. For the economic analysis, the total investment cost per output power (ICPP) is employed to evaluate the application potential.

The difference between section 4.3 and section 5.2.2 should be explained. The section 5.2.2 has more details of exergy analysis, this exergy analysis is

[2] Most of contents in Chapter 5 was published in Liu and **Ding** (2022), A trigeneration application based on compressed air energy storage integrated with organic Rankine cycle and absorption refrigeration: Multi-objective optimisation and energy, exergy and economic analysis. *Journal of Energy Storage*, 55, 105803.

performed after multi-objective optimisation. Section 5.2.1 energy analysis is also performed after multi-objective optimisation.

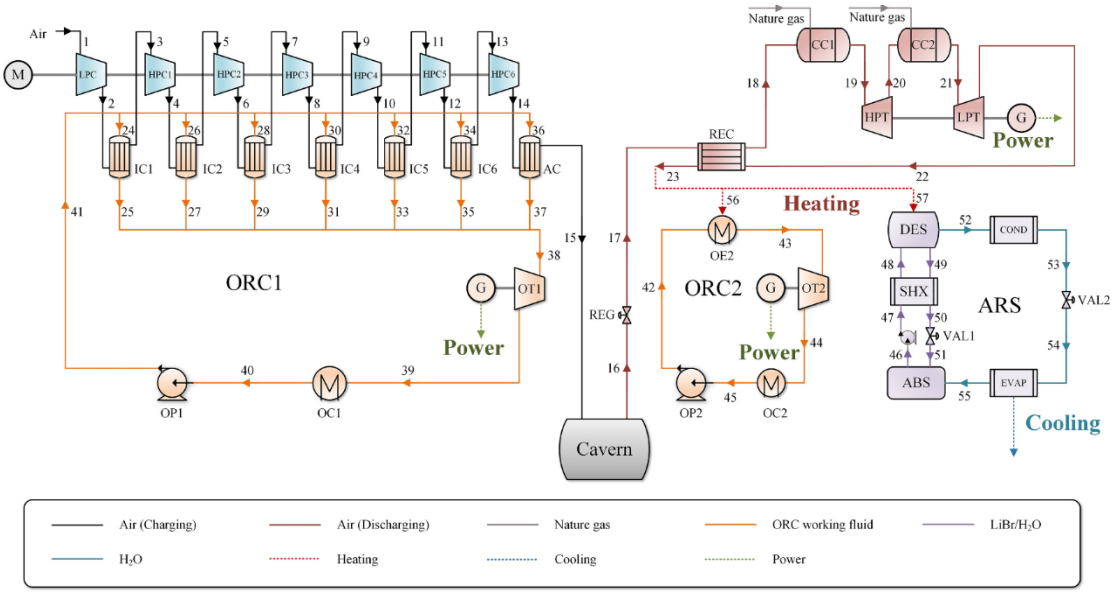

Figure 5-1 Process flow diagram of the CCHP system

The process flow diagram of the investigated CCHP system is illustrated in Figure 5-1. For better illustration, the system is described from the charging and discharging processes. ORC1 refers to ORC operating on charging process, and ORC2 refers to ORC operating on discharging process.

5.2.1 Energy analysis

To comprehensively evaluate the performance of the proposed system and its individual components, a detailed analysis of heat flow for each stream was conducted (Ghaebi et al., 2017). The energy balance for each component was derived by:

$$\sum \dot{m}_{in} - \sum \dot{m}_{out} = 0 \qquad (5-1)$$

$$\sum \dot{m}_{in} h_{in} + \sum \dot{Q}_{in} - \sum \dot{m}_{out} h_{out} - \sum \dot{Q}_{out} + \dot{W} = 0 \qquad (5-2)$$

The fundamental thermodynamic principles governing the proposed system were described using key parameters, including mass flowrate ($\dot{m}$), enthalpy (h), heat flow ($\dot{Q}$), and power ($\dot{W}$), where subscripts "in" and "out" are used to denote the inlet and outlet streams, respectively. Specifically, to increase ambient air pressure, a combination of one low-pressure compressor and six high-pressure compressors was employed, with the outlet temperature of these

compressors and required power calculated using established analytical techniques. These equations are as follows (Houssainy et al., 2018):

$$\dot{W}_{AC} = \dot{m}_a(h_{out} - h_{in}) \quad (5-3)$$

Notably, the subscripts AC and a are used to represent the air compressor and air, respectively. One important consideration in the design of the proposed system was the ability to recover the heat generated during compressor operation. Specifically, the heat generated in the compressors could be effectively recovered by using inter-coolers (ICs) and after-coolers (ACs), which function similarly to the evaporator in a refrigeration cycle. The energy balance of these components can be accurately characterized through heat exchanger calculations, allowing for a comprehensive understanding of their contribution to overall system performance. These equations are as follows:

$$\dot{Q}_{HE} = \dot{m}_{cold}(h_{out} - h_{in}) = \dot{m}_{hot}(h_{in} - h_{out}) \quad (5-4)$$

$$\dot{m}_{wf1} = \sum_{i=1}^{7} \dot{m}_{wf,i} \quad (5-5)$$

Where the subscript hot, $cold$ and wf denote the hot stream, cold stream and the working fluid, respectively. Of particular importance is the volume of the cavern, which is a critical parameter in determining overall system performance. The volume of the cavern can be accurately calculated as a function of inlet and outlet air densities and mass flowrates, using established analytical methods. Where V, t and ρ represent volume of cavern, charging time and density, respectively. The equation is expressed as (Roushenas et al., 2020; Razmi et al., 2021):

$$V_{CAES} = \frac{3600\dot{m}_a t_{charging}}{\rho_{in} - \rho_{out}} \quad (5-6)$$

A pressure regulating valve is employed to precisely control the pressure of the released air, ensuring stable and reliable operation. Importantly, this process is treated as an enthalpy invariant process, consistent with established thermodynamic principles (Razmi et al., 2021):

$$h_{in} = h_{out} \quad (5-7)$$

The energy balance of the combustion chamber can be expressed using established thermodynamic principles, and the power generated by the turbine can be calculated accordingly. These equations can be expressed as follows (Alirahmi, et al., 2021):

$$\dot{m}_a h_{in} + \dot{m}_{f1} LHV = \dot{m}_g h_{out} + (1 - \eta_{CC}) \dot{m}_{f1} LHV \qquad (5-8)$$

$$\dot{W}_{Tur} = \dot{m}_{in}(h_{in} - h_{out}) \qquad (5-9)$$

The temperature and lower heating value of the fuel are critical parameters that must be carefully considered. Furthermore, the subscripts Tur, CC and g denote the turbines, combustion chambers and gas, respectively, underscoring the complex interplay between these components and their role in the overall system performance. The required power was expressed:

$$\dot{W}_{Pump} = \dot{m}_{in}(h_{out} - h_{in}) \qquad (5-10)$$

The energy balance equations for each of the individual components are important. These equations are summarized in Table 5-1.

Table 5-1 Energy balance equations for the CCHP system

Components	Energy rate balance equation
CAES charging process	
LPC	$\dot{W}_{LPC} = \dot{m}_a(h_2 - h_1)$
HPC1	$\dot{W}_{HPC1} = \dot{m}_a(h_4 - h_3)$
HPC2	$\dot{W}_{HPC2} = \dot{m}_a(h_6 - h_5)$
HPC3	$\dot{W}_{HPC3} = \dot{m}_a(h_8 - h_7)$
HPC4	$\dot{W}_{HPC4} = \dot{m}_a(h_{10} - h_9)$
HPC5	$\dot{W}_{HPC5} = \dot{m}_a(h_{12} - h_{11})$
HPC6	$\dot{W}_{HPC6} = \dot{m}_a(h_{14} - h_{13})$
IC1	$\dot{Q}_{IC1} = \dot{m}_{wf,1}(h_{25} - h_{24}) = \dot{m}_a(h_2 - h_3)$
IC2	$\dot{Q}_{IC2} = \dot{m}_{wf,i}(h_{27} - h_{26}) = \dot{m}_a(h_4 - h_5)$
IC3	$\dot{Q}_{IC3} = \dot{m}_{wf,i}(h_{29} - h_{28}) = \dot{m}_a(h_6 - h_7)$
IC4	$\dot{Q}_{IC4} = \dot{m}_{wf,i}(h_{31} - h_{30}) = \dot{m}_a(h_8 - h_9)$
IC5	$\dot{Q}_{IC5} = \dot{m}_{wf,5}(h_{33} - h_{32}) = \dot{m}_a(h_{10} - h_{11})$

IC6	$\dot{Q}_{IC6} = \dot{m}_{wf,6}(h_{35} - h_{34}) = \dot{m}_a(h_{12} - h_{13})$
AC	$\dot{Q}_{AC} = \dot{m}_{wf,7}(h_{37} - h_{36}) = \dot{m}_a(h_{14} - h_{15})$
Cavern	$V_{CAES} = \frac{3600\dot{m}_a t_{charging}}{\rho_{15} - \rho_{16}}$
CAES discharging process	
REG	$h_{16} = h_{17}$
REC	$\dot{Q}_{REC} = \dot{m}_{a,dis}(h_{18} - h_{17}) = \dot{m}_{a,dis}(h_{22} - h_{33})$
CC1	$\dot{m}_a h_{18} + \dot{m}_{f1} LHV = \dot{m}_g h_{19} + (1 - \eta_{CC})\dot{m}_{f1} LHV$
HPT	$\dot{W}_{HPT} = \dot{m}_{a,dis}(h_{19} - h_{20})$
CC2	$\dot{m}_a C_{Pa} T_{20} + \dot{m}_{f2} LHV = \dot{m}_g C_{Pg} T_{21} + (1 - \eta_{CC})\dot{m}_{f2} LHV$
LPT	$\dot{W}_{LPT} = \dot{m}_{a,dis}(h_{21} - h_{22})$
ORC	
OT1	$\dot{W}_{OT1} = \dot{m}_{wf,1}(h_{38} - h_{39})$
OC1	$\dot{Q}_{OC1} = \dot{m}_{wf,1}(h_{39} - h_{40})$
OP1	$\dot{W}_{OP1} = \dot{m}_{wf,1}(h_{41} - h_{40})$
OT2	$\dot{W}_{OT2} = \dot{m}_{wf,2}(h_{43} - h_{44})$
OC2	$\dot{Q}_{OC2} = \dot{m}_{wf,2}(h_{44} - h_{45})$
OP2	$\dot{W}_{OP2} = \dot{m}_{wf,2}(h_{42} - h_{45})$
OE2	$\dot{Q}_{OE2} = \dot{m}_{wf,2}(h_{43} - h_{43})$
ARS	
DES	$\dot{Q}_{DES} = \dot{m}_{ARS,48} h_{48} - \dot{m}_{ARS,49} h_{49} - \dot{m}_{ARS,52} h_{52}$
COND	$\dot{Q}_{COND} = \dot{m}_{ARS,52}(h_{52} - h_{53})$
EVAP	$\dot{Q}_{EVAP} = \dot{m}_{ARS,54}(h_{55} - h_{54}) = \dot{Q}_{cooling}$
ABS	$\dot{Q}_{ABS} = \dot{m}_{ARS,55} h_{55} + \dot{m}_{ARS,51} h_{51} - \dot{m}_{ARS,46} h_{46}$
SHX	$\dot{Q}_{SHX} = \dot{m}_{ARS,48}(h_{48} - h_{47}) = \dot{m}_{ARS,49}(h_{49} - h_{50})$
PUMP	$\dot{W}_{PUMP} = \dot{m}_{ARS,47}(h_{47} - h_{46})$
VAL1	$h_{50} = h_{51}$
VAL2	$h_{53} = h_{54}$

It provides a detailed overview of each component's key inputs and outputs and serves as a valuable tool for analysing and optimising the overall system performance.

The energy efficiency by the first law of thermodynamics was derived as the ratio of the output energy to the input energy. Where subscript en is energy, η_{en} denote the energy efficiency. There it can be expressed as (Lee and You, 2019):

$$\eta_{en} = \frac{\sum(\dot{Q}_{out}+\dot{W}_{out})}{\sum(\dot{Q}_{in}+\dot{W}_{in})} \quad (5-11)$$

The energy efficiency for the ORC can be diverted by:

$$\eta_{en}^{ORC} = \frac{\dot{W}_{net}}{\dot{Q}_{eva}^{ORC}} \quad (5-12)$$

The RTE is defined as the ratio of the total energy output to the total energy input to the CAES system, with the subscripts net and eva denoting the net value and evaporator, respectively. RTE can be diverted by (Ding et al., 2022):

$$RTE_{CAES} = \frac{\dot{W}_{Tur}}{\dot{W}_{Com}+\dot{Q}_{fuel}} \quad (5-13)$$

The COP of the ARS can be expressed as the ratio of useful cooling provided to the required energy used to drive the single-effect LiBr/H_2O ARS. Where the subscripts Com and $fuel$ denote compressor and consumed fuel. COP can be diverted by (Ding et al., 2022):

$$COP = \frac{\dot{Q}_{EVAP}}{\dot{Q}_{DES}+\dot{W}_{pump}} \quad (5-14)$$

Based on all equations, the RTE of CCHP system can be diverted by (Ding et al., 2022):

$$RTE_{CCHP} = \frac{\dot{W}_{OT1}*t_{charging}+(\dot{W}_{HPT}+\dot{W}_{LPT}+\dot{W}_{OT2}+\dot{Q}_{cooling})*t_{discharging}}{(\dot{W}_{AC}+\dot{W}_{OP1})*t_{charging}+(\dot{Q}_{fuel}+\dot{W}_{OP2}+\dot{W}_{pump})*t_{discharging}} \quad (5-15)$$

5.2.2 Exergy analysis

Exergy efficiency is an invaluable indicator that related to the amount of available energy that can be lost or destructed. The equations used to calculate the exergy destruction of each component are derived from Eqs. (2-4) - (2-12), and itemized in Table 5-2.

Table 5-2 Exergy destruction equations of components (Alirahmi et al., 2021; Ding et al., 2022)

Components	Exergy destruction
CAES charging process	
LPC	$\dot{E}x_{LPC}^{D} = \dot{E}x_1 - \dot{E}x_2 + \dot{W}_{LPC}$
HPC1	$\dot{E}x_{HPC1}^{D} = \dot{E}x_3 - \dot{E}x_4 + \dot{W}_{HPC1}$
HPC2	$\dot{E}x_{HPC2}^{D} = \dot{E}x_5 - \dot{E}x_6 + \dot{W}_{HPC2}$
HPC3	$\dot{E}x_{HPC3}^{D} = \dot{E}x_7 - \dot{E}x_8 + \dot{W}_{HPC3}$
HPC4	$\dot{E}x_{HPC4}^{D} = \dot{E}x_9 - \dot{E}x_{10} + \dot{W}_{HPC4}$
HPC5	$\dot{E}x_{HPC5}^{D} = \dot{E}x_{11} - \dot{E}x_{12} + \dot{W}_{HPC5}$
HPC6	$\dot{E}x_{HPC6}^{D} = \dot{E}x_{13} - \dot{E}x_{14} + \dot{W}_{HPC6}$
IC1	$\dot{E}x_{IC1}^{D} = \dot{E}x_2 - \dot{E}x_3 + \dot{E}x_{24} - \dot{E}x_{25}$
IC2	$\dot{E}x_{IC2}^{D} = \dot{E}x_4 - \dot{E}x_5 + \dot{E}x_{26} - \dot{E}x_{27}$
IC3	$\dot{E}x_{IC3}^{D} = \dot{E}x_6 - \dot{E}x_7 + \dot{E}x_{28} - \dot{E}x_{29}$
IC4	$\dot{E}x_{IC4}^{D} = \dot{E}x_8 - \dot{E}x_9 + \dot{E}x_{30} - \dot{E}x_{31}$
IC5	$\dot{E}x_{IC5}^{D} = \dot{E}x_{10} - \dot{E}x_{11} + \dot{E}x_{32} - \dot{E}x_{33}$
IC6	$\dot{E}x_{IC6}^{D} = \dot{E}x_{12} - \dot{E}x_{13} + \dot{E}x_{34} - \dot{E}x_{35}$
AC	$\dot{E}x_{AC}^{D} = \dot{E}x_{14} - \dot{E}x_{15} + \dot{E}x_{36} - \dot{E}x_{37}$
Cavern	$\dot{E}x_{Cavern}^{D} = \dot{E}x_{15} - \dot{E}x_{16}$
CAES discharging process	
REG	$\dot{E}x_{REG}^{D} = \dot{E}x_{16} - \dot{E}x_{17}$
REC	$\dot{E}x_{REG}^{D} = \dot{E}x_{17} - \dot{E}x_{18} + \dot{E}x_{22} - \dot{E}x_{23}$
CC1	$\dot{E}x_{CC1}^{D} = \dot{E}x_{18} - \dot{E}x_{fuel} - \dot{E}x_{19}$

HPT	$\dot{E}x_{HPT}^{D} = \dot{E}x_{19} - \dot{E}x_{20} - \dot{W}_{HPT}$
CC2	$\dot{E}x_{CC2}^{D} = \dot{E}x_{20} - \dot{E}x_{fuel} - \dot{E}x_{21}$
LPT	$\dot{E}x_{LPT}^{D} = \dot{E}x_{21} - \dot{E}x_{22} - \dot{W}_{LPT}$
ORC	
OT1	$\dot{E}x_{OT1}^{D} = \dot{E}x_{38} - \dot{E}x_{39} - \dot{W}_{OT1}$
OC1	$\dot{E}x_{OC1}^{D} = \dot{E}x_{39} - \dot{E}x_{40} + \dot{E}x_{cu,in} - \dot{E}x_{cu,out}$
OP1	$\dot{E}x_{OP1}^{D} = \dot{E}x_{40} - \dot{E}x_{41} + \dot{W}_{OP1}$
OT2	$\dot{E}x_{OT2}^{D} = \dot{E}x_{43} - \dot{E}x_{44} - \dot{W}_{OT2}$
OC2	$\dot{E}x_{OC2}^{D} = \dot{E}x_{44} - \dot{E}x_{45} + \dot{E}x_{cu,in} - \dot{E}x_{cu,out}$
OP2	$\dot{E}x_{OP2}^{D} = \dot{E}x_{45} - \dot{E}x_{42} + \dot{W}_{OP2}$
OE2	$\dot{E}x_{OE2}^{D} = \dot{E}x_{42} - \dot{E}x_{43} + \dot{E}x_{hu,in} - \dot{E}x_{hu,out}$
ARS	
DES	$\dot{E}x_{DES}^{D} = \dot{E}x_{48} - \dot{E}x_{49} - \dot{E}x_{52} + \dot{E}x_{hu,in} - \dot{E}x_{hu,out}$
COND	$\dot{E}x_{COND}^{D} = \dot{E}x_{52} - \dot{E}x_{53} + \dot{E}x_{cu,in} - \dot{E}x_{cu,out}$
EVAP	$\dot{E}x_{EVAP}^{D} = \dot{E}x_{54} - \dot{E}x_{55} + \dot{E}x_{hu,in} - \dot{E}x_{hu,out}$
ABS	$\dot{E}x_{ABS}^{D} = \dot{E}x_{55} + \dot{E}x_{51} - \dot{E}x_{46} + \dot{E}x_{cu,in} - \dot{E}x_{cu,out}$
SHX	$\dot{E}x_{SHX}^{D} = \dot{E}x_{47} - \dot{E}x_{48} + \dot{E}x_{49} - \dot{E}x_{50}$
PUMP	$\dot{E}x_{PUMP}^{D} = \dot{E}x_{46} - \dot{E}x_{47} + \dot{W}_{PUMP}$
VAL1	$\dot{E}x_{V1}^{D} = \dot{E}x_{50} - \dot{E}x_{51}$
VAL2	$\dot{E}x_{V2}^{D} = \dot{E}x_{53} - \dot{E}x_{54}$

5.2.3 Economic analysis

To appraise the potential viability and market competitiveness of the proposed CCHP system, an economic evaluation was conducted. The insights gleaned from economic analysis are expected to inform critical decisions regarding the feasibility and commercial viability of the proposed CCHP system. The ICPP refers to investment cost per output power. These equations can be expressed as follows:

$$ICPP = \frac{\dot{C}_{total}}{\dot{W}_{AT,out}+\dot{W}_{ORC,out}} \quad (5-16)$$

$$\dot{C}_{total} = \dot{Z}_{total} + \dot{C}_{fuel} \quad (5-17)$$

$$\dot{Z}_{total} = \left(\frac{CRF}{D}\right) Z_{total} + \frac{\gamma Z_{total}}{D} \quad (5-18)$$

$$CRF = \frac{i_r(1+i_r)^N}{(1+i_r)^N-1} \quad (5-19)$$

$$\dot{C}_{fuel} = c_{fuel}\left(\dot{W}_{AC,in} + \dot{W}_{pump,all}\right) \quad (5-20)$$

Where $\dot{C}_{total}$ is the total cost rate, $\dot{Z}_{total}$ is the investment cost rate, $\dot{C}_{fuel}$ is the fuel cost rate, CRF is the capital recovery factor, γ is the maintenance factor, D is yearly operational days, i_r is the interest rate and N is the system lifetime (Details data are shown in Table 5-5).

The cost equations of system components to calculate their capital investment cost are given in Table 5-3. The cost values calculated as listed in Table 4 are obtained from the original year, and the value should be converted to from reference year (2018) into present year according to the Chemical Engineering Plant Cost Index (CEPEI) (Razmi and Janbaz, 2020):

$$Cost\ at\ present\ year = Original\ cost * \frac{CEPCI_{present}}{CEPCI_{original}} \quad (5-21)$$

Table 5-3 Cost equations of each component (Jalili, Chitsaz, and Alhuyi, 2021; Razmi et al., 2019; Akrami et al., 2017)

Components	The capital investment cost equation
CAES charging process	
LPC & HPC	$Z_k = 44.71 \frac{\dot{m}}{0.95-\eta_{AC}} \frac{P_{out}}{P_{in}} \ln\left(\frac{P_{out}}{P_{in}}\right)$

IC	$Z_k = 12{,}000\left(\frac{A_k}{100}\right)^{0.6}$, $A_k = \frac{Q_k}{U_k \times LMTD_k}$
AC	$Z_k = 12{,}000\left(\frac{A_k}{100}\right)^{0.6}$
Cavern	$Z_k = 4{,}042V_k^{0.506}$
CAES discharging process	
CC	$Z_k = 28.98\dot{m}\left(1 + e^{0.015*(T_{in}-1540)}\right)\frac{1}{0.995 - \frac{P_{out}}{P_{in}}}$
LPT & HPT	$Z_k = 301.45\dot{m}\frac{1}{0.95 - \eta_{tur}}\ln\left(\frac{P_{in}}{P_{out}}\right)\left(1 + e^{0.025(T_{in}-1{,}570)}\right)$
REC	$Z_k = 12{,}000\left(\frac{A_k}{100}\right)^{0.6}$
ORC	
OT	$Z_k = 4{,}750\left(\dot{W}_{orc,tur}\right)^{0.75}$
OC	$Z_k = 516.62(A_k)^{0.6}$
OP	$Z_k = 2{,}000\left(\dot{W}_{orc,pump}\right)^{0.65}$
OE	$Z_k = 309.14(A_k)^{0.85}$
ARS	
DES	$Z_k = 17{,}500\left(\frac{A_k}{100}\right)^{0.6}$
COND	$Z_k = 8{,}000\left(\frac{A_k}{100}\right)^{0.6}$
EVAP	$Z_k = 16{,}000\left(\frac{A_k}{100}\right)^{0.6}$
ABS	$Z_k = 16{,}000\left(\frac{A_k}{100}\right)^{0.6}$
SHX	$Z_k = 12{,}000\left(\frac{A_k}{100}\right)^{0.6}$
PUMP	$Z_k = 2{,}000\left(\dot{W}_{LiBr,pump}\right)^{0.65}$
VAL1	$Z_k \cong 0$
VAL2	$Z_k \cong 0$

5.3 CCHP Optimisation

A multi-objective optimisation was performed to make a trade-off between investment cost and thermodynamic performance. Herein, the NSGA-II method was employed for the optimisation, which is generally used to find the optimal solution (Yang et al., 2022).

RTE (to be maximised) and ICPP (to be minimised) were selected as two conflicting objective functions, and the model was formulated.

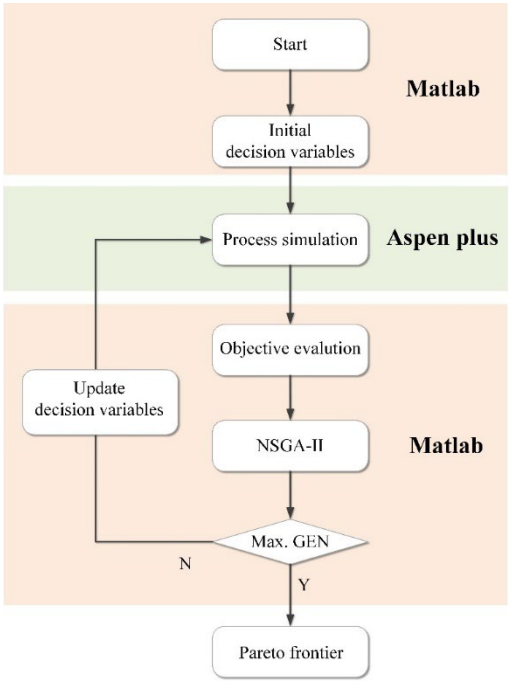

Figure 5-2 The flowchart of the simulation-based multi-objective optimisation framework

The flowchart of the whole optimisation procedure is shown in Figure 5-2. It displays the interaction between Aspen plus® and MATLAB. The initial decision variables were generated first and then transferred to Aspen plus®. The investigated system was simulated in Aspen plus®. Based on the simulated results, the objective functions were calculated. In the next step, the feasible solution generated in the previous step were sorted. New decision variables were generated if the maximum iteration has not been reached.

The algorithm was configured to operate within a pre-specified set of parameters, with a maximum of 1,000 iterations, a population size of 100, a crossover percentage of 0.5, a mutation ratio of 0.02, and a mutation step size of 10% of the difference between the upper and lower limits of the variables.

Following 1,000 iterations, the algorithm converged to an optimal solution, represented by a Pareto frontier that encapsulates the optimal trade-offs between various competing objectives. To identify the best solution within this frontier, the Technique for Order of Preference by Similarity to Ideal Solution (TOPSIS) method was employed. This method evaluates the relative distance of each potential solution from an idealized reference point and selects the one with the shortest geometric distance.

5.4 Results of the multi-objective optimisation

The investigated CCHP system has been simulated in Aspen plus®, and the simulated results were used to calculate the two objectives. The decision variables were considered as the inlet temperature of the combustion chamber ($T_{cc,in}$), evaporation temperature (T_{oe1}, T_{oe2}), condensation temperature (T_{oc1}, T_{oc2}), mass flowrate of the ORC working fluid (m_{wf1}, m_{wf2}), desorber temperature (T_{des}), absorber temperature (T_{abs}) and mass flowrate of the ARS (m_{ars}) (Sadreddini et al., 2018; Kaushik and Arora, 2009). Based on these simulation techniques, the final variables for CCHP system investigated are listed in Table 5-4.

Table 5-4 The lower bound and upper bound of decision variables

Variables	Lower bound	Upper bound
$T_{cc,in}$ (℃)	35	75
T_{oe1} (℃)	70	100
T_{oe2} (℃)	70	120
T_{oc1} (℃)	30	70
T_{oc2} (℃)	30	70
m_{wf1} (kg/s)	0	1,000
m_{wf2} (kg/s)	0	1,000
T_{des} (℃)	80	110
T_{abs} (℃)	30	40
m_{ars} (kg/s)	0	1,000

The assumed input parameters' design conditions of the CCHP system are shown in Table 5-5.

Table 5-5 Design conditions of CCHP system (Ding et al., 2022; Yang et al., 2022)

Parameters	Value	Unit
Equipment parameters		
CAES Compressor isentropic efficiency	75	%
ORC turbine isentropic efficiency	80	%
ORC pump isentropic efficiency	80	%
HPT isentropic efficiency	93	%
LPT isentropic efficiency	93	%
ARS pump isentropic efficiency	85	%
Economic parameters		
i_r	0.12	/
N	25	y
D	300	d
γ	0.06	/
c_{fuel}	0.03	\$/kWh

Figure 5-3 shows the Pareto front obtained from the multi-objective optimisation.

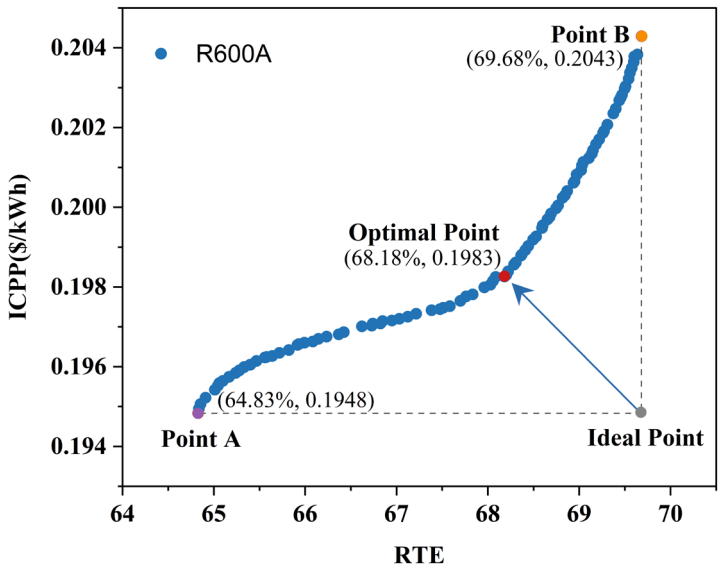

Figure 5-3 Pareto front of CCHP system

The system configuration that yielded the highest RTE (69.68%) was at Point B, which corresponded to the highest ICPP of 0.2043 $/kWh. On the other hand, the CCHP system exhibited the lowest RTE of 64.83% and the lowest ICPP of 0.1948 $/kWh. The optimal configuration that represented the optimal trade-offs between the competing objectives was determined using the TOPSIS method and corresponded to an RTE of 68.18% and an ICPP of 0.1983 $/kWh.

The optimised decision variables have been listed in Table 5-6, and a comprehensive breakdown of these variables is presented in Table 5-7. Additionally, Table 5-8 outlines the decision variables for each of the evaluated CCHP systems.

Table 5-6 Decision variables of the CCHP system

Variables	Basic case	Optimal case
$T_{cc,in}$ (℃)	560.20	490.00
T_{oe1} (℃)	100.00	70.00
T_{oe2} (℃)	100.00	70.16
T_{oc1} (℃)	30.00	30.00
T_{oc2} (℃)	30.00	30.00
m_{wf1} (kg/s)	528.00	561.05
m_{wf2} (kg/s)	8.00	15.05
T_{des} (℃)	89.90	91.61
T_{abs} (℃)	32.70	34.46
m_{ars} (kg/s)	1.00	49.12

Table 5-7 Performance indicators of CCHP system

Variables	Basic case	Optimal case
$\dot{W}_{AC}$ (kW)	218,421.63	218,421.63

$\dot{W}_{HPT}$ (kW)	28,497.17	28,492.50
$\dot{W}_{LPT}$ (kW)	177,390.27	177,147.92
$\dot{Q}_{fuel}$ (kW)	222,683.72	222,683.72
$\dot{W}_{OT1}$ (kW)	27,567.82	19,607.18
$\dot{W}_{OT2}$ (kW)	522.12	528.11
$\dot{W}_{OP1}$ (kW)	830.79	877.22
$\dot{W}_{OP2}$ (kW)	36.36	23.67
$\dot{W}_{pump}$ (kW)	0.01	0.28
$\dot{Q}_{cooling}$ (kW)	245.47	10,635.97
η_{ORC1}	12.14	8.51
η_{ORC2}	11.95	8.53
COP	0.74	0.78
RTE (%)	66.35	68.18
$Z_{charging}$ ($)	6,963,389.46	5,687,444.19
$Z_{discharging}$ ($)	42,662,850.36	42,264,709.19
Z_{ORC} ($)	17,108,388.96	12,358,583.19
Z_{ARS} ($)	263,379.06	781,626.61
Z_{total} ($)	66,998,007.84	61,092,363.18
$\dot{Z}_{total}$ ($)	41,873.75	38,182.72
$\dot{C}_{fuel}$ ($)	6,610.90	6,579.52
$\dot{C}_{total}$ ($)	48,484.64	44,762.24
ICPP ($/kWh)	0.2038	0.1983

The findings reveal that the inlet temperature of the combustion chamber underwent a significant decrease of 12.53%, from 560.20°C to 490.00°C. Consequently, the heat load of the recuperator decreased, enabling the ORC and ARS subsystems to recover more waste heat from the flue gas in the discharging process. This increase is reflected in the growth of the mass flow of the ORC2 and ARS, which rose to 15.05 kg/s and 49.12 kg/s, respectively. Notably, the cooling capacity of the ARS subsystem increased substantially from 245.47 kW to 10,635.97 kW, which is a direct consequence of the increase in the mass flowrate of the subsystem. Furthermore, the rise in desorber and absorber temperature contributed to an increase in the heat loads of the condenser and evaporator and a reduction in absorber heat duty, ultimately leading to an improvement in COP by 4.75% from 0.74 to 0.78. These results demonstrate that an increased flowrate and improved desorber and absorber temperatures of the ARS subsystem can lead to improved sub-process performance.

Table 5-8 The decision variables at optimal point

Variables	**R600A**	**R600**	**R601**	**R245FA**	**R245CA**
$T_{cc,in}$ (℃)	490.00	490.75	490.00	490.01	490.00
T_{oe1} (℃)	70.00	70.01	76.80	74.66	73.15
T_{oe2} (℃)	70.16	70.01	70.27	70.36	70.00
T_{oc1} (℃)	30.00	30.00	30.00	30.00	30.00
T_{oc2} (℃)	30.00	30.00	30.00	30.00	30.00
m_{wf1} (kg/s)	561.05	515.62	494.46	943.01	908.38
m_{wf2} (kg/s)	15.05	13.02	13.91	26.47	24.95
T_{des} (℃)	91.61	96.49	89.79	89.00	90.66
T_{abs} (℃)	34.46	34.96	34.97	34.76	34.88
m_{ars} (kg/s)	49.12	36.48	56.09	59.74	52.52

During the charging process of the ORC, the mass flowrate of working fluid increased from 528.00 kg/s to 561.05 kg/s, while the power generated by the turbine decreased from 27,567.82 kW to 19,607.18 kW. As a result of the decrease in evaporator temperature from 100°C to 70.00°C, the ORC efficiency worsened from 12.14% to 8.51%. However, the reduction in evaporator temperature increased the temperature difference of the heat exchanger, which, in turn, led to a reduction in the heat exchanger area. This is the primary reason for reducing the cost of the ICs and AC and the evaporator in ORC2. From an economic standpoint, decreasing the evaporator temperature has the advantage of reducing ICPP.

5.4.1 Energy analysis

As previously mentioned, the decrease in evaporator temperature resulted in the reduction of the ORC system. The COP of the ARS was enhanced by 3.82%, and the RTE of the entire system went from 66.35% to 68.38%. These data indicate that the overall system efficiency of the process has increased; however, the ORC efficiency has decreased.

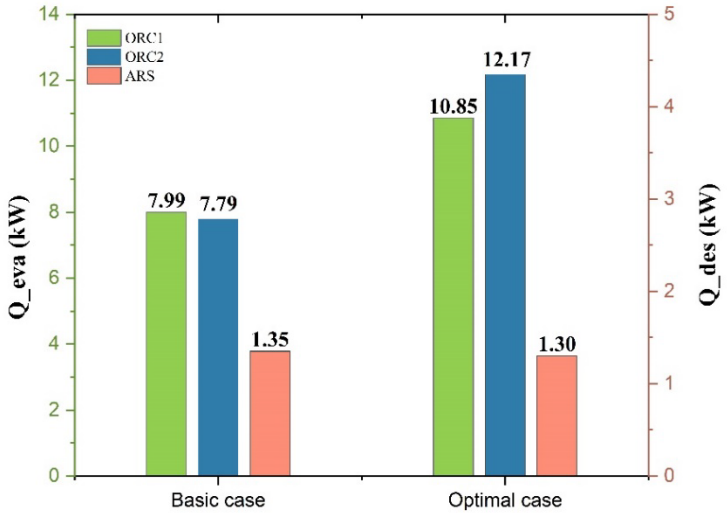

Figure 5-4 The heat per power and per cooling capacity generated

Furthermore, it is noted that the power generated by ORC per mass is much less than the cooling capacity generated by the ARS. Figure 5-4 shows the needed heat duty to generate per power in ORC and per cooling capacity in ARS. Generating per cooling capacity needs less waste heat. In other words, under the same waste heat conditions, the ARS could generate more cooling

capacity. Using the ARS to recover waste heat is greater than ORC in the suggested CCHP system. In the optimal case, the desorber needs less heat to generate per cooling capacity, which corresponds to the improved COP.

5.4.2 Exergy analysis

Figure 5-5 shows the exergy analysis results for the CCHP system based on the optimal operating condition in Table 5-8. The inner circle is the distribution of the four subsections. For the outer circle, it illustrates each component's detailed exergy destruction distribution. It is noted that the total exergy was destructed by 57.90% in discharging process, where the most significant unit operations are combustion chamber with the highest exergy destruction (48.90%). It should be mentioned that the exergy destruction of combustion chamber is 160,635 kW (as discussed in section 4.3), it decreased to 151,981 kW after multi-objective optimisation. The reason is that combustion is an irreversibility process, which results in the highest level of exergy destruction.

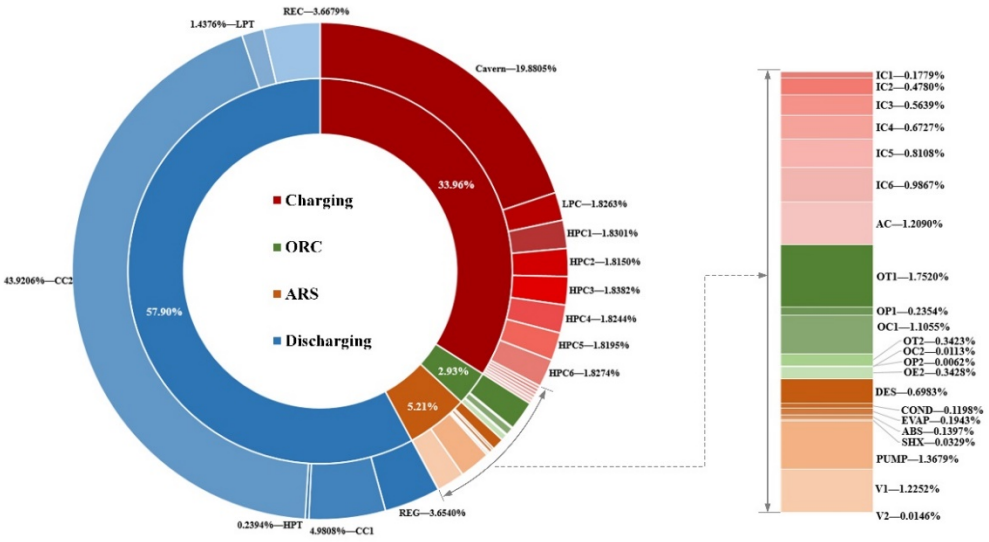

Figure 5-5 Exergy destruction of all components

During the charging process, the amount of exergy loss was the second large sub-section, which reached up to 33.96%. The amount of exergy loss was identified in the carven, which accounted for 19.88% of the total exergy loss and was the second-highest exergy destruction unit. The compressors and valves also exhibited significant exergy losses, primarily attributed to the inherent irreversibility of the pressure change process. Moreover, the heat exchangers contributed to the fourth largest proportion of exergy losses. The

reason is the significant temperature difference between the hot and cold flow entering these components.

5.4.3 Economic analysis

To determine the economic viability of the proposed CCHP system, an ICPP-based economic study was conducted. The cost of each piece of equipment is listed in Table 5-9.

Table 5-9 The cost of each component in the CCHP system

System component	Cost (k$)	Proportion of total cost (%)
CAES charging process		
LPC	141.19	0.2301
HPC1	141.19	0.2301
HPC2	141.19	0.2301
HPC3	141.19	0.2301
HPC4	141.19	0.2301
HPC5	141.19	0.2301
HPC6	141.19	0.2301
IC1	796.10	1.2971
IC2	780.80	1.2722
IC3	782.61	1.2752
IC4	786.14	1.2809
IC5	168.81	0.2751
IC6	171.52	0.2795
AC	176.20	0.2871
CARVEN	1,217.83	1.9843
Charging process	5,868.39	9.5617

CAES discharging process		
CC1	220.87	0.3599
HPT	2,446.70	3.9866
CC2	807.00	1.3149
LPT	38,237.61	62.3028
REC	552.53	0.9003
Discharging process	42,264.71	68.8644
ORC		
OT1	10,933.80	17.8151
OP1	99.80	0.1626
OC1	384.40	0.6263
OT2	674.77	1.0994
OP2	8.42	0.0137
OC2	47.49	0.0774
OE2	303.58	0.4946
ORC	12,452.25	20.2892
ARS		
DES	473.57	0.7716
COND	37.68	0.0614
EVAP	108.63	0.1770
ABS	120.46	0.1963
SHX	46.80	0.0763
PUMP	1.29	0.0021
V1	0	0.0000

V2	0	0.0000
ARS	788.43	1.2846
Total	61,373.78	100

The cost distributions of the whole system and each subsection are illustrated in Figure 5-6.

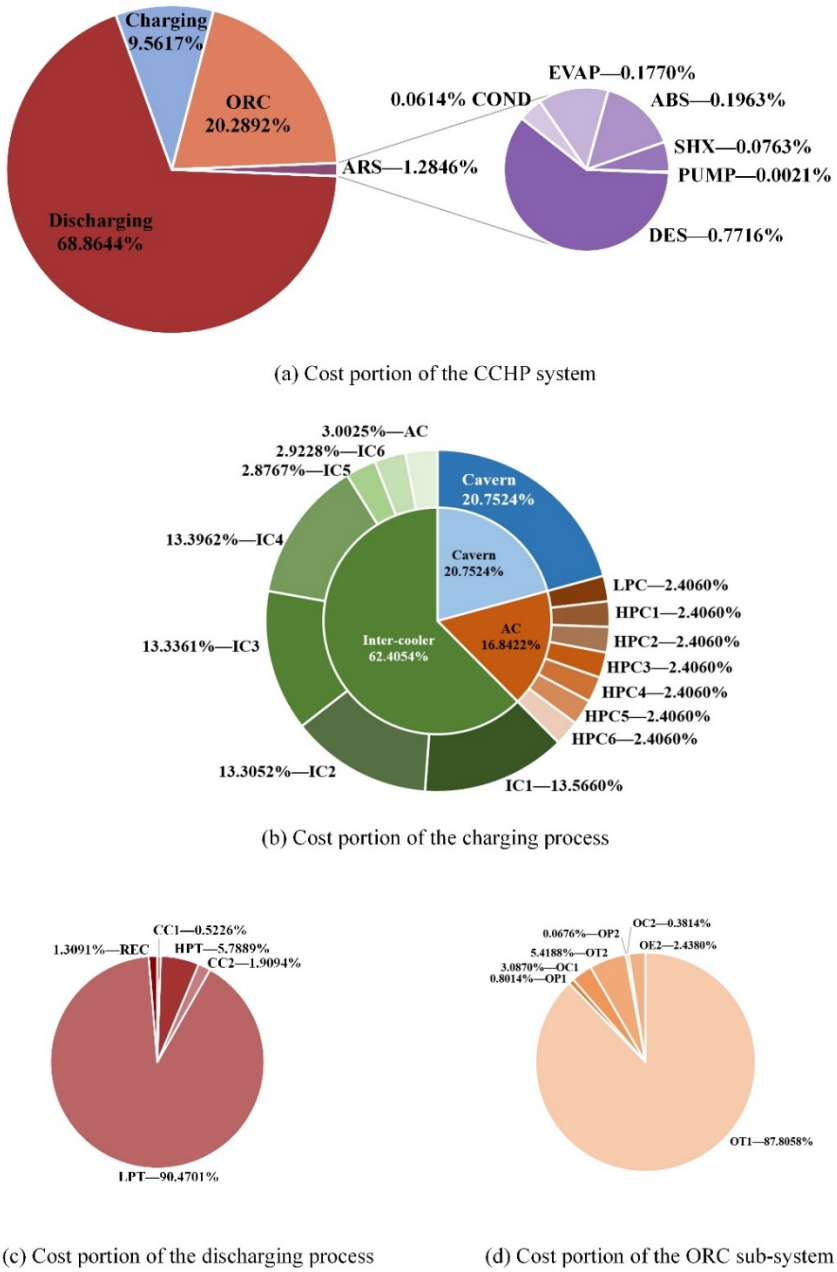

Figure 5-6 Cost distribution of CCHP system

One can observe that the cost of discharging process is the highest among the four subsections. Based on the cost calculation equations, LPT accounted for

the highest proportion of the total cost (62.30%) in the discharging process. It is highly due to the large pressure drop and high turbine temperature. Therefore, it is significant equipment when building a new commercial CAES plant. It suggests a potential for enhancement, where additional process optimisation possibilities exist to minimise equipment cost. During the discharging process, another high-cost equipment was the HPT, with a proportion of the total cost at 3.99% and the proportion of the discharging subsection at 5.79%. Furthermore, as shown in Figure 5-6 (b), the percentage of inter-coolers was 62.41%, which ranks first in the charging process. Notably, the cost of IC5, IC6 and AC was lower than the rest ICs. The reason is that the heat transfer coefficient of the high-pressure is higher than that of the low-pressure, resulting in a decrease in the heat exchanger area. In Figure 5-6 (a), the ARS subsystem accounted for 1.28% of the total cost, while the ORC2 subsystem made up 1.69%. The comparison of these percentages reveals that the ARS subsystem is more economically feasible than the ORC2 subsystem.

5.5 Conclusion

In this chapter, the investigation of a CCHP system that incorporates CAES, ORC and ARS technologies. To fully explore the heat recovery and reutilisation potential of the CCHP system, a multi-objective optimisation approach was employed to achieve a balance between a higher RTE and a lower ICPP. Subsequently, a comprehensive analysis was performed to examine the optimised system's energy, exergy and economic performance. The significant conclusions are summarised as follow:

(1) The multi-objective optimisation results show that the RTE and ICPP of the optimal suggested CCHP system can reach up to 68.38 % (increased by 0.78 %) and 0.1984 $/kWh (decreased by 2.68 %), respectively.
(2) Based on the optimal results, the exergy analysis results indicate that the discharging process is a significant subsection that accounts for the largest proportion of the exergy destruction (57.90 %).
(3) The ARS has an economic advantage over ORC, making up 1.2846 % and 1.6852 % of the total cost.

6. Thermodynamic and economic analysis of CCHP with different types of ARS

6.1 Overview

In this chapter, a new process design for CCHP system was developed. The ORC only operates during the charging process. The ARS only operated during the discharging process. Under the design conditions, the waste low-grade heat from the flue gas was all used for supplying ARS. The performance of the CCHP system with different types of ARS (single-effect using different working media and double-effect using different working media) is compared. The different effects and different working media of ARS were compared to analyse the effects on the CCHP performance. Section 6.2 describes the configuration of the proposed CCHP system. Section 6.3 illustrates the performance analysis methodologies and Section 6.4 presents the results of energy and economic analysis. Section 6.5 draws the main findings of this chapter.

6.2 Process description of CCHP

The proposed CCHP system includes CAES, ORC and different types of ARS. The most commonly used working media of ARS are LiBr/H_2O and NH_3/H_2O (Herold and Klein, 2016).

6.2.1 CCHP with single-effect ARS

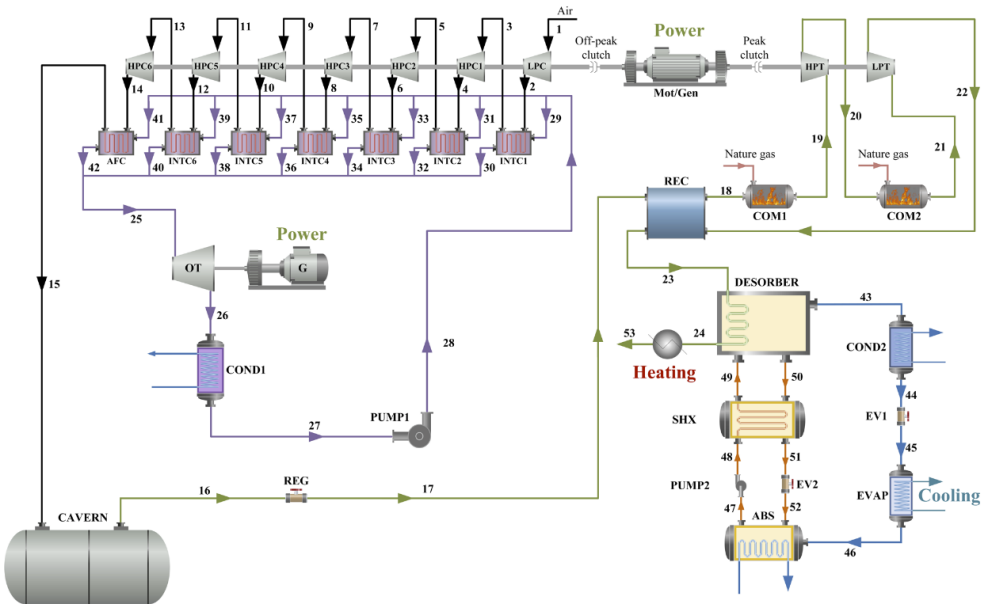

Figure 6-1 The flowsheet of CCHP-1 and CCHP-2 system (D-CAES, ORC and single-effect ARS [using LiBr/H_2O and NH_3/H_2O respectively])

ARS systems can be categorised into single-effect ARS and double-effect ARS (Herold and Klein, 2016). The CAES and ORC integrated with the single-effect ARS is referred to as CCHP-1 (using LiBr/H_2O) and CCHP-2 (using NH_3-H_2O). The CAES and ORC integrated with the double-effect ARS is referred to as CCHP-3 (using LiBr/H_2O) and CCHP-4 (using NH_3-H_2O). This labelling system enables an efficient comparison of the different configurations, thereby elucidating the relative merits and shortcomings of each.

During the off-peak period, excess electricity from renewable sources, such as wind or solar energy, can be used to drive multi-stage compressors (one LPC and six HPCs), through which compressed high-pressure air is injected into a cavern. At the same time, the large amount of waste heat generated by the multi-stage compressors during compression can be recovered by inter-coolers and after-cooler and used as a heat source (stream 25 in Figure 6-1) for the ORC. In the ORC, R600a was chosen as the organic working fluid due to its low global warming potential (GWP=3) and ozone depletion potential (ODP=0) (Bolaji and Huan, 2013). The ORC includes evaporator (six INTCs and one AFC), a turbine (OT), a condenser (COND1) and a pump (PUMP1). The evaporator is responsible for recovering waste heat and converting the organic working fluid (R600a) into saturated vapour. The evaporated fluid is channelled into the turbine to generate electricity.

During the peak period, high-pressure compressed air is released from the cavern, the stream is heated by a recuperator (REC) and directed to the combustion chambers (COM1 and COM2) for fuel combustion. The resulting energy is harnessed to generate electricity using turbines. During discharging, low-temperature waste heat at the REC outlet can drive the ARS. The ARS may be characterized as a thermodynamically driven cooling technology, designed to utilize low-grade thermal energy sources for cooling. In the desorber, waste heat is utilized to heat the solution and separate the gaseous refrigerant from the liquid solution. The concentrated salt solution leaving the desorber passes through a solution heat exchanger (SHX) and exchanges energy with the solution leaving the absorber. The evaporated gaseous refrigerant is then directed into the condenser (COND2) by a baffle plate and cooled by cooling water. Following condensation, the refrigerant undergoes a process of

depressurization before being channelled into the evaporator (EVAP). This transition fosters the production of chilled water at a lower temperature, serving a vital role in the cooling process. The highly concentrated solution combines with water vapour, becoming a dilute solution that collects at the bottom of the absorber and is sent back to the desorber via a solution pump (PUMP2).

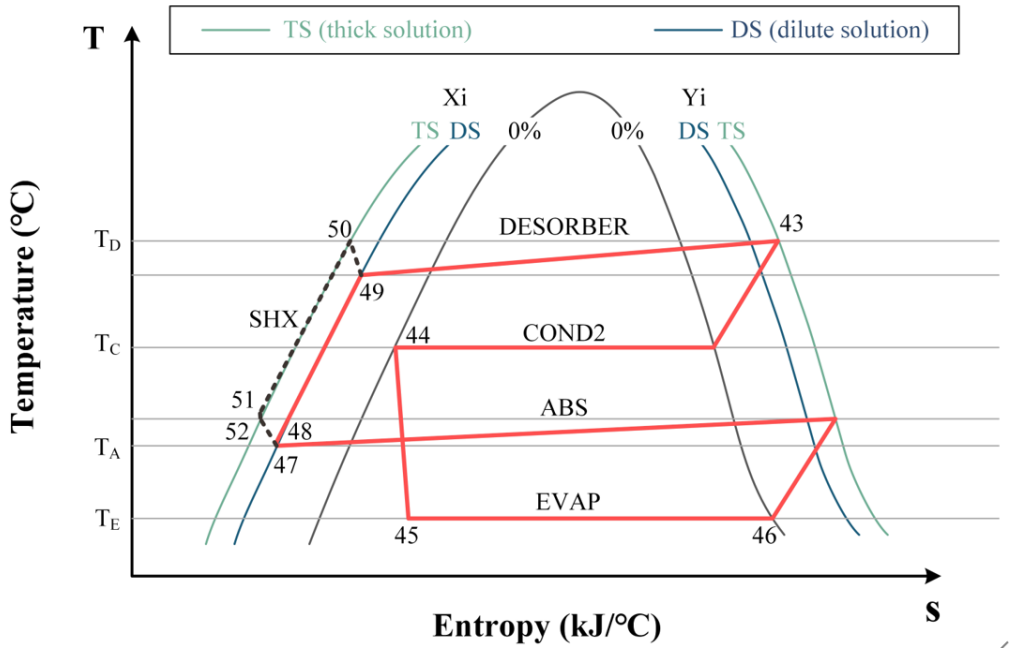

Figure 6-2 The T-S diagram of the single-effect ARS

Figure 6-2 shows that T–S diagram of single-effect ARS. The Yi lines denote the saturated vapour line of the refrigerant, while the Xi lines represent the saturated liquid line. TS means the concentration of the thick solution and DS means the concentration of the dilute solution. The T-S diagram represents refrigerant properties related to the mixture. The refrigerant and solution circuits (between points 47 and 49) overlap can be identified. The refrigerant circuit involves the following streams: 49, 43, 44, 45, 46, 47, 48, 49. The solution circuit involves the following streams: 49, 50, 51, 52, 47, 48, 49.

6.2.2 CCHP with double-effect ARS

The process flow diagram of another proposed CCHP system (D-CAES, ORC and double-effect ARS) design is illustrated in Figure 6-3 (CCHP-3 using LiBr/H_2O and CCHP-4 using NH_3/H_2O). The double-effect ARS has two solution heat exchangers (SHX) for internal heat exchange between the high temperature condenser (COND3) and the lower-pressure desorber (DESORBER). The double-effect ARS has a higher-pressure level. The

refrigerant is produced in both the desorber and the second-effect desorber, thus increasing the amount of water vapour produced with the same amount of heat input (Somers et al., 2011).

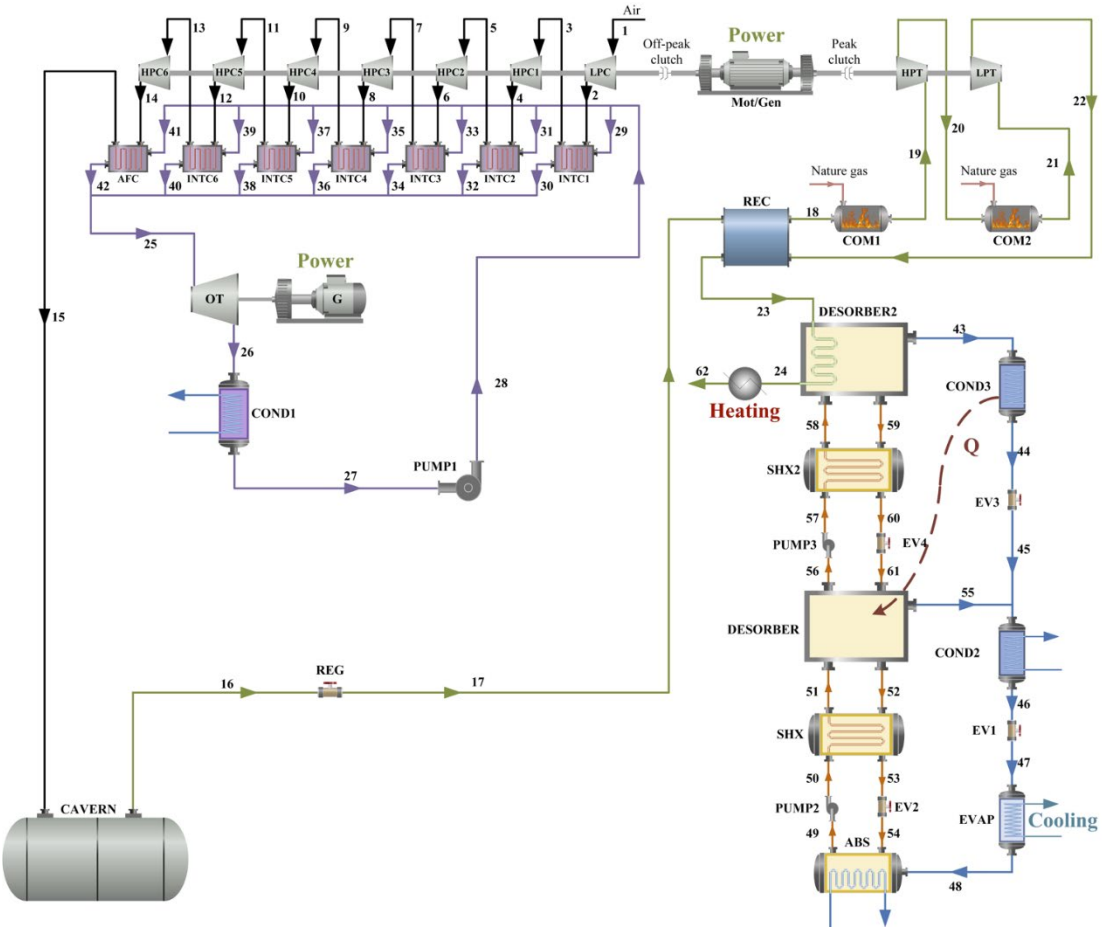

Figure 6-3 The proposed CCHP-3 and CCHP-4 system (D-CAES, ORC and double-effect ARS [LiBr/H_2O and NH_3/H_2O])

Figure 6-4 shows that T–S diagram of double-effect ARS. The refrigerant circuit involves the following streams: 58, 43, 44, 45, 46, 47, 48, 49, 50, 51, 55, 56, 57, 58. The solution circuit involves the following streams: 58, 59, 60, 61, 52, 53, 54, 49, 50, 51, 56, 57, 58. The refrigerant and solution circuits overlap between points 49 and 51, 56 and 58.

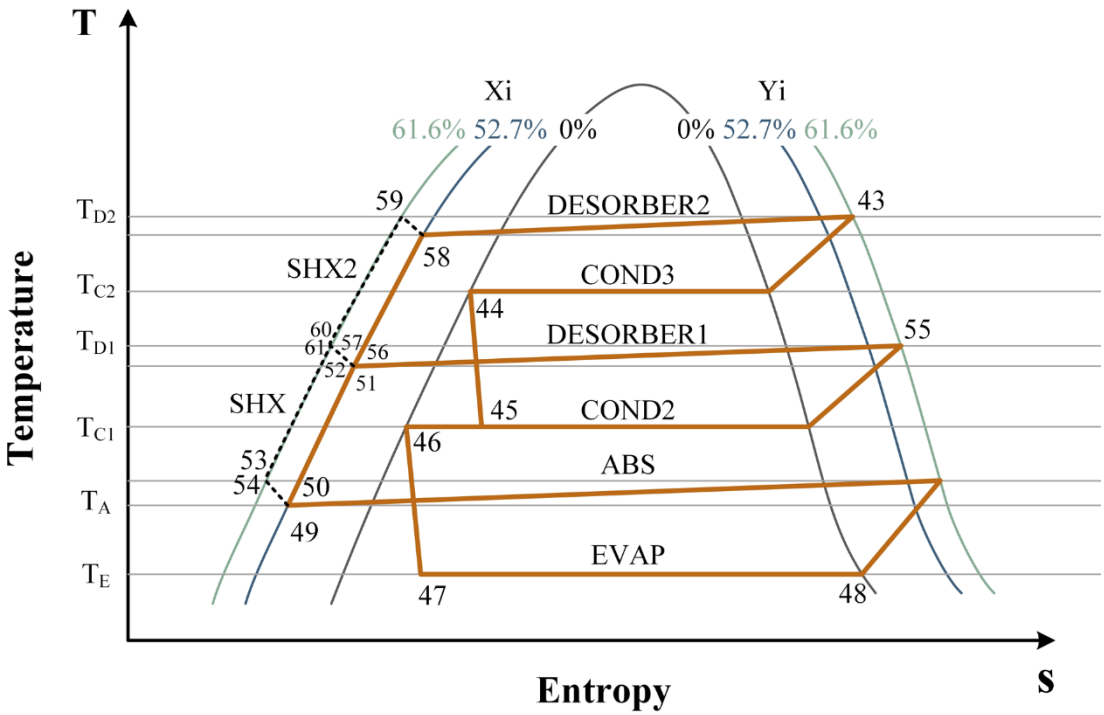

Figure 6-4 The T-S diagram of the double-effect ARS

6.3 Process analysis

The boundary conditions and parameters such as compressor outlet mass flowrate, charging and the discharging time, recuperator outlet temperature (desorber inlet temperature) and desorber outlet temperature. A summary of the baseline boundary conditions, and design point parameters are given in in Table 6-1.

Table 6-1 The input parameters of CCHP system at design condition

CAES charging Process		
Parameter	Value	Unit
Ambient temperature	25	°C
Ambient pressure	1.013	bar
Pressure ratio of compressor	1.96177	-
Mass flowrate of compressor outlet	353	kg/s
Compressor isentropic efficiency	75	%
Charging time	3	hour
ORC		
ORC turbine inlet pressure	19.85	bar
ORC Condenser pressure	4	bar

ORC evaporator temperature	100	°C
ORC condenser temperature	30	°C
ORC turbine isentropic efficiency	90	%
ORC pump isentropic efficiency	90	%
CAES discharging Process		
Discharging time	6	hour
Inlet pressure of high-pressure turbine	34.40	bar
Turbine isentropic efficiency	93	%
Inlet pressure of low-pressure turbine	17.93	bar
Fuel inlet pressure of combustor 1	44.82	bar
Fuel inlet pressure of combustor 2	24.13	bar
Fuel inlet temperature of combustor 1	32.22	°C
Fuel inlet temperature of combustor 2	32.22	°C
ARS		
Recuperator outlet temperature Desorber inlet temperature)	210	°C
Desorber outlet temperature	120	°C
CCHP-1 ARS mass flowrate	55	kg/s
CCHP-2 ARS mass flowrate	72	kg/s
CCHP3 ARS mass flowrate	76	kg/s
CCHP4 ARS mass flowrate	156	kg/s

6.3.1 Effect of recuperator outlet temperature and ARS mass flowrate on CCHP-1

Figure 6-5 shows the effect of the recuperator outlet temperature and ARS mass flowrate on the CCHP-1 system performance. Different ARS applications have different heat transfer requirements. By adjusting the mass flowrate, the heat transfer rate can be regulated to meet the specific needs of the ARS system. The results showed that COP and RTE are increasing when the mass flowrate is between 30-40 kg/s except 210°C. At this temperature, the mass flowrate appears to have been optimally calibrated to the system's requirements up to 30 kg/s. The observation that the COP exhibits a maximum, which indicates the presence of several competing factors or changes happening as the temperature increases in a system. With increasing

recuperator outlet temperature, the amount of cooling capacity increases, while the heating decreases. The reason is that the total amount of waste heat is the same, and the waste heat is divided into two parts. One part is used to drive the ARS, which corresponds to the heat provided to the desorber. The other is treated as heating output. It means that the more heat provided to the desorber, the less heat will be used for heating. Notably, beyond the 40 kg/s threshold in mass flowrate, both the COP and RTE manifest a declining pattern. This could be attributed to the practical limitations in the operational range of an ARS application. Additionally, an elevation in the recuperator outlet temperature could engender an increase in heat transfer irreversibility within the heat exchangers.

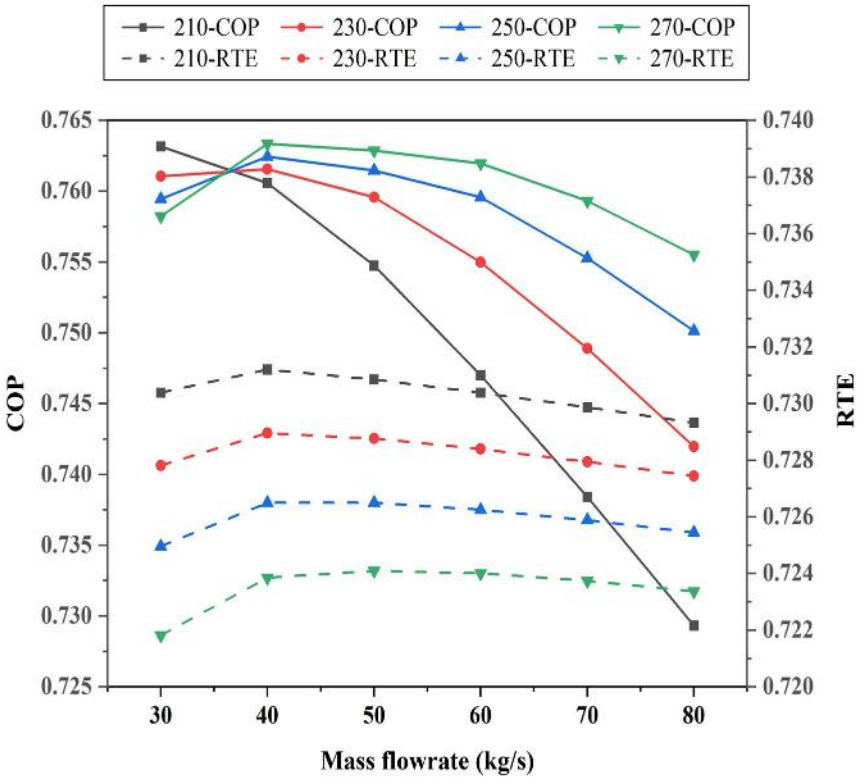

Figure 6-5 Effect of recuperator outlet temperature and ARS mass flowrate on CCHP-1

6.3.2 Effect of recuperator outlet temperature and ARS mass flowrate on CCHP-2

Figure 6-6 shows the effect of the recuperator outlet temperature and ARS mass flowrate on the CCHP-2 system performance. CCHP-2 system was designed with higher mass flowrate than CCHP-1. Due to the latent heat of

NH_3/H_2O is lower than $LiBr/H_2O$. The recuperator outlet temperature and ARS mass flowrate were varied while other parameters were fixed at the baseline value. The results showed that COP and RTE increased with the mass flowrate. The COP plot helps to explain one of the primary effects. As the recuperator outlet temperature increases, more heat could be transferred to ARS. It leads to an increase in refrigerant temperature and the solution in the desorber, which has a positive effect on enhancement of COP. When the ARS mass flowrate is about 100 kg/s and the recuperator outlet temperature is about 210°C, the CCHP-2 system performance could achieve an optimum condition.

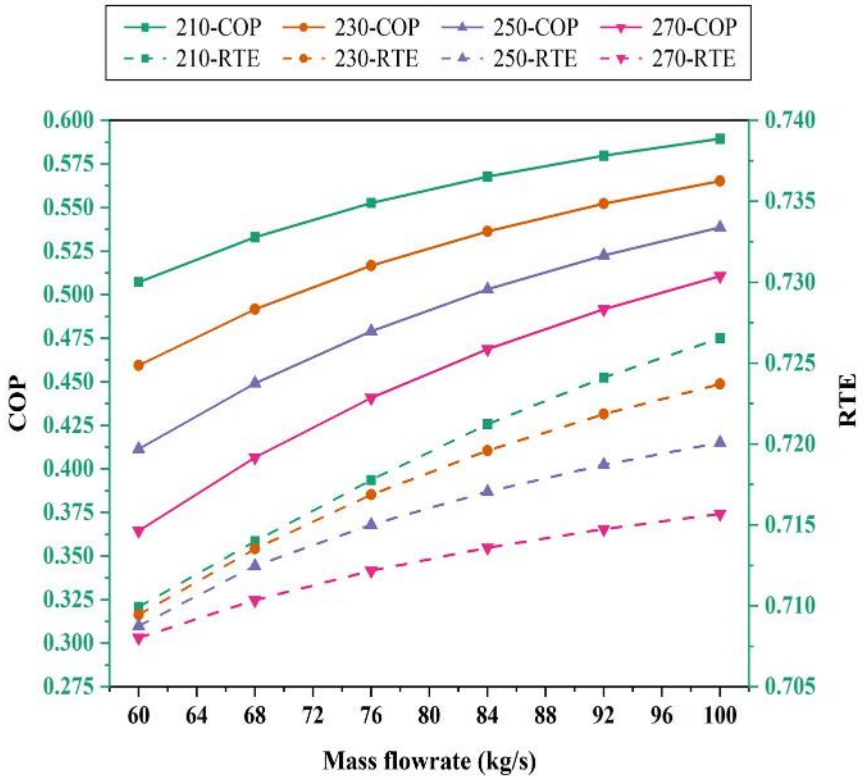

Figure 6-6 Effect of recuperator outlet temperature and ARS mass flowrate on CCHP-2

6.3.3 Effect of recuperator outlet temperature and ARS mass flowrate on CCHP-3

Figure 6-7 shows the effect of the recuperator outlet temperature and ARS mass flowrate on the CCHP-3 system performance. The recuperator outlet temperature and ARS mass flowrate were optimised while other parameters were fixed at the baseline value. The results indicate that both COP and RTE exhibited a positive effect on mass flowrate. Remarkably, the COP plot unveils

a primary effect - an increase in recuperator outlet temperature leads to a corresponding increase in COP. As the recuperator outlet temperature increases, more heat could be transferred to ARS. It has a positive effect on COP. Notably, at a mass flowrate of approximately 120 kg/s and a recuperator outlet temperature of 210°C, the CCHP-3 system's performance attains an optimal condition. These results highlight the crucial role of mass flowrate in enhancing the performance of CCHP systems when integrated with the ARS.

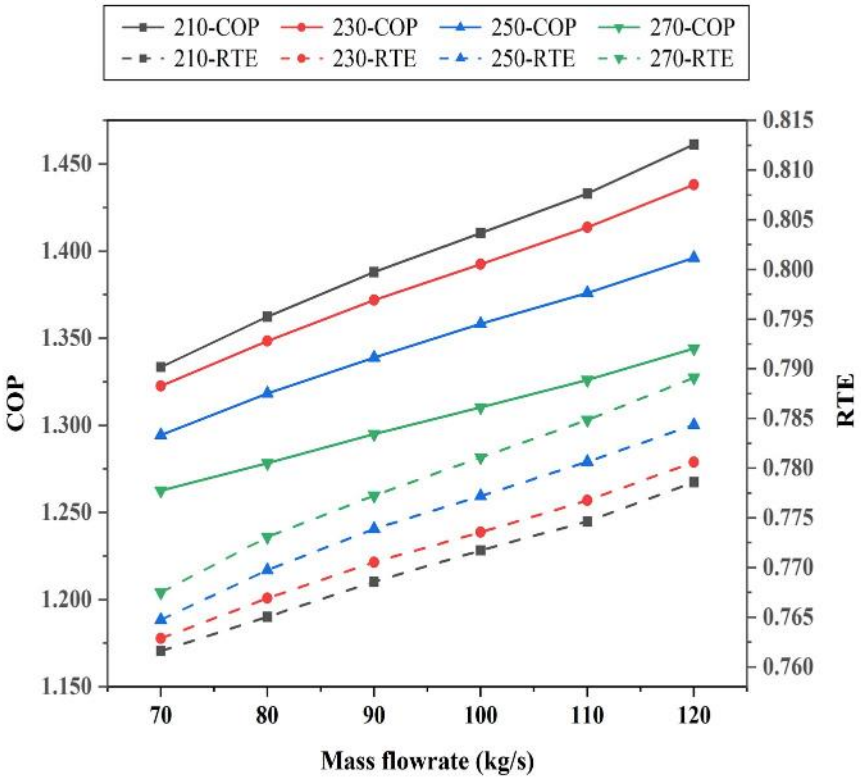

Figure 6-7 Effect of recuperator outlet temperature and ARS mass flowrate on CCHP-3

6.3.4 Effect of recuperator outlet temperature and ARS mass flowrate on CCHP-4

Figure 6-8 shows the effect of the recuperator outlet temperature and ARS mass flowrate on the CCHP-4 system performance. The recuperator outlet temperature and ARS mass flowrate were optimised while holding all other parameters at the baseline value. The results showed that COP and RTE increased with the mass flowrate. COP and RTE exhibit a positive correlation

with mass flowrate. The COP plot helps to explain one of the primary effects. As the recuperator outlet temperature increases, the COP also increases. Remarkably, the optimal condition for CCHP-4 system performance can be achieved when the ARS mass flowrate is 180 kg/s and the recuperator outlet temperature is 210°C.

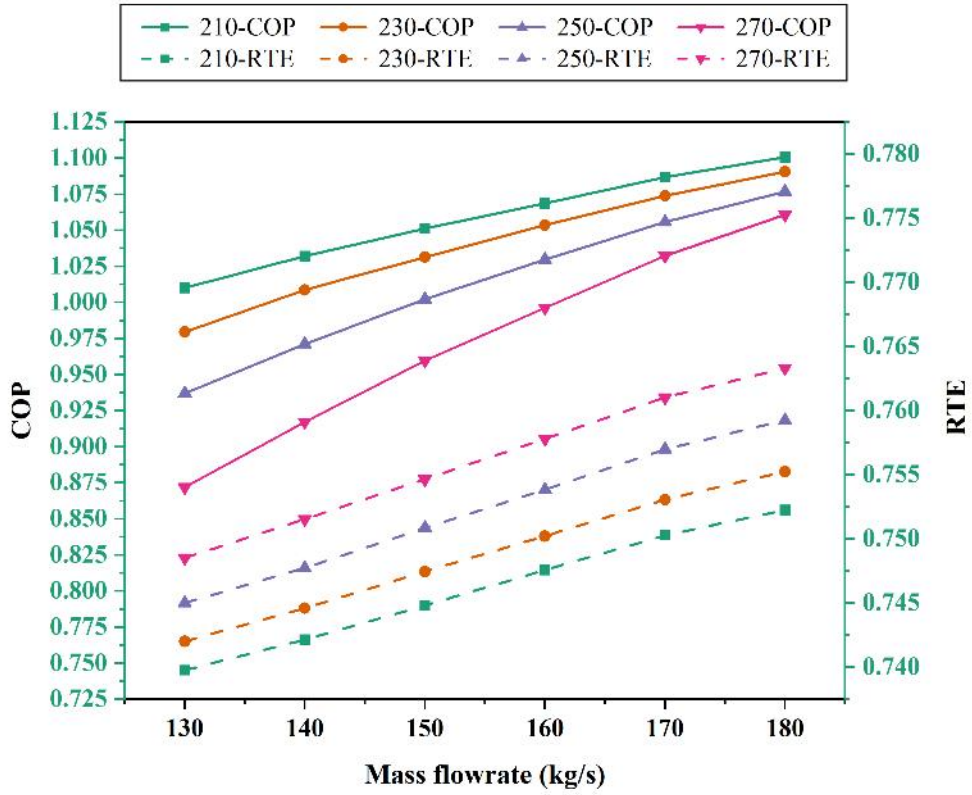

Figure 6-8 Effect of recuperator outlet temperature and ARS mass flowrate on CCHP-4

6.3.5 Performance comparisons among different cases (CCHP-1, CHHP-2, CCHP-3, and CCHP-4)

The proposed CCHP system is a novel design and has not yet been deployed commercially, hence the overall performance of the system has not been evaluated. However, the individual components of the system (i.e., CAES, ORC, and ARS) were simulated independently to ensure the accuracy of each component model in Chapter 3. The system performances under simulation conditions are presented in Table 6-2.

Table 6-2 Performance indicators of the CCHP system

CAES		
Parameter	**Value**	**Unit**
$\dot{W}_{comp,total}$	218.42	MW_e
$\dot{Q}_{Inter-cooler1-6}$	185.52	MW_{th}
$\dot{Q}_{After-cooler}$	34.74	MW_{th}
$\dot{W}_{HPT}$	28.50	MW_e
$\dot{W}_{LPT}$	177.39	MW_e
$\dot{Q}_{Com1-2}$	105.61	MW_e
$\dot{Q}_{Rec}$	85.64	MW_{th}
ORC		
$\dot{W}_{ORC-Turbine}$	23.58	MW_e
$\dot{Q}_{ORC-Condenser}$	176.99	MW_{th}
Single-effect $LiBr/H_2O$ ARS		
$\dot{Q}_{cooling}$	15.41	MW_{th}
COP	0.75	—
Single-effect NH_3-H_2O ARS		
$\dot{Q}_{cooling}$	10.84	MW_{th}
COP	0.54	—
Double-effect $LiBr/H_2O$ ARS		
$\dot{Q}_{cooling}$	27.28	MW_{th}
COP	1.36	—
Double-effect NH_3-H_2O ARS		
$\dot{Q}_{cooling}$	21.93	MW_{th}
COP	1.06	—

Figure 6-9 shows the comparison of the detailed simulation results (RTE, COP and Cooling capacity). A comparative analysis was conducted to assess the impact of different types of ARS on the performance of CCHP systems. Multiple cases were examined to discern the distinctive effects resulting from different ARS configurations. The results show that the RTE of CCHP-1, CCHP-2, CCHP-3 and CCHP-4 are 72.93%, 71.52%, 76.50% and 74.76% respectively.

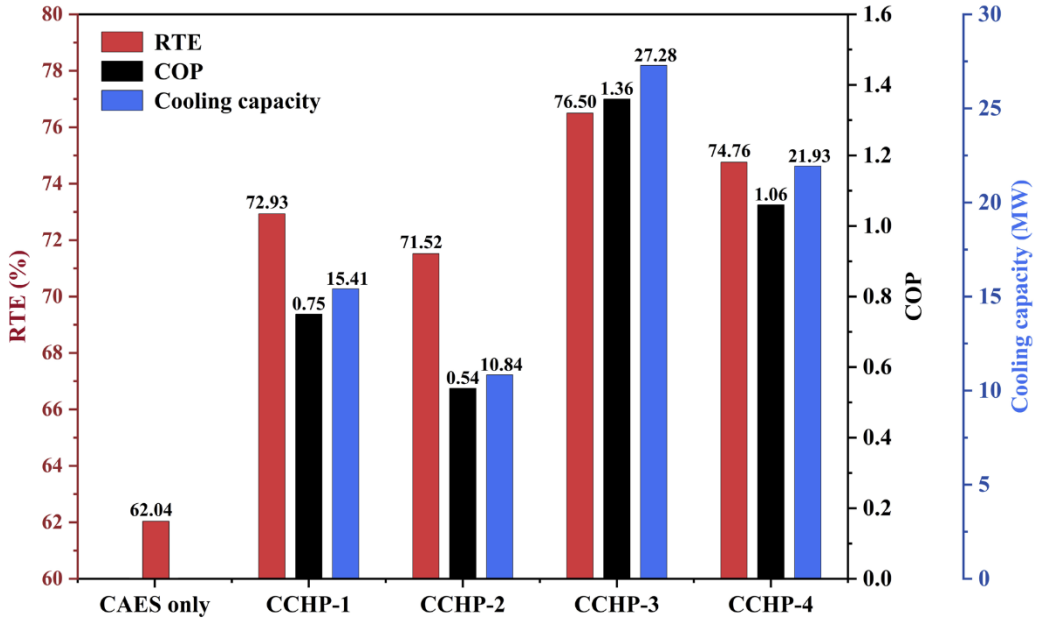

Figure 6-9 comparison between different models on system's performance

Firstly, a comparative analysis of different type of ARS with the same working medium reveals the superiority of double-effect ARS over single-effect ARS (CCHP-3>CCHP-1 and CCHP-4>CCHP-2). The enhanced performance of double-effect ARS can be attributed to the additional refrigerant produced twice, specifically in the DESORBER and DESORBER2 stages. This is achieved by utilizing the heat available from the condensation of vapour refrigerant emanating from the higher temperature desorber (DESORBER2).

Secondly, a comparison of ARS with the same effect but employing different working mediums demonstrates the superiority of LiBr/H_2O over NH_3/H_2O. It could be found that the LiBr/H_2O is better than NH_3/H_2O (CCHP-1>CCHP-2 and CCHP-3>CCHP-4). Notably, the latent heat of the NH_3/H_2O solution is higher than that of LiBr/H_2O systems. Consequently, the efficiency of the desorber stage is diminished in NH_3/H_2O ARS. The properties of LiBr/H_2O lend higher desorber performance than NH_3/H_2O.

Lastly, when aiming to achieve the same cooling capacity, NH_3/H_2O ARS necessitates higher mass flowrates compared to LiBr/H_2O ARS. This disparity can be attributed to the differences in fluid properties and system characteristics between the two working media.

In summary, the double-effect LiBr/H_2O ARS (CCHP-3) has the best performance, it can produce the most cooling capacity (27.28 MW) with COP of 1.36. Therefore, CCHP-3 can be selected when the refrigeration is at high demand.

6.4 Economic analysis

The economic analysis of the proposed CCHP system was conducted through APEA V12. The levelized cost of electricity (LCOE) was determined by dividing the total annual cost (TAC) by the sum of the annual power, heating and cooling output, as represented in equation (6-1), which has been previously utilized in similar studies (Meng et al., 2019; Luo and Wang 2017).

$$LCOE = \frac{TAC}{E_{cchp-output}} \qquad (6-1)$$

The TAC, which is the key metric for assessing the economic feasibility of the proposed system, is the sum of annualized capital expenditure (ACAPAX), fixed operational expenditure (FOPEX) and variable operational expenditure (VOPEX) as defined in eq. (6-2), (6-3), and (6-4) (Meng et al., 2019; Luo and Wang 2017).

$$TAC = ACAPEX + FOPEX + VOPEX \qquad (6-2)$$

$$ACAPEX = CAPEX \times CRF \qquad (6-3)$$

$$VOPEX = Fuel\ cost\ +\ Electricity\ consumption\ cost \qquad (6-4)$$

The ACAPEX is the total capital expenditure (CAPEX) multiplied by the capital recovery factor (CRF), which is calculated by eq. (6-5).

$$CRF = \frac{i(i+1)^n}{(i+1)^n - 1} \qquad (6-5)$$

Where n is the economic life of the plant and i is the interest rate.

The FOPEX includes the costs of long-term service agreements, overheads, operating and maintenance (O&M) expenses and other constant expenditures,

regardless of whether the facility is working at half or full load or is shutdown (Meng et al., 2019; Luo and Wang, 2017). These costs can be expressed mathematically as shown in eq. (6-6).

$$FOPEX = 0.03 \times CAPEX \qquad (6-6)$$

The CAPEX represents the total capital expenditure associated with the charging process, discharging process, ORC and ARS, as defined in eq. (6-7).

$$CAPEX = Cost_{charging} + Cost_{discharging} + Cost_{ORC} + Cost_{ARS} \qquad (6-7)$$

The payback period is adopted here (Ye et al., 2019).

$$PBP = \frac{CAPEX}{Sales\ Revenue - Operating\ Cost} \qquad (6-8)$$

$$Sales\ Revenue = Sale_{Heating} + Sale_{Cooling} + Sale_{Electricity} \qquad (6-9)$$

Table 6-3 presents the investment cost and cost equations of CCHP components in their respective capacities, enabling a precise economic analysis.

Table 6-3 Cost equations of each component (Ahmadi, 2013; Razmi et al., 2019; Akrami et al., 2017; Liu et al 2022)

Components	**The capital investment cost equation**
CAES-charging	
LPC & HPC	$Cost_{LPC} = 44.71 \frac{\dot{m}}{0.95 - \eta_{AC}} \frac{P_{out}}{P_{in}} \ln\left(\frac{P_{out}}{P_{in}}\right)$
IC	$Cost_{IC} = 12{,}000 \left(\frac{A_{IC}}{100}\right)^{0.6}$, $A_{IC} = \frac{Q_{IC}}{U_{IC} \times LMTD_{IC}}$
AC	$Cost_{AC} = 12{,}000 \left(\frac{A_{AC}}{100}\right)^{0.6}$
Cavern	$Cost_{Cavern} = 4{,}042 V_{Cavern}^{0.506}$
CAES-discharging	

COM	$Cost_{CC} = 28.98\dot{m}\left(1 + e^{0.015*(T_{in}-1540)}\right)\frac{1}{0.995 - \frac{P_{out}}{P_{in}}}$
LPT & HPT	$Cost_{tur} = 301.45\dot{m}\frac{1}{0.95 - \eta_{tur}}\ln\left(\frac{P_{in}}{P_{out}}\right)\left(1 + e^{0.025(T_{in}-1{,}570)}\right)$
REC	$Cost_{REC} = 12{,}000\left(\frac{A_{REC}}{100}\right)^{0.6}$
ORC-charging	
OT	$Cost_{OT} = 4{,}750\left(\dot{W}_{orc,tur}\right)^{0.75}$
COND1	$Cost_{OC} = 516.62(A_{OC})^{0.6}$
PUMP1	$Cost_{OP} = 2{,}000\left(\dot{W}_{orc,pump}\right)^{0.65}$
INTC&AFC	$Cost_{OE} = 309.14(A_{OE})^{0.85}$
ARS-discharging	
DESORBER	$Cost_{DES} = 17{,}500\left(\frac{A_{DES}}{100}\right)^{0.6}$
COND2	$Cost_{COND} = 8{,}000\left(\frac{A_{COND}}{100}\right)^{0.6}$
EVAP	$Cost_{EVAP} = 16{,}000\left(\frac{A_{EVAP}}{100}\right)^{0.6}$
ABS	$Cost_{ABS} = 16{,}000\left(\frac{A_{ABS}}{100}\right)^{0.6}$
SHX	$Cost_{SHX} = 12{,}000\left(\frac{A_{SHX}}{100}\right)^{0.6}$
PUMP2	$Cost_{PUMP} = 2{,}000\left(\dot{W}_{LiBr,pump}\right)^{0.65}$
EV1	$Cost_{VAL1} \cong 0$
EV2	$Cost_{VAL2} \cong 0$

An economic feasibility study is crucial to evaluate the potential profitability of the proposed CCHP system. Economic parameters and unit prices used in the study are detailed in Table 6-4 (Meng et al., 2019; McGrail et al., 2013), with all costs presented in US Dollars. The proposed system is assumed to have a

lifespan of 20 years, and a daily operation of 9 hours is considered for the analysis.

Table 6-4 Related economic parameters of proposed system (Arabkoohsar et al., 2017; Zhang et al., 2019)

Parameter	Value
Economic life of plant	20 years
Interest rate	4%
CRF	0.074
Proportion of operation and maintenance	3%
Daily operation hours	9 hours
Natural gas price	0.194 $/m^3
Hot water price	19 $/MWh
Electricity price	13.9 $/MWh
Cooling price	114 $/MWh

Table 6-5 The overall cost of the CCHP system with the breakdown details

Variables	CCHP-1	CCHP-2	CCHP-3	CCHP-4
Capital cost of charging process (M$/year)	62.03	62.03	62.03	62.03
Capital cost of discharging process (M$/year)	42.26	42.26	42.26	42.26
Capital cost of ORC process (M$/year)	9.35	9.35	9.35	9.35
Capital cost of ARS process (M$/year)	0.66	0.85	1.18	1.35
CAPEX (M$/year)	114.31	114.50	114.83	115.00
Annualized ACAPEX (M$/year)	8.46	8.47	8.50	8.51
FOPEX (M$/year)	3.43	3.44	3.45	3.45
Fuel cost (M$/year)	0.63	0.63	0.63	0.63
Cooling revenue (M$/year)	11.54	8.12	20.43	16.43
Sales revenue (M$/year)	31.25	27.83	40.14	36.14
PBP (year)	13.2	15.7	12.9	15.1
LCOE ($/MWh)	31.98	32.46	31.01	32.95

Table 6-5 provides a comprehensive comparison of the costs associated with different CCHP systems integrated with different types of ARS. The CCHP-3 system has the lowest LCOE of 31.01 $/MWh in design condition. Furthermore, the CCHP-3 system has a payback period of 12.9 years and the sales revenue can reach up to 40.14 M$/year. The superior performance of the CCHP-3 system can be attributed to its high cooling capacity. The economic evaluation confirms that the CCHP-3 system is a viable option from a financial perspective.

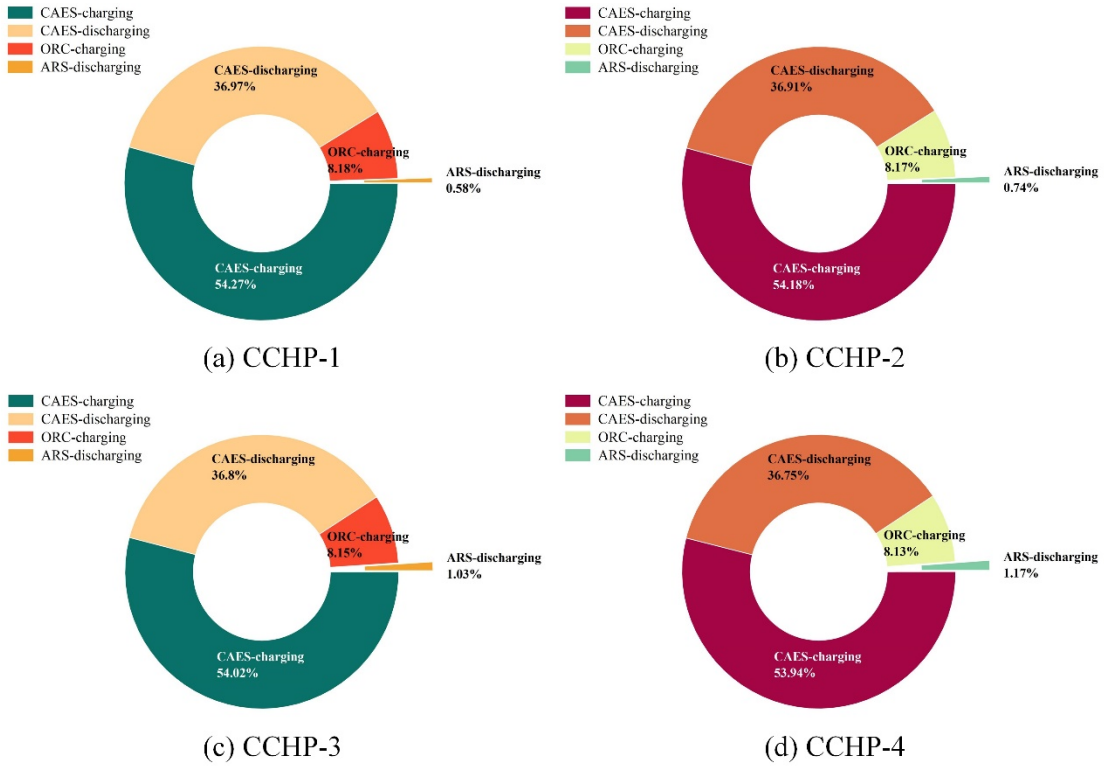

Figure 6-10 Cost distribution of each subsystem (CAES-charging, CAES-discharging, ORC-charging, and ARS-discharging) of the CCHP system

Figure 6-10 shows the cost distribution of each subsystem (CAES-charging, CAES-discharging, ORC-charging and ARS-discharging) of the CCHP system. By comparing the four different systems (CCHP-1, CCHP-2, CCHP-3 and CCHP-4), the results indicate that the cost distribution is basically the same. The cost of CAES-charging accounts for the largest proportion of the CCHP system, indicating that the multi-stage compressor is the most expensive component. Furthermore, it should be noted that the least expensive component is the ARS-discharging.

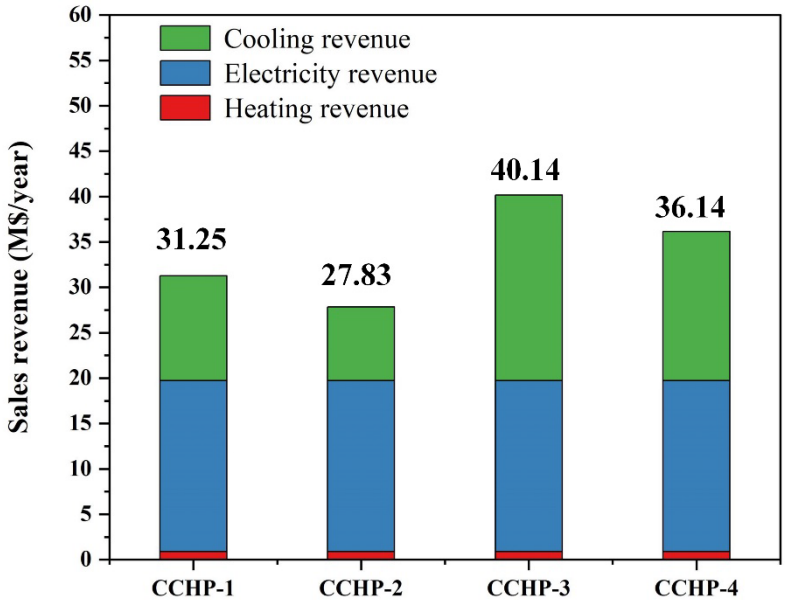

Figure 6-11 Comparative sales revenue for different four different systems

Figure 6-11 in the present study presents a comparison of the sales revenue for four different CCHP systems. The results show that, under the designed conditions, CCHP-3 achieves the highest sales revenue, with a sales revenue of 40.14 M$/year. Interestingly, the proportion of ARS cost in the overall cost of the CCHP system is only around 1%. This indicates that although the ARS component contributes minimally to the overall cost, it can have a significant impact on the sales revenue.

6.5 Conclusion

This chapter studied the CCHP system through a model-based techno-economic assessment. Steady-state models for CAES, ORC and different types of ARS were developed in Aspen Plus®. All the models were validated. The study analysed the impact of different types of ARS systems on CCHP system performance. In the newly proposed CCHP system, a new operating strategy was proposed: the waste heat from the discharging process is only used for the ARS. Under the designed operating conditions, the key findings are as follows:

(1) The superiority of double-effect ARSs over single-effect ARSs with the same working medium.
(2) The LiBr/H_2O is more suitable than NH_3/H_2O as working medium.

(3) The parametric analysis indicates that COP and RTE increased with the ARS mass flowrate. The CCHP-3 system (double-effect ARS using LiBr/H_2O) can produce 206 MW of electrical energy, 7.26 MW of heating and 27.28 MW cooling capacity (COP 1.36).

(4) The LCOE of the CCHP-3 system is 31.01 $/MWh, the payback period of the CCHP-3 system is 12.9 years. These favourable economic indicators render CCHP-3 is preferred from the economic point of view. The ARS cost proportion of the CCHP system is around only 1%, but ARS could bring more sales revenue.

7. Conclusions and Recommendations for Future Work

7.1 Conclusions

This chapter first summarizes the main conclusions of this work. Recommendations are then given for the future work based on this study.

7.1.1 Steady-state simulation and model validations

The steady-state models of CAES, ORC and different types of ARS were developed using Aspen Plus® in Chapter 3. Each subsystem model was performed validation and comparison using the real plant and reference literature data as benchmarks to ascertain accuracy. All relative errors were less than 5% and the results of the simulation matched the commercial plant data.

7.1.2 Thermodynamic analysis of CCHP

In Chapter 4, the newly proposed CCHP system comprised of a CAES, ORC and a single- effect ARS using LiBr/H_2O. A comprehensive thermodynamic analysis of a CCHP system was applied to the system to analyse its performance. The main findings are summarised as follows: (a) The RTE of the proposed CCHP system has been improved 12.35% when compared with the McIntosh CAES plant (54%). Under the design condition, the RTE and overall exergy efficiency of the system are 66.35% and 51.21%, respectively. (b) Total exergy destruction of the CCHP system is equal to 478 MW, in which the combustion chamber is responsible for more than half of it. After the combustion chamber, the cavern, and recuperator have the highest value of exergy destruction. (c) R290 (Propane) as the ORC working fluid is the most suitable working fluid with the best performance. (d) Of all the parameters considered, the inlet temperature of the compressor, the inlet temperature of the combustion chamber and the inlet pressure of the ORC turbine are the most critical parameters, which can significantly improve the RTE and overall exergy efficiency.

7.1.3 Multi-objective optimisation of CCHP

Based on the validated models, a multi-objective optimisation was employed for the CCHP system to obtain optimal operating conditions in Chapter 5. To achieve the maximum utilisation of waste heat, five commonly used ORC

working fluids were analysed through multi-objective optimisation. (a) It was found that R601 was the better ORC working fluid for the proposed CCHP system from the system efficiency perspective at optimal points. (b) The results show that the RTE and ICPP of the optimal suggested CCHP system can reach up to 68.38% (increased by 3.05%) and 0.1984 $/kWh (decreased by 2.68%), respectively. Based on the optimal results, detailed thermodynamic (energy and exergy) and economic analysis were investigated. (c) The exergy analysis results indicate that the discharging process is a significant subsection that accounts for the largest proportion of the exergy destruction (57.90%). (d) The ARS has an economic advantage over ORC, making up 1.2846% and 1.6852% of the total cost. In summary, the suggested CCHP system has higher RTE and lower ICPP than previous work.

7.1.4 Thermodynamic analysis of CCHP with different types of ARS

The study in Chpater 6 analysed the impact of different types of ARS systems on CCHP system performance. A new operating strategy was proposed where waste heat from the discharging process is used only for the ARS. The main findings of the study are: (a) The superiority of double-effect ARS over single-effect ARS with the same working medium. (b) The LiBr/H_2O is more suitable than NH_3/H_2O as working medium. (c) The parametric analysis indicates that COP and RTE increased with the ARS mass flowrate. (d) The CCHP-3 system (double-effect ARS using LiBr/H_2O) can produce 206 MW of electrical energy, 7.26 MW of heating and 27.28 MW cooling capacity (COP 1.36). (e) The LCOE of the CCHP-3 system is 31.01 $/MWh, the payback period of the CCHP-3 system is 12.9 years. These favourable economic indicators render CCHP-3 is preferred from the economic point of view. (f) The ARS cost proportion of the CCHP system is around only 1%, but ARS could bring more sales revenue.

7.2 Recommendations for future research

Although interesting and very promising results have been obtained in this Ph.D. study, there are still numerous aspects that need further investigation. The following areas are recommended for further research in the study of CAES:

- The extant study of CAES primarily revolves around steady-state performance evaluation. The dynamic simulation and modelling are needed in the future study.

- Current discussions have predominantly centred around D-CAES systems. Research should be broadened to include other forms of CAES systems, such as AA-CAES.
- Rigorous experimental assessments of compressors and turbine performance, along with dynamic modelling of these components, should be conducted.
- The heat exchanger is intrinsically linked with factors such as pressure loss, the length and number of channels (or flow area) of the heat exchangers. It is thus essential to optimise heat exchanger design, enabling the selection of the most efficient design parameters.
- Future research endeavours should pivot towards the detailed design of the turbomachinery, with emphasis on span line design, generation of performance maps for off-design conditions, dynamic modelling.

In summary, these potential directions could significantly contribute to our evolving understanding of CAES and CCHP, promoting higher RTE and reliability in their operation and implementation.

References

Alirahmi, S.M., Razmi, A.R. and Arabkoohsar, A., 2021. Comprehensive assessment and multi-objective optimisation of a green concept based on a combination of hydrogen and compressed air energy storage (CAES) systems. *Renewable and Sustainable Energy Reviews,* 142, 110850.

Akrami, E., Chitsaz, A., Nami, H. and Mahmoudi, S.M.S., 2017. Energetic and exergoeconomic assessment of a multi-generation energy system based on indirect use of geothermal energy. *Energy,* 124, pp.625-639.

Aneke, M., Wang, M. (2016). Energy storage technologies and real-life applications – A state of the art review. *Applied Energy. 179,* pp.350–377.

Arshad, M.U., Ghani, M.U., Ullah, A., Güngör, A. and Zaman, M., 2019. Thermodynamic analysis and optimisation of double effect absorption refrigeration system using genetic algorithm. *Energy Conversion and Management, 192,* pp.292-307.

Beaudin, M., Zareipour, H., Schellenberg, A., Rosehart, W. (2014). Energy storage for mitigating the variability of renewable electricity sources. In *Energy Storage for Smart Grids: Planning and Operation for Renewable and Variable Energy Resources (VERs).* pp. 1–33.

Becattini, V., Geissbühler, L., Zanganeh, G., Haselbacher, A. and Steinfeld, A., 2018. Pilot-scale demonstration of advanced adiabatic compressed air energy storage, Part 2: Tests with combined sensible/latent thermal-energy storage. *Journal of Energy Storage*, *17*, pp.140-152.

Behzadi, A., Habibollahzade, A., Ahmadi, P., Gholamian, E. and Houshfar, E., 2019. Multi-objective design optimisation of a solar based system for electricity, cooling, and hydrogen production. *Energy,* 169, pp.696-709.

Boles, M. and Cengel, Y., 2014. An Engineering Approach. *New York: McGraw-Hil l Education*.

Bolaji, B.O. and Huan, Z., 2013. Ozone depletion and global warming: Case for the use of natural refrigerant–a review. *Renewable and Sustainable Energy Reviews,* 18, pp.49-54.

Bollinger, B., 2015. Demonstration of isothermal compressed air energy storage to support renewable energy production. Sustainx, Incorporated, Seabrook, NH (United States).

Boyce, M.P., 2011. *Gas turbine engineering handbook*. Elsevier.

Budt, M., Wolf, D., Span, R. and Yan, J., 2016. A review on compressed air energy storage: Basic principles, past milestones and recent developments. *Applied Energy*, *170*, pp.250-268.

Camargos, T.P., Pottie, D.L., Ferreira, R.A., Maia, T.A. and Porto, M.P., 2018. Experimental study of a PH-CAES system: Proof of concept. *Energy*, *165*, pp.630-638.

Cheayb, M., Gallego, M.M., Tazerout, M. and Poncet, S., 2019. Modelling and experimental validation of a small-scale trigenerative compressed air energy storage system. *Applied energy, 239,* pp.1371-1384.

Chen, H., Cong, T.N., Yang, W., Tan, C., Li, Y. and Ding, Y., 2009. Progress in electrical energy storage system: A critical review. *Progress in natural science*, *19*(3), pp.291-312.

Chen, haisheng., Liu, jinchao., Guo, huan., Xu, yujie., and Tan, chunqing., 2012 Principles of compressed air energy storage technology. *Energy storage science and technology, 02,* pp.146-151

Chen, J., Liu, W., Jiang, D., Zhang, J., Ren, S., Li, L., Li, X. and Shi, X., 2017. Preliminary investigation on the feasibility of a clean CAES system coupled with wind and solar energy in China. *Energy, 127,* pp.462-478.

Deane, J.P., Gallachóir, B.Ó. and McKeogh, E.J., 2010. Techno-economic review of existing and new pumped hydro energy storage plant. *Renewable and Sustainable Energy Reviews,* 14(4), pp.1293-1302.

Desai, N.B. and Bandyopadhyay, S., 2016. Thermo-economic comparisons between solar steam Rankine and organic Rankine cycles. *Applied Thermal Engineering, 105,* pp.862-875.

Ding, Y., Olumayegun, O., Chai, Y., Liu, Y. and Wang, M., 2022. Simulation, energy and exergy analysis of compressed air energy storage integrated with

organic Rankine cycle and single-effect absorption refrigeration for trigeneration application. *Fuel*, *317*, 123291.

Dyment, J., Mantrala, V. (2015). *Jump Start: Getting Started with Aspen Plus® V8.0.* Aspen Technology.

Emrich Jr, W.J., 2023. *Principles of Nuclear Rocket Propulsion*. Elsevier.

Ferreira, H.L., Garde, R., Fulli, G., Kling, W., Lopes, J.P. (2013). Characterisation of electrical energy storage technologies. *Energy.* 53, pp.288–298.

Geissbühler, L., Becattini, V., Zanganeh, G., Zavattoni, S., Barbato, M., Haselbacher, A. and Steinfeld, A., 2018. Pilot-scale demonstration of advanced adiabatic compressed air energy storage, Part 1: Plant description and tests with sensible thermal-energy storage. *Journal of Energy Storage*, *17*, pp.129-139.

Ghaebi, H., Parikhani, T., Rostamzadeh, H. and Farhang, B., 2017. Thermodynamic and thermoeconomic analysis and optimisation of a novel combined cooling and power (CCP) cycle by integrating of ejector refrigeration and Kalina cycles. *Energy,* 139, pp.262-276.

Gidwani, M., Bhagwani, A. and Rohra, N., 2014. Supercapacitors: the near Future of Batteries. *International Journal of Engineering Inventions, 4(5),* pp.22-2.

Gomri, R., 2009. Second law comparison of single-effect and double effect vapour absorption refrigeration systems. *Energy Conversion and Management*, *50*(5), pp.1279-1287.

Guo, C., Xu, Y., Zhang, X., Guo, H., Zhou, X., Liu, C., Qin, W., Li, W., Dou, B. and Chen, H., 2017. Performance analysis of compressed air energy storage systems considering dynamic characteristics of compressed air storage. *Energy, 135,* pp.876-888.

Guo, H., Xu, Y., Chen, H. and Zhou, X., 2016. Thermodynamic characteristics of a novel supercritical compressed air energy storage system. *Energy Conversion and Management*, *115*, pp.167-177.

Hannan, M.A., Hoque, M.M., Mohamed, A. and Ayob, A., 2017. Review of energy storage systems for electric vehicle applications: Issues and challenges. *Renewable and Sustainable Energy Reviews*, *69*, pp.771-789.

He, W. and Wang, J., 2018. Optimal selection of air expansion machine in Compressed Air Energy Storage: A review. *Renewable and Sustainable Energy Reviews*, *87*, pp.77-95.

Herold, K.E., Radermacher, R. and Klein, S.A., 2016. *Absorption chillers and heat pumps.* CRC press.

Houssainy, S., Janbozorgi, M., Ip, P. and Kavehpour, P., 2018. Thermodynamic analysis of a high temperature hybrid compressed air energy storage (HTH-CAES) system. *Renewable Energy, 115,* pp.1043-1054.

IEA (2022). *Global Energy & CO2 Status Report.* [online] Available at: https://www.iea.org/geco/electricity/ [Accessed 2 June 2023].

Jalili, M., Chitsaz, A. and Alhuyi Nazari, M., 2021. Investigating the fuel type influence on the thermo-economic performance of absorption refrigeration systems: a comparative study. *Journal of Thermal Analysis and Calorimetry,* pp.1-18.

Jafarizadeh, H., Soltani, M. and Nathwani, J., 2020. Assessment of the Huntorf compressed air energy storage plant performance under enhanced modifications. *Energy Conversion and Management, 209,* 112662.

Kanoglu, M. and Bolatturk, A., 2008. Performance and parametric investigation of a binary geothermal power plant by exergy. *Renewable Energy, 33(11),* pp.2366-2374.

Kaldellis, J.K., 2008. Integrated electrification solution for autonomous electrical networks on the basis of RES and energy storage configurations. *Energy Conversion and Management,* 49(12), pp.3708-3720.

Kaiser, F., 2015. Steady-state analyse of existing compressed air energy storage plants. *Power and Energy Student Summit (PESS) 2015, January 13th-14th, Dortmund Germany*.

Kalina, A.I., Kalina Alexander Ifaevich, 1982. Generation of energy by means of a working fluid, and regeneration of a working fluid. U.S. Patent 4,346,561.

Kim, Y.M. and Favrat, D., 2010. Energy and exergy analysis of a micro-compressed air energy storage and air cycle heating and cooling system. *Energy*, *35*(1), pp.213-220.

King, M., Jain, A., Bhakar, R., Mathur, J. and Wang, J., 2021. Overview of current compressed air energy storage projects and analysis of the potential underground storage capacity in India and the UK. *Renewable and Sustainable Energy Reviews*, *139*, 110705.

Kousksou, T., Bruel, P., Jamil, A., El Rhafiki, T. and Zeraouli, Y., 2014. Energy storage: Applications and challenges. *Solar Energy Materials and Solar Cells*, *120*, pp.59-80.

Lee, I. and You, F., 2019. Systems design and analysis of liquid air energy storage from liquefied natural gas cold energy. *Applied Energy,* 242, pp.168-180.

Letcher, T.M. ed., 2020. *Future energy: improved, sustainable and clean options for our planet.* Elsevier.

Leung, P., Li, X., De León, C.P., Berlouis, L., Low, C.J. and Walsh, F.C., 2012. Progress in redox flow batteries, remaining challenges and their applications in energy storage. *RSC Advances, 2(27),* pp.10125-10156.

Li, H. and Zhou, H., 2012. Enhancing the performances of Li-ion batteries by carbon-coating: present and future. *Chemical Communications, 48(9),* pp.1201-1217.

Li, Y., Wang, X., Li, D. and Ding, Y., 2012. A trigeneration system based on compressed air and thermal energy storage. *Applied Energy*, *99*, pp.316-323.

Liu, B.T., Chien, K.H. and Wang, C.C., 2004. Effect of working fluids on organic Rankine cycle for waste heat recovery. *Energy*, *29*(8), pp.1207-1217.

Liu, W., Liu, L., Zhou, L., Huang, J., Zhang, Y., Xu, G. and Yang, Y., 2014. Analysis and optimisation of a compressed air energy storage—combined cycle system. *Entropy, 16(6),* pp.3103-3120.

Luo, X., Wang, J., Dooner, M., Clarke, J. (2015). Overview of current development in electrical energy storage technologies and the application potential in power system operation. *Applied Energy.* 137, pp.511–536.

Lüdtke, K.H., 2004. Process centrifugal compressors: basics, function, operation, design, application. Springer Science & Business Media.

Macchi, E. and Astolfi, M. eds., 2016. *Organic rankine cycle (ORC) power systems: technologies and applications*. Woodhead Publishing.

Maryami, R. and Dehghan, A.A., 2017. An exergy based comparative study between LiBr/water absorption refrigeration systems from half effect to triple effect. *Applied Thermal Engineering,* 124, pp.103-123.

Mason, J., Fthenakis, V., Zweibel, K., Hansen, T. and Nikolakakis, T., 2008. Coupling PV and CAES power plants to transform intermittent PV electricity into a dispatchable electricity source. *Progress in Photovoltaics: Research and Applications, 16(8),* pp.649-668.

McNevin, C. and Harrison, S.J., 2017. Multi-stage liquid-desiccant air-conditioner: Experimental performance and model development. *Building and Environment*, *114*, pp.45-55.

McGrail, B.P.J.E., Cabe, J., Davidson, C., Knudsen, F., Bacon, D., Bearden, M., Charmness, M., Horner, J.A., Reidel, S.P., Schaef, H.T. and Spane, F.A., 2013. Technoeconomic performance evaluation of compressed air energy storage in the Pacific Northwest. *Pacific Northwest National Laboratory, Richland, USA*.

Mei, S., Wang, J., Tian, F., Chen, L., Xue, X., Lu, Q., Zhou, Y. and Zhou, X., 2015. Design and engineering implementation of non-supplementary fired compressed air energy storage system: TICC-500. *Science China Technological Sciences*, *58*, pp.600-611.

Meng, H., Wang, M., Aneke, M., Luo, X., Olumayegun, O. and Liu, X., 2018. Technical performance analysis and economic evaluation of a compressed air energy storage system integrated with an organic Rankine cycle. *Fuel*, *211*, pp.318-330.

Meng, H., 2019. *Design and Operation of Compressed Air Energy Storage (CAES) for Wind Power through Process Modelling and Simulation,* PhD thesis, University of Sheffield.

Meng, H., Wang, M., Olumayegun, O., Luo, X. and Liu, X. (2019). Process design, operation and economic evaluation of compressed air energy storage (CAES) for wind power through modelling and simulation. *Renewable Energy, 136,* pp.923-936.

Misra, R.D., Sahoo, P.K., Sahoo, S. and Gupta, A., 2003. Thermoeconomic optimisation of a single-effect water/LiBr vapour absorption refrigeration system. *International Journal of refrigeration*, *26*(2), pp.158-169.

Mohammadi, A., Ahmadi, M.H., Bidi, M., Joda, F., Valero, A. and Uson, S., 2017. Exergy analysis of a Combined Cooling, Heating and Power system integrated with wind turbine and compressed air energy storage system. *Energy Conversion and Management*, *131*, pp.69-78.

Mohammadi, A., Kasaeian, A., Pourfayaz, F. and Ahmadi, M.H., 2017. Thermodynamic analysis of a combined gas turbine, ORC and absorption refrigeration for a CCHP system. *Applied Thermal Engineering*, *111*, pp.397-406.

Molina, M.G., 2010. Dynamic modelling and control design of advanced energy storage for power system applications. *In Dynamic Modelling. IntechOpen.*

Mokarram, N.H. and Mosaffa, A.H., 2018. A comparative study and optimisation of enhanced integrated geothermal flash and Kalina cycles: A thermoeconomic assessment. *Energy*, *162*, pp.111-125.

Moubayed, N., Kouta, J., El-Ali, A., Dernayka, H. and Outbib, R., 2008, May. Parameter identification of the lead-acid battery model. *In 2008 33rd IEEE Photovoltaic Specialists Conference* (pp. 1-6). IEEE.

Nikolaidis, P. and Poullikkas, A., 2017. A comparative review of electrical energy storage systems for better sustainability. *Journal of power technologies*.

Oshima, T., Kajita, M. and Okuno, A., 2004. Development of sodium‐sulfur batteries. *International Journal of Applied Ceramic Technology*, *1*(3), pp.269-276.

Pelagotti, A., Baldassarre, L., Meher-Homji, C. and Masani, K., 2016. Future trends in LNG Turbomachinery. *In LNG18 Conference*.

Pittock, J., 2010. *Better management of hydropower in an era of climate change*. Water Alternatives 3 (2) (2010) 444.

Pottie, D.L., Ferreira, R.A., Maia, T.A. and Porto, M.P., 2019. An alternative sequence of operation for Pumped-Hydro Compressed Air Energy Storage (PH-CAES) systems. *Energy,* 116472.

Quoilin, S., Van Den Broek, M., Declaye, S., Dewallef, P. and Lemort, V., 2013. Techno-economic survey of Organic Rankine Cycle (ORC) systems. *Renewable and Sustainable Energy Reviews, 22, pp.*168-186.

P. Radgen, “30 Years Compressed Air Energy Storage - Experiences and Outlook,” in IRES 2008 - *International Renewable Energy Storage Conference,* 2008,18.

Razmi, A.R. and Janbaz, M., 2020. Exergoeconomic assessment with reliability consideration of a green cogeneration system based on compressed air energy storage (CAES). *Energy Conversion and Management,* 204, 112320.

Razmi, A., Soltani, M. and Torabi, M., 2019. Investigation of an efficient and environmentally-friendly CCHP system based on CAES, ORC and compression-absorption refrigeration cycle: Energy and exergy analysis. *Energy Conversion and Management, 195,* pp.1199-1211.

Razmi, A.R., Soltani, M., Ardehali, A., Gharali, K., Dusseault, M.B. and Nathwani, J., 2021. Design, thermodynamic, and wind assessments of a compressed air energy storage (CAES) integrated with two adjacent wind farms: A case study at Abhar and Kahak sites, Iran. *Energy,* 221, 119902.

Rismanchi, B., Saidur, R., BoroumandJazi, G. and Ahmed, S., 2012. Energy, exergy and environmental analysis of cold thermal energy storage (CTES) systems. *Renewable and Sustainable Energy Reviews, 16(8),* pp.5741-5746.

Rogeau, A., Girard, R. and Kariniotakis, G., 2017. A generic GIS-based method for small Pumped Hydro Energy Storage (PHES) potential evaluation at large scale. *Applied Energy, 197,* pp.241-253.

Roushenas, R., Razmi, A.R., Soltani, M., Torabi, M., Dusseault, M.B. and Nathwani, J., 2020. Thermo-environmental analysis of a novel cogeneration system based on solid oxide fuel cell (SOFC) and compressed air energy storage (CAES) coupled with turbocharger. Applied Thermal Engineering, 181, 115978.

Roy, P. and Srivastava, S.K., 2015. Nanostructured anode materials for lithium ion batteries. *Journal of Materials Chemistry A, 3(6),* pp.2454-2484.

Saravanamuttoo, H. I., Rogers, G. F. C., & Cohen, H. (2001). *Gas turbine theory.* Pearson Education.

Sadreddini, A., Fani, M., Aghdam, M.A. and Mohammadi, A., 2018. Exergy analysis and optimisation of a CCHP system composed of compressed air energy storage system and ORC. *Energy conversion and management, 157,* pp.111-122.

Sciacovelli, A., Vecchi, A. and Ding, Y., 2017. Liquid air energy storage (LAES) with packed bed cold thermal storage–From component to system level performance through dynamic modelling. *Applied Energy, 190,* pp.84-98.

Sedighnejad, H. (2011). Performance evaluation of a hybrid wind-diesel-compressed air energy storage system. In *Electrical and Computer Engineering (CCECE), 2011 24th Canadian Conference. IEEE,* pp. 270–273.

Soltani, M., Nabat, M.H., Razmi, A.R., Dusseault, M.B. and Nathwani, J., 2020. A comparative study between ORC and Kalina based waste heat recovery cycles applied to a green compressed air energy storage (CAES) system. *Energy Conversion and Management, 222,* 113203.

Somers, C., Mortazavi, A., Hwang, Y., Radermacher, R., Rodgers, P. and Al-Hashimi, S., 2011. Modeling water/lithium bromide absorption chillers in ASPEN Plus. *Applied Energy*, *88*(11), pp.4197-4205.

Tan, X., Li, Q. and Wang, H., 2013. Advances and trends of energy storage technology in microgrid. International Journal of Electrical Power & Energy Systems, 44(1), pp.179-191.

Venkataramani, G., Parankusam, P., Ramalingam, V. and Wang, J., 2016. A review on compressed air energy storage–A pathway for smart grid and polygene ration. *Renewable and Sustainable Energy Reviews*, *62*, pp.895-907.

Wang, R.Z. and Oliveira, R.G., 2006. Adsorption refrigeration—an efficient way to make good use of waste heat and solar energy. *Progress in energy and combustion science*, *32*(4), pp.424-458.

Wang, J., Yan, Z., Wang, M., Ma, S. and Dai, Y., 2013. Thermodynamic analysis and optimisation of an (organic Rankine cycle) ORC using low grade heat source. *Energy*, *49*, pp.356-365.

Wang, J., Lu, K., Ma, L., Wang, J., Dooner, M., Miao, S., Li, J. and Wang, D., 2017. Overview of compressed air energy storage and technology development. *Energies*, *10*(7), 991.

Wang, J., Ma, L., Lu, K., Miao, S., Wang, D. and Wang, J., 2017. Current research and development trend of compressed air energy storage. *Systems Science & Control Engineering, 5(1),* pp.434-448.

Wang, S., Zhang, X., Yang, L., Zhou, Y. and Wang, J., 2016. Experimental study of compressed air energy storage system with thermal energy storage. *Energy*, *103*, pp.182-191.

Wang, X., Yang, C., Huang, M. and Ma, X., 2018. Multi-objective optimisation of a gas turbine-based CCHP combined with solar and compressed air energy storage system. *Energy Conversion and Management*, *164*, pp.93-101.

Wu, D. and Wang, R., 2006. Combined cooling, heating and power: A review. *Progress in Energy and Combustion Science*, *32*(5-6), pp.459-495.

Yang, X., Yang, S., Wang, H., Yu, Z., Liu, Z. and Zhang, W., 2022. Parametric assessment, multi-objective optimisation and advanced exergy analysis of a combined thermal-compressed air energy storage with an ejector-assisted Kalina cycle. *Energy,* 239, 122148.

Yao, E., Wang, H., Wang, L., Xi, G. and Maréchal, F., 2017. Multi-objective optimisation and exergoeconomic analysis of a combined cooling, heating and power based compressed air energy storage system. *Energy Conversion and Management*, *138*, pp.199-209.

Zhao, P., Dai, Y. and Wang, J., 2014. Design and thermodynamic analysis of a hybrid energy storage system based on A-CAES (adiabatic compressed air energy storage) and FESS (flywheel energy storage system) for wind power application. *Energy, 70,* pp.674-684.

Zhao, P., Wang, J. and Dai, Y., 2015. Thermodynamic analysis of an integrated energy system based on compressed air energy storage (CAES) system and Kalina cycle. *Energy Conversion and Management, 98,* pp.161-172.

Zhang, Y., Yang, K., Li, X. and Xu, J., 2013. The thermodynamic effect of thermal energy storage on compressed air energy storage system. *Renewable Energy*, *50*, pp.227-235.

Zhang, J., Cao, S., Yu, L. and Zhou, Y., 2018. Comparison of combined cooling, heating and power (CCHP) systems with different cooling modes based on energetic, environmental and economic criteria. *Energy Conversion and Management, 160,* pp.60-73.

Zhang, X., Zeng, R., Deng, Q., Gu, X., Liu, H., He, Y., Mu, K., Liu, X., Tian, H. and Li, H., 2019. Energy, exergy and economic analysis of biomass and geothermal energy based CCHP system integrated with compressed air energy storage (CAES). *Energy conversion and management,* 199, 111953.

Zhou, Q., Du, D., Lu, C., He, Q. and Liu, W., 2019. A review of thermal energy storage in compressed air energy storage system. *Energy, 188,* 115993.